

**Functionalized Vanadium Oxide as the Cathode  
Material for Rechargeable Aqueous Zinc-ion Batteries**

by

Mei Han

A thesis

presented to the University of Waterloo

in fulfillment of the

thesis requirement for the degree of

Master of Applied Science

in

Chemical Engineering

Waterloo, Ontario, Canada, 2019

© Mei Han 2019

## **Author's Declaration**

I hereby declare that I am the sole author of this thesis. This is a true copy of the thesis, including any required final revisions, as accepted by my examiners.

I understand that my thesis may be made electronically available to the public.

## Abstract

Battery offers a viable solution for storing intermittent energy supplies associated with renewable energy production. Although lithium-ion batteries take up the most battery market, they are still limited by lithium metal resources, high cost and safety concerns. With this regard, aqueous batteries with mildly acidic electrolytes hold a promise for large-scale energy storage. In particular, zinc, as an attractive alternative to lithium metal, has been employed in aqueous rechargeable batteries due to its low-cost, high safety and environmental friendliness. Layered vanadium oxide ( $V_2O_5$ ) as cathode material has gained enhanced interests in the studies of rechargeable aqueous zinc-ion batteries (RAZBs) due to its relatively high capacity. However, commercial  $V_2O_5$  shows poor stability during cycling since the zinc ion intercalation causes degradation of the cathode and battery components. Therefore, in this project, two strategies involve surface coating and metal-ion doping are utilized to improve the electrochemical performance of vanadium-based electrodes in RAZBs.

First, we introduce a coating method to fabricate polymer-modified cathode materials for aqueous zinc-ion batteries, which display improved electrochemical performances under both ambient and elevated temperature conditions. A polypyrrole-coated cathode is demonstrated, and the assembled battery delivers a high capacity of 195.7 mAh·g<sup>-1</sup> at the current rate of 5 C (200 mAh·g<sup>-1</sup> corresponds 1 C), with only 9.5% capacity decay at room temperature after 200 cycles. At an elevated temperature (60°C), the polymer-coated battery still shows outstanding capacity retention, of 80% vs. 25%

for bare  $V_2O_5$  cathode after 150 cycles. Therefore, coating conductive polymers on the surface of cathode materials stabilizes the structure of the positive electrode at high temperatures and offer a viable approach to realize the thermal stability of such batteries.

Second, two kinds of metal ions ( $Zn^{2+}$  and  $Na^+$ ) are doped simultaneously into the  $V_2O_5$  interlayer by a molar ratio of  $Zn:Na = 0.3:0.43$  to form a metal-ion doped cathode material  $Zn_{0.3}Na_{0.43}V_2O_5$  (ZNVO). To enlarge the specific surface area, the commercial  $V_2O_5$  is optimized into nanobelts by a hydrothermal method. The doped positive electrode in 2M  $ZnSO_4$  electrolytic solution reaches over  $300 \text{ mAh}\cdot\text{g}^{-1}$  initial discharge capacity at 5 C, which is much higher than that of undoped electrode material ( $V_2O_5$  nanobelts). Besides, in order to prevent the extraction of Na ions from the positive electrode, additional 2M sodium salt is added to the 2M  $ZnSO_4$  aqueous solution to prepare a dual-ion electrolyte. This dual-ion system (containing dual ion-doped positive electrode and dual ion electrolyte) offers a long-term cycle life,  $\sim 89\%$  capacity retention after 4000 cycles, and a relatively high discharge capacity of  $190 \text{ mAh}\cdot\text{g}^{-1}$  at 5 C during fast charge / discharge process. More importantly, this dual-ion electrolyte effectively suppresses zinc dendrite formation on the anode surface because of the electrostatic shield mechanism, where creating a positively charged shield around the sharp zinc protuberances. Thus, this dual-ion system provides the excellent electrochemical performance of  $Zn // ZNVO$  batteries and holds a promise for realizing practical applications of zinc-ion batteries.

## **Acknowledgements**

The work herein was financially supported by Mitacs through the Mitacs Accelerate program and the University of Waterloo.

I would like to acknowledge my supervisor, Prof. Pu Chen, for the wonderful opportunity to pursue my graduate studies and for his continuous guidance and support during this period.

I would also like to thank lab colleagues Dr. Jian Zhi, Dr. Yu Liu, Shengkai Li, Qianshu Ma for their assistance and support. Their friendship has made my graduate studies more fulfilling.

I would also like to acknowledge my reading committee members Prof. Yuning Li and Prof. Marios Ioannidis for their time and constructive feedback towards the completion of this thesis.

Finally, I would like to thank my parents for their unwavering love and support throughout the master program.

# Table of Contents

<b>Author’s Declaration .....</b>	<b>ii</b>
<b>Abstract.....</b>	<b>iii</b>
<b>Acknowledgements .....</b>	<b>v</b>
<b>List of Figures .....</b>	<b>x</b>
<b>List of Tables .....</b>	<b>xvi</b>
<b>List of Abbreviations .....</b>	<b>xvii</b>
<b>Chapter 1. Aqueous Zinc-ion Battery Systems: Introduction, Limitations, and Research Motivations.....</b>	<b>1</b>
1.1 Introduction .....	1
1.2 Rechargeable Aqueous Zinc Ion Batteries (RAZBs).....	3
1.3 Cathode Materials for Zinc-ion Battery System.....	6
1.3.1 Layered Vanadium Oxide ( $V_2O_5$ ) as the Cathode Material.....	7
1.3.2 Limitations of $V_2O_5$ Cathode in Aqueous Batteries.....	12
1.3.3 Strategies to Overcome $V_2O_5$ Cathode Limitations in Aqueous Batteries .....	13
1.4 Polymeric Species .....	23
1.5 Electrolyte Optimizations to Suppress Dendrite Formation for RAZBs	25

1.6 Project Scope and Objectives .....	27
<b>Chapter 2: Material and Electrochemical Characterization Techniques ....</b>	<b>29</b>
2.1 Material Characterization Techniques .....	29
2.1.1 X-Ray Diffraction (XRD).....	29
2.1.2 Fourier Transform Infra-red Spectroscopy (FTIR).....	32
2.1.3 Scanning Electron Microscopy (SEM).....	34
2.1.4 High-Resolution Transmission Electron Microscopy (HRTEM) .....	37
2.1.5 X-Ray Photoelectron Spectroscopy (XPS).....	39
2.1.6 Thermogravimetric Analysis (TGA).....	42
2.1.7 Inductively Coupled Plasma Mass Spectrometry (ICP-MS).....	43
2.2 Electrochemical Characterization Techniques .....	45
2.2.1 Electrochemical Impedance Spectroscopy (EIS).....	45
2.2.2 Cyclic Voltammetry .....	49
2.2.3 Battery Testing .....	51
<b>Chapter 3: Conductive Polymer Modified-Vanadium Oxide as the Cathode</b>	
<b>Materials in Rechargeable Aqueous Zinc-ion Batteries.....</b>	<b>52</b>
3.1 Fabrication of Conductive Polymer Coated Ball-milled Vanadium Oxide	52
3.1.1 Synthesizing Polypyrrole (PPy) on the Surface of Ball-milled Vanadium	
Oxide.....	53

3.1.2 Synthesizing Polyaniline (PANI) on the Surface of Ball-milled Vanadium Oxide.....	54
3.2 Cathode Fabrication and Battery Assembling .....	55
3.3 Material Characterizations .....	56
3.3.1 Fourier Transformed Infra-Red Spectroscopy (FTIR).....	56
3.3.2 X-Ray Diffraction (XRD).....	57
3.3.3 Electron Microscopy .....	59
3.3.5 X-ray Photoelectron Spectroscopy (XPS) .....	61
3.3.4 Thermogravimetric Analysis (TGA).....	63
3.4 Electrochemical Performance.....	64
3.4.1 Cyclic Voltammetry (CV) .....	65
3.4.2 Rate Capability.....	69
3.4.3 Cyclic Performance .....	71
3.4.4 Electrochemical Impedance Spectroscopy (EIS).....	74
3.5 Section Conclusions.....	78
<b>Chapter 4. Dual-ion Doped Vanadium Oxide as the Cathode Material in Rechargeable Aqueous Zinc-ion Batteries .....</b>	<b>80</b>
4.1 Synthesis of Dual-ion Inserted Vanadate Material .....	80
4.2 Cathode Fabrication and Battery Assembling .....	82

4.3 Material Characterizations .....	82
4.3.1 Scanning Electron Microscopy (SEM).....	82
4.3.2 Inductively Coupled Plasma Mass Spectrometry (ICP-MS).....	84
4.3.3 X-ray Photoelectron Spectroscopy (XPS) .....	84
4.4 Basic Electrochemical Performance .....	86
4.4.1 Cyclic Performance .....	86
4.4.2 Rate Capability.....	88
4.4.3 Cyclic Voltammetry (CV) .....	89
4.5 Anode Characterizations .....	91
4.6 Advanced Characterizations .....	92
4.6.1 Cyclic Voltammetry (CV) .....	92
4.6.2 X-Ray Diffraction (XRD).....	95
4.6.3 Fourier Transformed Infra-Red Spectroscopy (FTIR).....	96
4.7 Section Conclusions.....	97
<b>Chapter 5. Summary of Thesis and Recommendations for Future Work ...</b>	<b>99</b>
<b>References .....</b>	<b>102</b>
<b>Appendices .....</b>	<b>113</b>

## List of Figures

Figure 1. A) Worldwide primary energy consumption, by fuel, 1970-2040; B) share of primary energy consumption, by fuel, 1970-2040 [1].....	2
Figure 2. Global demand for lithium-ion batteries, 2005-2040 [2].....	3
Figure 3. Aqueous zinc-ion battery system [24]. ....	5
Figure 4. The operating potential and specific capacity for various cathode materials in aqueous ZIBs [24].....	8
Figure 5. The corresponding vanadium coordination polyhedral to vanadium valence [39]. ....	9
Figure 6. The orthorhombic structure of $V_2O_5$ in A) ac plane and B) ab plane [49]. .....	10
Figure 7. Schematic of the crystal structure of $V_2O_5 \cdot H_2O$ xerogels [53].....	11
Figure 8. Schematic of the $V_2O_5$ cathode with 2 M $ZnSO_4$ aqueous electrolyte in RAZB system [57]. ....	12
Figure 9. Typical SEM (A-C) and TEM (D and E) images of single-crystalline $V_2O_5$ nanobelts. The inserted patterns in A and D are the cross-section of $V_2O_5$ nanobelts and SAED pattern, respectively. The scale bar corresponds to 100 nm [66]. ....	14
Figure 10. Schematic of producing nanostructured $V_2O_5$ material by electrospinning method and subsequent annealing [67]. ....	15

Figure 11. Schematic of two-dimensional leaf-like $V_2O_5$ nanosheet production process [68].	16
Figure 12. Schematic of the preparation of carbon-coated $V_2O_5$ composite [77].	18
Figure 13. Schematic of hybrid MWCNTs / $V_2O_5$ composite formation via hydrothermal method [78].	19
Figure 14. A) SEM and B) TEM images of $V_2O_5$ / PANI nanobelts [82].	20
Figure 15. Schematic of Zn // $Zn_{0.25}V_2O_5$ battery in 1M $ZnSO_4$ electrolyte [94].	22
Figure 16. Schematic of Zn ion de- / intercalation in the $Na_{0.33}V_2O_5$ electrode [95].	23
Figure 17. The structures of A) PPy and B) PANI [104].	24
Figure 18. Illustration of zinc deposition process based on electrostatic shield mechanism.	27
Figure 19. Schematic of XRD instrument.	31
Figure 20. Schematic showing the interaction between X-rays and a typical crystalline sample [114].	31
Figure 21. Working principle of an FTIR interferometer [118].	34
Figure 22. Components and principle of operation of an SEM [123].	35
Figure 23. Schematic of electron beam interaction [127].	36
Figure 24. Components and principle of operation of an TEM [132].	39

Figure 25. Schematic of XPS instrument [134]. .....	40
Figure 26. Principle of the photoelectron emission [135].....	41
Figure 27. Schematic of TGA instrument [137].....	43
Figure 28. Schematic of ICP-MS instrument [138].....	44
Figure 29. Experimental EIS system set up using three electrode mode [139]. .	47
Figure 30. Relationship between Nyquist plot components [141]. .....	48
Figure 31. A) Potential scan with time and B) the resulted CV plot [143].....	50
Figure 32. Experimental procedure of synthesizing ball-milled V <sub>2</sub> O <sub>5</sub> -PPy. ....	54
Figure 33. The FTIR patterns of A) ball-milled V <sub>2</sub> O <sub>5</sub> -PPy powder and B) ball- milled V <sub>2</sub> O <sub>5</sub> -PANI powder. ....	57
Figure 34. The XRD patterns of ball-milled V <sub>2</sub> O <sub>5</sub> and commercial V <sub>2</sub> O <sub>5</sub> (PDF# 41-1426). .....	58
Figure 35. The XRD patterns of ball-milled V <sub>2</sub> O <sub>5</sub> -PPy and ball-milled V <sub>2</sub> O <sub>5</sub> -PANI and ball-milled V <sub>2</sub> O <sub>5</sub> .....	59
Figure 36. SEM images of A) ball-milled V <sub>2</sub> O <sub>5</sub> , B) ball-milled V <sub>2</sub> O <sub>5</sub> -PPy and C) ball-milled V <sub>2</sub> O <sub>5</sub> -PANI with scale bar of 1 μm. TEM images of D) ball-milled V <sub>2</sub> O <sub>5</sub> , the coating thickness of E) ball-milled V <sub>2</sub> O <sub>5</sub> -PPy and F) ball-milled V <sub>2</sub> O <sub>5</sub> -PANI with scale bar of 10 nm. ....	61
Figure 37. EDX image of ball-milled V <sub>2</sub> O <sub>5</sub> -PPy sample.....	61
Figure 38. XPS spectra of ball-milled V <sub>2</sub> O <sub>5</sub> -PPy A) C 1s, B) N 1s, and ball-milled V <sub>2</sub> O <sub>5</sub> -PANI C) C 1s, D) N 1s. ....	63

Figure 39. TGA measurements of ball-milled  $V_2O_5$ , ball-milled  $V_2O_5$ -PPy and ball-milled  $V_2O_5$ -PANI in a temperature range of 30°C to 650°C at a ramp rate of 10°C·min<sup>-1</sup>. ..... 64

Figure 40. The CV plots of A) ball-milled  $V_2O_5$ , ball-milled  $V_2O_5$ -PPy and ball-milled  $V_2O_5$ -PANI at their 1st cycling, B) ball-milled  $V_2O_5$  cathode and C) ball-milled  $V_2O_5$ -PANI at their 1st and 50th cycling, D) ball-milled  $V_2O_5$ -PPy and the conductive polymer PPy cathode at 1st cycling with a scan rate of 0.1 mV·s<sup>-1</sup>. The galvanostatic charge / discharge curves of E) ball-milled  $V_2O_5$  cathode and F) ball-milled  $V_2O_5$ -PANI cathode at 5 C at room temperature. .... 67

Figure 41. CV plots of A) ball-milled  $V_2O_5$ , B) ball-milled  $V_2O_5$ -PPy and C) ball-milled  $V_2O_5$ -PANI at their selected cycling (1st, 50th, 100th) with 1 mV·s<sup>-1</sup> scanning rate at 60°C. .... 69

Figure 42. Rate performance of ball-milled  $V_2O_5$ , ball-milled  $V_2O_5$ -PPy and ball-milled  $V_2O_5$ -PANI samples at A) room temperature in coin cells (~ 1 cm<sup>2</sup> in cell) and B) at 60°C in large batteries (~ 9 cm<sup>2</sup> in cell) at different current densities. Rate capability of large batteries (~ 9 cm<sup>2</sup> in cell) containing C) ball-milled  $V_2O_5$ -PPy and D) ball-milled  $V_2O_5$ -PANI cathodes at 40°C, 60°C and 80°C at different current densities (1 C, 2.5 C, 5 C and 10 C). 1 C corresponds to 200 mA·g<sup>-1</sup>. All of them have mass loading around 4.5 mg·cm<sup>-2</sup>. .... 70

Figure 43. Galvanostatic cycling tests of ball-milled  $V_2O_5$ , ball-milled  $V_2O_5$ -PPy and ball-milled  $V_2O_5$ -PANI samples A) at room temperature in coin cells ( $\sim 1 \text{ cm}^2$  in cell), B) at  $40^\circ\text{C}$ , C)  $60^\circ\text{C}$  and D)  $80^\circ\text{C}$  in large batteries ( $\sim 9 \text{ cm}^2$  in cell) at a current density of 5 C over the voltage range of 0.2-1.6 V. All of them have mass loading around  $4.5 \text{ mg}\cdot\text{cm}^{-2}$ ..... 72

Figure 44. Galvanostatic cycling tests of A) ball-milled  $V_2O_5$ -PPy and B) ball-milled  $V_2O_5$ -PANI samples at  $60^\circ\text{C}$  in large batteries ( $\sim 9 \text{ cm}^2$  in cell) at a current density of 5 C over the voltage range of 0.2-1.6 V. All of them have mass loading around  $4.5 \text{ mg}\cdot\text{cm}^{-2}$ ..... 74

Figure 45. Nyquist plots of three samples at their 50th cycle under A) room temperature, and B)  $60^\circ\text{C}$ ..... 77

Figure 46. Experimental procedure of synthesizing dual-ion inserted vanadate material..... 81

Figure 47. SEM images of A) commercial  $V_2O_5$  and B) synthesized ZNVO nanobelts with scale bar of  $1 \mu\text{m}$ . C) EDX image of ZNVO sample..... 83

Figure 48. XPS spectra of pristine ZNVO sample in A) survey spectrum, B) V 2p spectrum, C) Na 1s spectrum and D) Zn 2p spectrum. .... 85

Figure 49. Cycling performance of A)  $V_2O_5$  and ZNVO nanobelts electrodes in 2M  $ZnSO_4$  electrolyte and B) ZNVO electrode in 2M  $ZnSO_4$  electrolyte with and without  $Na_2SO_4$  addition. C) The galvanostatic discharge curves of ZNVO cathode in dual-ion electrolyte. All tests are conducted in coin cells at

a current density of 5 C in a voltage range of 0.2-1.6 V. All of them have mass loading around $2.3 \text{ mg} \cdot \text{cm}^{-2}$ .....	87
Figure 50. Rate performance of ZNVO electrode in different electrolytes at various current densities, where 1C corresponds to $200 \text{ mA} \cdot \text{g}^{-1}$ .....	88
Figure 51. Cyclic voltammograms of ZNVO electrode in A) 2M ZnSO <sub>4</sub> and B) 2M ZnSO <sub>4</sub> + 2M Na <sub>2</sub> SO <sub>4</sub> electrolyte at a scan rate of $0.1 \text{ mV} \cdot \text{s}^{-1}$ . Cyclic voltammograms of ZNVO electrode in C) 2M ZnSO <sub>4</sub> and D) 2M ZnSO <sub>4</sub> + 2M Na <sub>2</sub> SO <sub>4</sub> electrolyte at a scan rate of $0.5 \text{ mV} \cdot \text{s}^{-1}$ at selected cycle numbers. ....	90
Figure 52. SEM images of anode surface in different electrolytes at their selected cycles at fully charged state. Scale bars, $2 \text{ } \mu\text{m}$ . ....	92
Figure 53. CV plots of A) ZNVO electrode in different electrolytes and B) NVO and ZNVO in 2M Na <sub>2</sub> SO <sub>4</sub> electrolyte at their 2nd cycling at a scan rate of $0.1 \text{ mV} \cdot \text{s}^{-1}$ .....	94
Figure 54. Ex situ XRD patterns of ZNVO electrode in 2M ZnSO <sub>4</sub> + 2M Na <sub>2</sub> SO <sub>4</sub> electrolyte at determined voltages at their 2nd cycle.....	96
Figure 55. FTIR spectra of ZNVO electrode in 2M ZnSO <sub>4</sub> + 2M Na <sub>2</sub> SO <sub>4</sub> electrolyte at determined voltages at their 2nd cycle.....	97

## List of Tables

Table 1. A comparison of metal elements in standard potential, capacities and ionic radius [19].....	6
Table 2. Element detection limit of ICP-MS. ....	45
Table 3. Capacity retention at a current density of 5 C at room temperature. ....	72
Table 4. Capacity retention of ball-milled V <sub>2</sub> O <sub>5</sub> sample with a current density of 5 C at different temperatures. ....	74
Table 5. EIS measurement results at room temperature. ....	77
Table 6. EIS measurement results at 60°C.....	78
Table 7. Concentrations for each element in ZNVO sample. ....	84

## List of Abbreviations

AC	Alternating current
AGM	Absorbed glass mat
AIBs	Aluminum-ion batteries
ARBs	Aqueous rechargeable batteries
CNTs	Carbon nanotubes
CC	Constant current
CVD	Chemical vapor deposition
CV	Cyclic voltammetry
DC	Direct current
EELS	Electron energy loss spectroscopy
EIS	Electrochemical impedance spectroscopy
FTIR	Fourier transform infra-red spectroscopy
HRTEM	High-resolution transmission electron microscopy
ICP-MS	Inductively coupled plasma mass spectrometry
KIBs	Potassium-ion batteries
LIBs	Lithium-ion batteries
MIBs	Magnesium-ion batteries
MWCNTs	Multi-wall carbon nanotubes
PANI	Polyaniline

PBAs	Prussian blue analogs
PPy	Polypyrrole
RAZBs	Rechargeable aqueous zinc-ion batteries
$R_{ct}$	Charge transfer resistance
$R_s$	Equivalent serial resistance
SAED	Selected area electron diffraction
SEM	Scanning electron microscopy
SHE	Standard hydrogen electrode
SIBs	Sodium-ion batteries
TGA	Thermogravimetric analysis
XPS	X-ray photoelectron spectroscopy
XRD	X-ray diffraction
ZIBs	Zinc-ion batteries

# **Chapter 1. Aqueous Zinc-ion Battery Systems: Introduction, Limitations, and Research Motivations**

## **1.1 Introduction**

In a world increasingly uncertainly about climate change, a sliver of hope has been offered via the surge in the generation of renewable energy over the past 20 years. The electricity can be produced by renewable energy resources with fewer environmental impacts. It is conceivable to make renewable energy sources produce electricity without generating carbon dioxide (CO<sub>2</sub>) because CO<sub>2</sub> emission is the major cause of global climate change [1]. Figure 1 represents the Energy Outlook in 2018, it shows the steady growth in overall energy consumption through 2040. This report predicts that oil and coal will provide smaller shares of energy in the future; the global demand for green, renewable and sustainable energy sources are growing rapidly and taking larger shares [1]. However, difficulties, e.g. the randomness and volatility of wind and solar power, show a big challenge on the cost of renewable energy storage [1]. Therefore, large-scale battery installations are springing up across electricity grids worldwide because they possess high energy efficiency, long cycle life and are independent from geographical conditions.

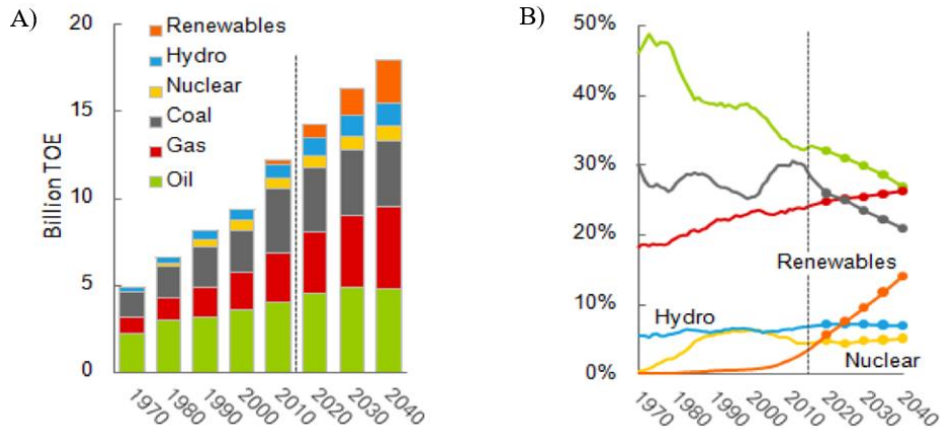


Figure 1. A) Worldwide primary energy consumption, by fuel, 1970-2040; B) share of primary energy consumption, by fuel, 1970-2040 [1].

The forecast for global demand for lithium-ion batteries is shown in Figure 2. The report is expected that the demands for batteries used in electric-vehicles and energy storage are growing dramatically [2]. Lithium-ion batteries (LIBs) are the most successful rechargeable batteries for portable electronic devices and electric vehicles. Nevertheless, with the theoretical limits of lithium-ion batteries approaching and their safety concerns, researchers are hard at work pursuing other strategies on battery developments [2]. One effective way is to simply replace the lithium anode by another metal, such as sodium, magnesium or zinc, with much lower cost of production and they may have dramatically higher energy density potential than the present technologies [3]-[5].

## Global demand for lithium-ion batteries

2005-2040P, by end use, GWh

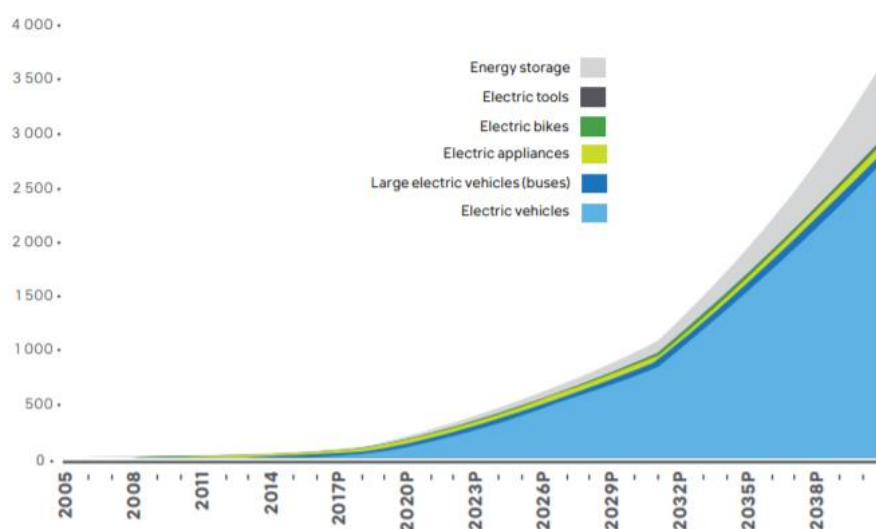


Figure 2. Global demand for lithium-ion batteries, 2005-2040 [2].

## 1.2 Rechargeable Aqueous Zinc Ion Batteries (RAZBs)

Because of the limited lithium resources, high cost and safety concerns of LIBs, new large-scale energy storage systems need to be explored as alternatives [2]. Although other types of metal ion batteries, such as sodium-ion batteries (SIBs) and potassium-ion batteries (KIBs), possess abundant element resources and similar chemical properties to LIBs, the high cost of battery operation, low energy density and safety issues of electrolytes are restricting their further developments on large-scale energy applications [3]-[5]. To reduce the toxic and flammable risks of electrolytes, aqueous electrolytes are under development. The aqueous electrolytes generally

provide higher ionic conductivity (can be up to  $1 \text{ S}\cdot\text{cm}^{-1}$ ) at 2 orders of magnitude than that of nonaqueous ones ( $1\text{--}10 \text{ mS}\cdot\text{cm}^{-1}$ ) [6].

Aqueous rechargeable batteries (ARBs) based on multivalent carriers, involving aluminum-ion batteries (AIBs), magnesium-ion batteries (MIBs) and zinc-ion batteries (ZIBs), are plausible alternative to LIBs since more electrons are involved in the redox reactions, so that higher energy density and discharge capacity would be offered [7]-[9]. Nonetheless, both AIBs and MIBs exhibit passivation and corrosion on their anode surface in aqueous electrolyte ( $4 < \text{pH} < 8$ ) [10]-[12]. The corroded anode inhibits metal ion diffusion and transportation, leading to lower battery efficiency and electrode potential in ARB systems [7][13][14].

With this regard, rechargeable aqueous zinc-ion batteries (RAZBs) with mildly acidic electrolyte hold a particular promise for large-scale energy storage system (as shown in Figure 3). The choice of anode is zinc since it has low-cost (USD 2 / kg), high safety and environmental friendliness on manufacturing [15]-[18]. It is widely used in combination with a large variety of cathode compounds since it has a very high theoretical specific capacity of up to  $820 \text{ mAh}\cdot\text{g}^{-1}$  [21] [23][24], and the smaller ionic radius of  $\text{Zn}^{2+}$  ( $0.75 \text{ \AA}$ ) allows it to insert / extract into / from the lattice of cathode materials without damaging the original structure (as listed in Table 1). Additionally, zinc has a low standard redox potential of  $-0.763 \text{ V}$  vs. standard hydrogen electrode (SHE) which offers zinc metal have low electrochemical stability in aqueous environment and the metal is susceptible to excessive hydrogen production when it

contacts with aqueous based electrolytes [20] [23]. Therefore, this RAZB system would exhibit a significant potential to alternate large scale energy storage devices with electrolyte safety, environmental and economical friendliness.

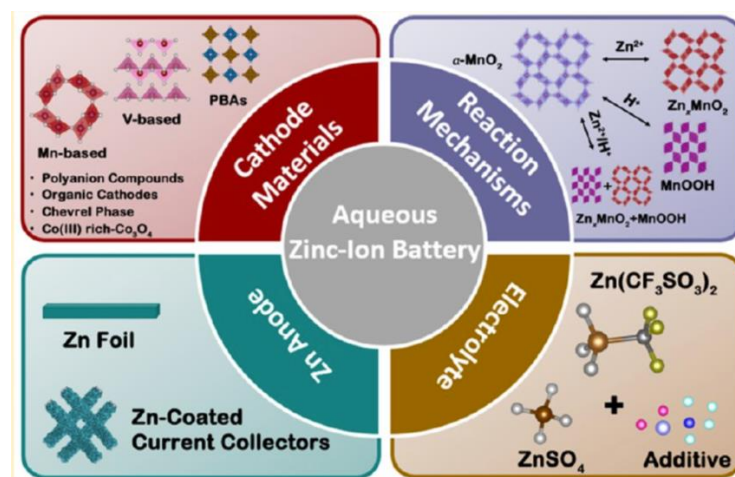


Figure 3. Aqueous zinc-ion battery system [24].

Major problems on the zinc electrode include the formation of solid-state inert  $Zn^{2+}$  species (e.g. zinc hydroxide, zinc sulfate hydroxide hydrate...) as oxidized products when zinc is reducing water to produce hydrogen gas and zinc dendrite, which give rise to the low coulombic efficiency and capacity fading. Part of these problems are suppressed using the near neutral or just slightly acidic electrolyte ( $3 < pH < 6$ ). However, the higher dimension of hydrated ionic radius of zinc ions in Table 1 may buffer the charge density of the  $Zn^{2+}$  and toughen the ion insertion into the cathode material structure [19][22]. Therefore, exploring a compound with high reversible structure (tunnel-type or layered-type) which is capable of multivalence cation charge-storage (zinc ions insertion / extraction) is necessary.

Element	Standard potential [V] versus SHE	Specific capacity [mAh g <sup>-1</sup> ]	Capacity density [mAh cm <sup>-3</sup> ]	Ionic radius [Å]	Hydrated ionic radius [Å]
Li	-3.040	3860	2061	0.76	3.40–3.82
Na	-2.713	1166	1129	1.02	2.76–3.60
K	-2.924	685	610	1.38	2.01–3.31
Mg	-2.356	2206	3834	0.72	3.00–4.70
Ca	-2.840	1337	2072	1.00	4.12–4.20
Zn	-0.763	820	5855	0.75	4.04–4.30
Al	-1.676	2980	8046	0.53	4.80

Table 1. A comparison of metal elements in standard potential, capacities and ionic radius [19].

### 1.3 Cathode Materials for Zinc-ion Battery System

To date, many compounds have been reported as the cost-efficient and high-performance cathode materials for advanced ZIBs, and such a tremendous interest has been raised in developing a material that accommodating zinc ions during the cycling. Manganese-based materials have been researched over 150 years due to their abundant resources on the earth and multiple oxidation states of manganese (Mn) ( $\text{Mn}^{2+}$ ,  $\text{Mn}^{3+}$ ,  $\text{Mn}^{4+}$ ). A remarkable variety of multivalence phases and crystal structures are exhibited in manganese oxide and hydroxide minerals [19]. However, due to the intrinsically poor electrical conductivity and unstable structure of  $\text{MnO}_2$  during the charge / discharge process, it cannot satisfy the requirement of ZIBs [30][31]. Prussian blue analogs (PBAs)  $\text{MFe}(\text{CN})_6$  ( $\text{M} = \text{Fe}, \text{Co}, \text{Ni}, \text{Cu}, \text{Mn} \dots$ ) have attracted scientists attentions due to their unique crystal structure, prominent structural stabilities and sufficient redox-active sites [32][33]. The zinc ion reversible and facile transportation in cathode can be

realized by the large interstitial sites and special tunnels of PBAs [19]. Nonetheless, the research of PBAs is developed in recent 5 years and the studies of this material class still on the early stage. The active sites are easily blocked off because of the unsatisfactory synthesis method which forming lattice defects and vacancies; moreover, their relative low specific capacity and short cycle life give rise to poor electrochemical performance on ZIBs [19][34]. Additionally, other organic cathode compounds, such quinone compounds and 9,10-di(1,3-dithiol-2-ylidene)-9,10-dihydroanthracene (ex-TTF), have been reported recently [35]-[37]. However, the dissolution of discharge products and anode corrosion lead to poor cycle life of these organic cathodes in ZIBs, and the toxicity of quinones also arouses safety concerns [19]. Therefore, vanadium-based compounds draw growing interests in the last decades due to their eminent redox properties and multiple vanadium oxidation states.

### **1.3.1 Layered Vanadium Oxide ( $V_2O_5$ ) as the Cathode Material**

Vanadium-based compounds have been studied as potential cathode materials in various battery systems for about 40 years. In comparison with other types of cathode materials mentioned in above section, vanadium-based compounds possess relatively high operating voltages and specific capacities in RAZBs, as shown in Figure 4 [24]. In particular, two key advantages of vanadium-based material over others, including stability and diversity, offer this kind of material as a promising cathode in ZIB system

[54]. As shown in Figure 5, a large family of V-coordination polyhedral contains tetrahedron, trigonal and square pyramids, distorted octahedron and regular octahedron with changes of vanadium (V) oxidation states, providing various open framework for reversible zinc ions insertion / extraction without breaking their original structures [19][55][56].

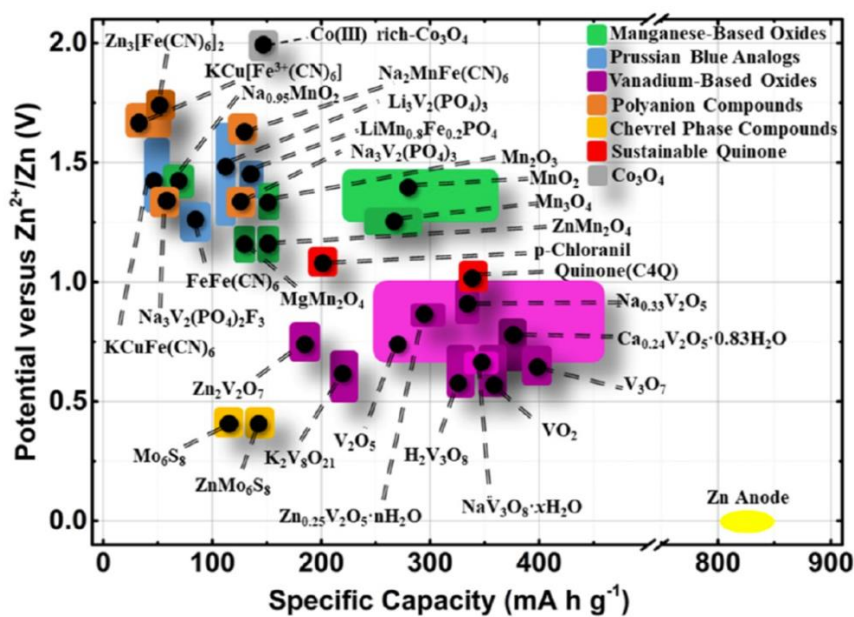


Figure 4. The operating potential and specific capacity for various cathode materials in aqueous ZIBs [24].

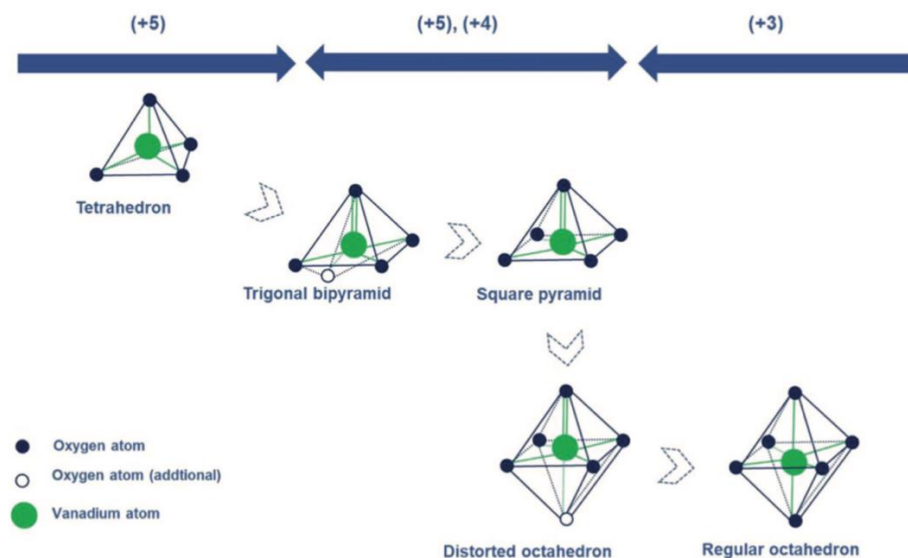


Figure 5. The corresponding vanadium coordination polyhedral to vanadium valence [39].

The compound vanadium pentoxide ( $V_2O_5$ ) with layered structure has been chosen as the host material in RAZB system due to its abundant resources, low cost, easy preparation, high energy density and safety properties [39]-[43]. The rich chemistry, morphology and crystal structure make it become a promising material for applications of artificial muscles, actuator, sensors and electrochromic windows [44]-[47]. Comparing with other vanadium-based compounds, layered  $V_2O_5$  with the lowest molecular weight and the simplest lattice structure is treated as the reference point to measure their electrochemical performance.

The weak Van der Waals forces hold layers of  $V_2O_5$  together and its most commonly crystallinity is orthorhombic structure [48][49]. The orthorhombic structure of  $V_2O_5$  is shown in Figure 6, each single layer of  $V_2O_5$  consists of edge- and corner-

sharing square pyramids, the vanadium-oxygen interactions which orthogonal to the *c*-direction linking  $V_2O_5$  slabs together [48]. Additionally, there are three types of oxygen center refer to O1, O2, O3 in each  $V_2O_5$  sheet. The terminal / apical and bridging (corner-sharing) coordinated vanadyl oxygen atoms O1, O2, have respectively V-O bond length of 1.54 Å and 1.77 Å. The triply coordinated O3 in  $VO_5$  square pyramids connects three neighboring V atoms via edge-sharing with corresponded bond lengths of 1.88 Å, 1.88 Å and 2.02 Å [48]. The combination of short vanadyl bond and the layered structure mainly determine the electronic and thermal properties of  $V_2O_5$  [50].

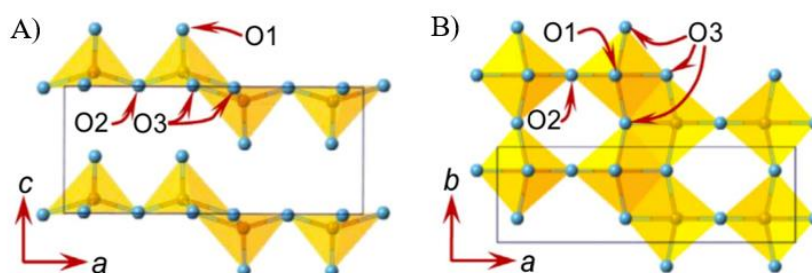


Figure 6. The orthorhombic structure of  $V_2O_5$  in A) *ac* plane and B) *ab* plane [49].

Moreover, another typical  $V_2O_5$  form is hydrated vanadium pentoxide denoted as  $V_2O_5 \cdot H_2O$  xerogels, which uses heat treatment to convert this compound into orthorhombic  $V_2O_5$  at a specific temperature [51][52]. Figure 7 exhibits the crystal structure of  $V_2O_5 \cdot H_2O$  xerogels.  $V_2O_5 \cdot H_2O$  xerogel consists of  $V_2O_5$  bilayers with water molecules inserted into its interlayer, where water molecules play a significant role to separate and stabilize  $V_2O_5$  bilayer with a distance of 11.5 Å.

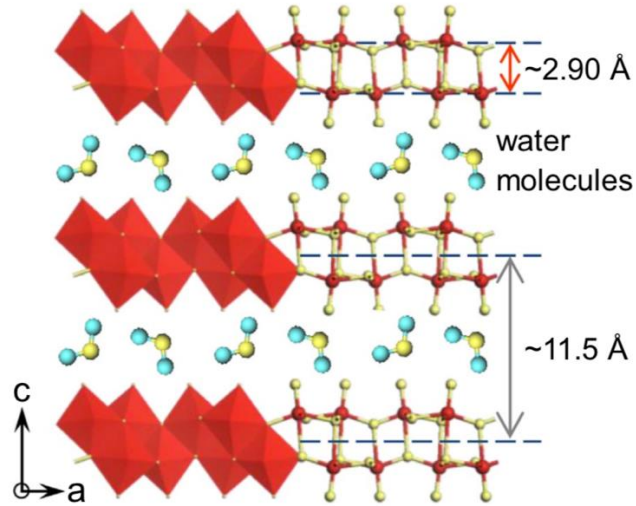
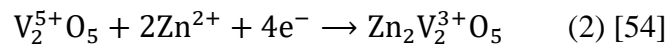
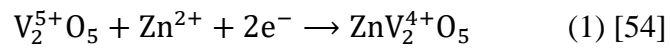


Figure 7. Schematic of the crystal structure of  $V_2O_5 \cdot H_2O$  xerogels [53].

Notably, the theoretical capacities of  $V_2^{5+}O_5$  with one  $Zn^{2+}$  intercalation is calculated in  $294.5 \text{ mAh} \cdot \text{g}^{-1}$ , and for  $V_2O_5$  varies from  $V^{5+}$  to  $V^{3+}$  with two  $Zn^{2+}$  transportation is measured in  $589.0 \text{ mAh} \cdot \text{g}^{-1}$  [54]. The reactions of forming  $Zn_xV_2O_5$  are shown in Equation 1 and 2:



The extraction / insertion of Zn ions from / into  $V_2O_5$  bilayer to form  $Zn_xV_2O_5$  during cycling process is exhibited in Figure 8.

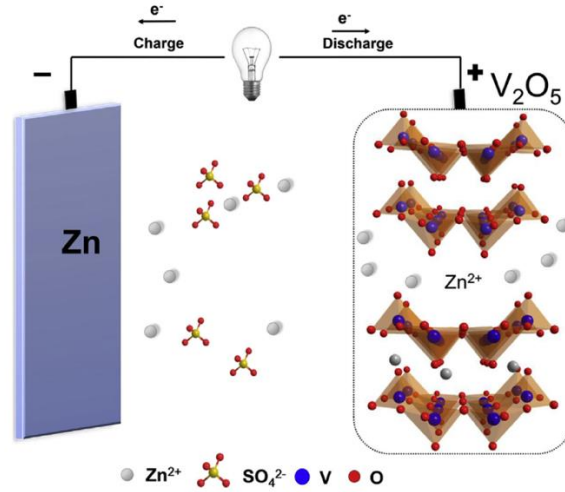


Figure 8. Schematic of the  $V_2O_5$  cathode with 2 M  $ZnSO_4$  aqueous electrolyte in RAZB system [57].

### 1.3.2 Limitations of $V_2O_5$ Cathode in Aqueous Batteries

Although  $V_2O_5$  possesses easy preparation, low cost and safety properties as the cathode material for next-generation ZIBs, the applications of  $V_2O_5$  have been limited owing to its low electrical conductivity, poor structural stability during the ion de- / intercalation, serious dissolution in acidic aqueous electrolytes and thermal stability issues [25]-[29] [58]-[60]. These shortcomings influence the kinetic energies of both electrons and ions during the transportation between the aqueous electrolyte and electrodes, this kinetic problem makes the case of requiring large specific capacity at high current densities more difficult [49]. Multiple strategies have been proposed to reduce the effects of  $V_2O_5$  poor structural stability and improve the electrochemical

performance of Zn // V<sub>2</sub>O<sub>5</sub> battery in the past few decades. The details and examples will be discussed in the following section.

### **1.3.3 Strategies to Overcome V<sub>2</sub>O<sub>5</sub> Cathode Limitations in Aqueous Batteries**

The poor electrical conductivity and serious dissolution of cathode material V<sub>2</sub>O<sub>5</sub> into acidic aqueous electrolyte limit the battery cyclability, three superior strategies involving material nanostructuring, surface coating and chemical doping are proposed to thwart this condition. Consequently, the electrochemical performance of Zn // V<sub>2</sub>O<sub>5</sub> batteries has been significantly improved with long term cycle stabilities, reversible specific capacities and high rate capabilities.

#### **Nanostructuring**

The diffusion path lengths of both ions and electrons between aqueous environment and electrodes have been reduced, which relying on the construction of nanostructured materials. Nanostructuring, one of the most effective proposed strategies, is capable of producing high performance cathode materials for ZIBs. Commonly, the synthesized materials with diverse nanostructures (e.g. wires, rods, tubes, belts, sheets and spheres) in nanoscale possess larger specific surface areas [61][62]. Therefore, high contact area between the nanostructured material and the electrolyte would offer large active interfacial area to enhance rate capability [63]. Furthermore, the synthesized cathode materials generally have higher sustainability during the cycling process with the

comparison of the commercial or natural materials [64]. The nanostructured material also possesses the advanced morphology, which shortens the distance of electrons and ions transportation, benefits their kinetic acceleration consequently [62][65].

Li *et al.* fabricated a high product yield  $V_2O_5$  nanobelts by hydrothermal method with the usage of  $H_2O_2$  and  $V_2O_5$  suspension [66]. The single-crystalline  $V_2O_5$  nanobelts with larger specific surface area, whose width and thickness in nanometer and length in micrometer as shown in Figure 9, delivered a high specific discharge capacity of  $288 \text{ mAh}\cdot\text{g}^{-1}$  which was more than twice as the commercial  $V_2O_5$  [66].

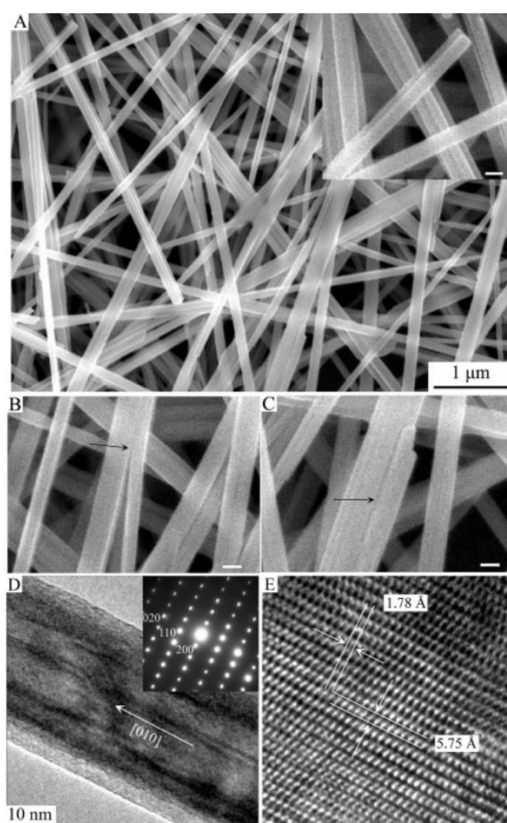


Figure 9. Typical SEM (A-C) and TEM (D and E) images of single-crystalline  $V_2O_5$  nanobelts. The inserted patterns in A and D are the cross-section of  $V_2O_5$  nanobelts and SAED pattern, respectively. The scale bar corresponds to 100 nm [66].

Wang *et al.* reported three types of nanostructured  $V_2O_5$  material, involving porous  $V_2O_5$  nanotubes, hierarchical  $V_2O_5$  nanofibers and single-crystalline  $V_2O_5$  nanorods, via electrospinning technique followed with annealing [67]. The synthesis processes are illustrated in Figure 10. It is notable that the morphology of the nanostructured materials is controlled by the different annealing temperatures, which is the uniqueness of this strategy. Consequently, these kinds of cathode materials in their battery systems displayed high reversible discharge capacities and superb cycling performance; moreover, the ion diffusion and electrolyte penetration were enhanced based on the advanced nanostructure [67].

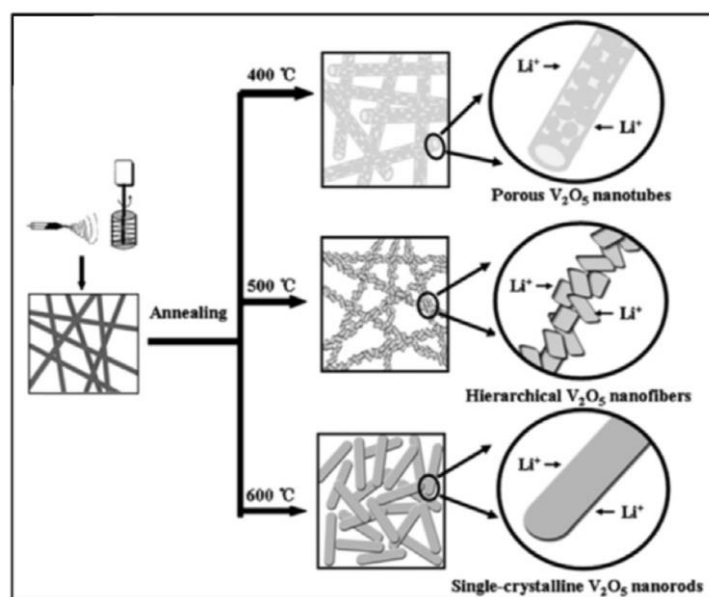


Figure 10. Schematic of producing nanostructured  $V_2O_5$  material by electrospinning method and subsequent annealing [67].

Li *et al.* used a facile sol-gel method combined with freeze-drying technique and subsequent annealing to synthesize a two-dimensional leaf-like  $V_2O_5$  nanosheets [68]. The preparation process is schematically exhibited in Figure 11. This material displayed a promising discharge capacity and rate capability, it can deliver a capacity of  $104 \text{ mAh}\cdot\text{g}^{-1}$  even at a high current density of  $5 \text{ A}\cdot\text{g}^{-1}$  [68]. Additionally, a discharge capacity of  $206 \text{ mAh}\cdot\text{g}^{-1}$  was reached at  $0.5 \text{ A}\cdot\text{g}^{-1}$  after 100 cycles, and a small capacity fading rate (merely 0.22% per cycle) demonstrated a superior capacity retention during cycling [68].

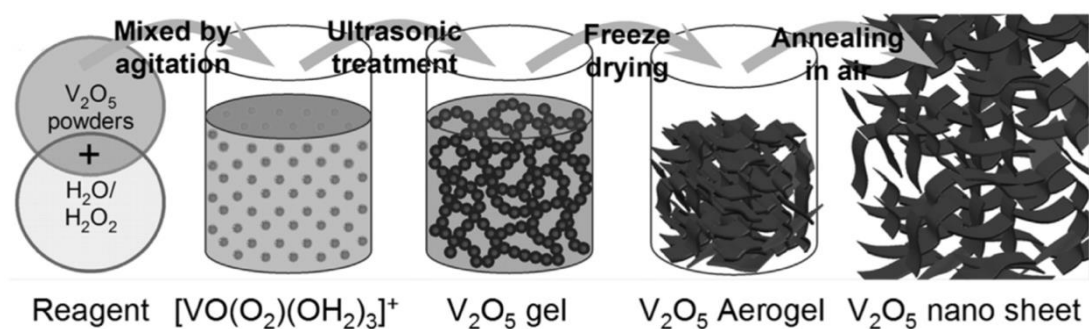


Figure 11. Schematic of two-dimensional leaf-like  $V_2O_5$  nanosheet production process [68].

Apart from the synthesis techniques mentioned above, other methods containing chemical vapor deposition (CVD) [69][70], dissolution-splitting method [71][72], membrane filtration technique [73], hydrolysis method... [74] have been used to synthesis advanced nanostructured  $V_2O_5$  cathode materials.

### **Surface coating**

The surface structure of the electrode material has been verified as a crucial part for the electrochemical performance of metal-ion batteries. The facile strategy, surface coating, has been intensively investigated by many scientists to enhance the cyclic stability and rate performance in their battery systems. Carbon and conductive polymers as two typical coating materials are widely used in battery studies since their electron-conducting properties promote the charge transfer on the particle surface [75]. The coating material as a physical protection barrier inhibits particle aggregation and buffer the stress of inner nanoparticles, improving the chemical stabilities of the active cathode materials [76]. The commercial  $V_2O_5$  particles are slightly dissolved in water, exposing  $V_2O_5$  nanoparticles in an aqueous electrolyte for a long time would lead its structure collapsing and crushing. Therefore, this surface modification strategy assists to protect  $V_2O_5$  structure and provide stable cyclability in the aqueous environment.

Zhang's group prepared carbon-coated  $V_2O_5$  nanocrystals by using a hard template of porous carbon via the capillary induction technique [77]. Figure 12 exhibits the preparation of this carbon-coated  $V_2O_5$  composite. This material, whose particle size ranging from 10-20 nm, displayed a high reversible capacity, long cycle life and good rate performance [77]. The small particle size assisted to dramatically shorten the ion diffusion and transport lengths on the surface of  $V_2O_5$  nanocrystals; moreover, the carbon coating enhanced the electrical conductivity of  $V_2O_5$  electrode, and it stabilized the  $V_2O_5$  crystalline structure via reducing the side reactions between the electrode material and electrolyte during the cycling process [77].

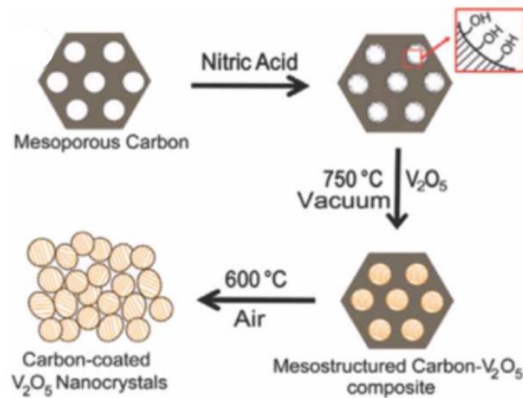


Figure 12. Schematic of the preparation of carbon-coated V<sub>2</sub>O<sub>5</sub> composite [77].

Zhou's research group synthesized a hybrid composite, multi-wall carbon nanotubes (MWCNTs) / V<sub>2</sub>O<sub>5</sub>, via hydrothermal treatment combined with a post-sintering process, and the particle size was controlled under nanometer scale (as shown in Figure 13) [78]. The superb electrochemical results were provided by this electrode material in LIBs. It delivered a large initial discharge capacity of 402 mAh·g<sup>-1</sup> at a current density of 0.1 A·g<sup>-1</sup> vs. Li / Li<sup>+</sup>, and maintained a capacity of 222 mAh·g<sup>-1</sup> after 50 cycles; moreover, it also reached 194 mAh·g<sup>-1</sup> even at a large current density of 0.8 A·g<sup>-1</sup> [78]. This electrochemical performance is due to the superior mechanical properties of carbon nanotubes (CNTs), which possess huge tensile strength and strain tolerance [79]-[81]. Additionally, CNTs with high specific surface area, electrical conductivity and chemical stability, making them act as a promising coating material in battery researches [79]-[81].

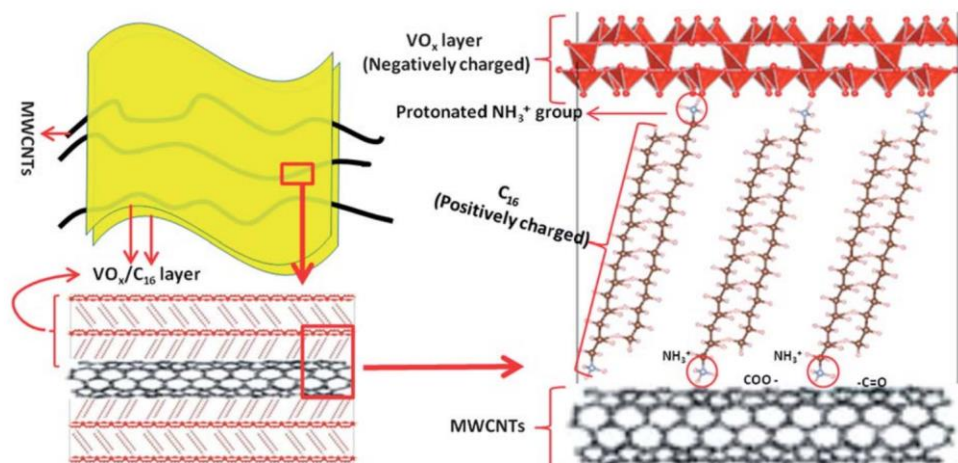


Figure 13. Schematic of hybrid MWCNTs /  $V_2O_5$  composite formation via hydrothermal method [78].

Li *et al.* reported a simple in-situ polymerization method without adding surfactants to form a polymer coated electrode material. As shown in Figure 14, the one-dimensional  $V_2O_5$  nanobelts were uniformly coated with the conductive polymer polyaniline (PANI) [82]. The authors investigated influences of pH values and additional initiators for the morphology of  $V_2O_5$  / PANI nanobelts, and the most appropriate conditions for polymerizing PANI on single crystalline  $V_2O_5$  nanobelts in its emeraldine state was related [82]. This resulting product exhibited a significantly enhanced electrical conductivity and environmental stability, it was considered as a promising cathode material in reversible metal-ion batteries [82].

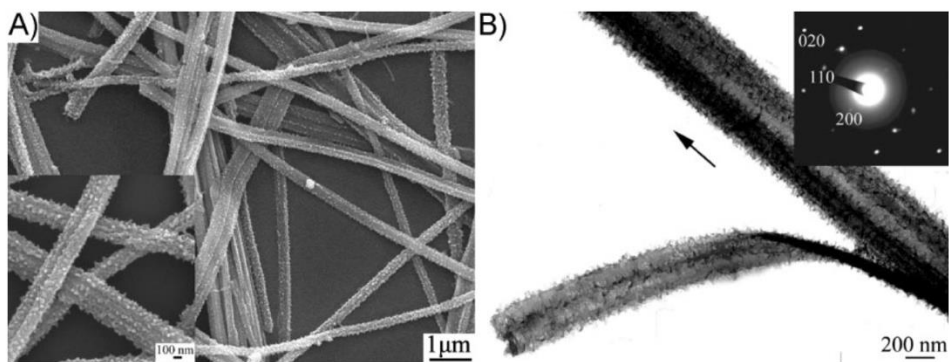


Figure 14. A) SEM and B) TEM images of  $V_2O_5$ / PANI nanobelts [82].

Other than carbon and conductive polymers, some inorganic coating materials involving  $SiO_2$  and  $TiO_2$  have been studied to improve the battery performance [83]-[85]. However, the oxides applied on the active material surface may limit the transportation of zinc ions, or other transport properties of the battery cathode [86][87].

### **Metal ion doping**

Metal-doped (M-doped) materials come into notice owing to their advanced structures and versatile electronic states, which providing superior structural stabilities and suppressing the loss of capacities during cycling [88]. A large variety of cations, such as  $Na^+$ ,  $Mg^{2+}$ ,  $Zn^{2+}$ ,  $Cu^{2+}$ ,  $Al^{3+}$ , have been investigated and used as the doping metal ions into  $V_2O_5$  lattice, and lead to distinct properties which observed on the doped materials, such as higher specific capacities and better rate capabilities [89]-[94]. Because of the formation of lower valence states of V ion ( $V^{3+}$  and  $V^{4+}$ ) with doping metal ions into the host  $V_2O_5$  lattice, the electronic conductivity would be remarkably increased [90][95]. The  $MO_6$  octahedral unit, which is formed by the inclusion of metal ions, is capable of stabilizing the  $V_2O_5$  layered structure during Zn ion insertion /

extraction, and offering beneficial structural stability during the cycling process [94][95]. The local structural defects of  $V_2O_5$  is led by foreign metal cations, this cathode material exhibits an enhanced cycle life during reversible Zn intercalation since the possible nucleation centers for phase transformation have been produced and the defects supply more pathways for ion diffusion [91]. Additionally, lower charge transfer resistance ( $R_{ct}$ ) and higher Faradic reaction kinetics would be realized by producing this cathode material [91].

Kundu *et al.* fabricated a vanadium oxide bronze ( $Zn_{0.25}V_2O_5 \cdot nH_2O$ ) intercalated by  $Zn^{2+}$  and crystalline water, which was synthesized in nanobelts structure by microwave hydrothermal method and assembled with aqueous electrolyte and zinc metal anode [94]. A high reversible capacity of  $300 \text{ mAh}\cdot\text{g}^{-1}$  at a current density of  $0.05 \text{ A}\cdot\text{g}^{-1}$  was achieved in this battery system, and it also delivered a large energy density of  $450 \text{ Wh}\cdot\text{L}^{-1}$  [94]. Even at  $4.5 \text{ A}\cdot\text{g}^{-1}$ , this pillared material still provided a capacity of  $233 \text{ mAh}\cdot\text{g}^{-1}$  and exhibited a high capacity retention over 80% within 1000 cycles [94]. These superb electrochemical performances were based on the reversible Zn ion de- / intercalation storage process with more than one  $Zn^{2+}$  per formula unit, and water molecules assisted to expand and contract  $V_2O_5$  interlayer distance for fluent diffusion of Zn ions [94]. Furthermore, the dendrite formation on zinc anode was reduced significantly due to the choice of inserted metal ion  $Zn^{2+}$ , which was the content of the anode [94]. The discharge process of Zn //  $Zn_{0.25}V_2O_5$  battery in 1M  $ZnSO_4$  electrolyte is schematically displayed in Figure 15.

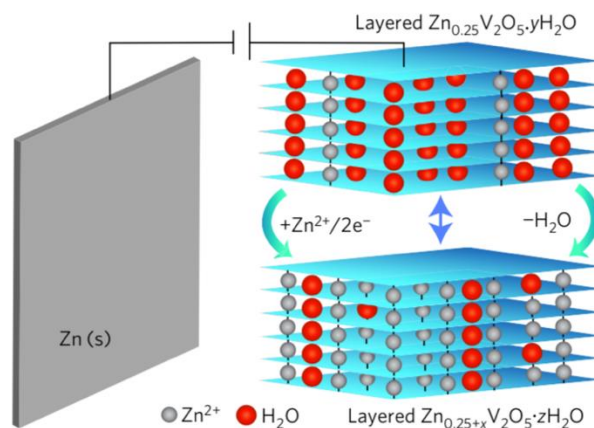


Figure 15. Schematic of Zn //  $\text{Zn}_{0.25}\text{V}_2\text{O}_5$  battery in 1M  $\text{ZnSO}_4$  electrolyte [94].

He's group reported the design of cathode material via insertion Na ions into  $\text{V}_2\text{O}_5$  interlayer to fabricate a nanowire structural electrode, the cell prepared from this material delivered a high capacity of  $367.1 \text{ mAh}\cdot\text{g}^{-1}$  at  $0.1 \text{ A}\cdot\text{g}^{-1}$  [95]. This advanced material exhibited a long-term cyclic stability of 93% capacity retention within 1000 cycles under a high-current density ( $1 \text{ A}\cdot\text{g}^{-1}$ ) [95]. Since the inserted Na ions, whose ionic radius (102 pm) was larger than that of  $\text{Zn}^{2+}$  (74 pm), acted as pillars between the  $\text{V}_2\text{O}_5$  interlayer to stabilize its layered structure. The reversible phase transformation was formed for Zn ion de- / intercalation during charge / discharge process, which is displayed in Figure 16 [95]. The  $\text{V}_2\text{O}_5$  volume expansion or contraction was buffered, and the dissolution of  $\text{V}_2\text{O}_5$  into the aqueous environment also had been suppressed [95]. Additionally, the metal ions in the  $\text{V}_2\text{O}_5$  interlayer significantly improved the

electrical conductivity [95]. Therefore, the structural stability of this kind of cathode material was enhanced and side reactions were inhibited during cycling.

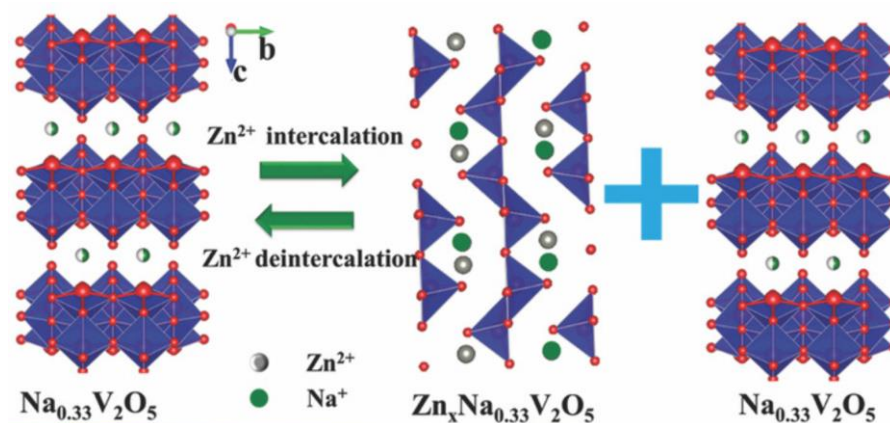


Figure 16. Schematic of Zn ion de- / intercalation in the  $\text{Na}_{0.33}\text{V}_2\text{O}_5$  electrode [95].

## 1.4 Polymeric Species

Polymers with a wide variety of functional groups are arguably the most common form of organic molecules. Conductive polymers gain further enhanced interests in battery research field due to their highly reversible redox behavior and unusual combination properties with other species [98]. Polyaniline (PANI) and polypyrrole (PPy) are considered as suitable candidates to coat cathode materials in rechargeable batteries due to their superb electrical conductivity and thermal stability [82] [97]-[100]. Additionally, the ease of fabrication and processing, the low cost of production and light weights make these conductive polymers as promising materials for surface coating [100].

The conductive polymer backbone contains both  $\sigma$ -bond and  $\pi$ -bond, and the bonds between carbons alternate single and double in  $\pi$ -conjugated system [101] [102]. As a result, the delocalized electrons in the conjugated double bond move along the backbone which allows current flow [101] [102]. Because of the conjugated double bond presents along the carbon chain, the insulated structure can be transformed into metallic one [99] [101]. Moreover, to achieve much higher electrical conductivity of conductive polymer, doping strategy has been used to carry more electron to its backbone [102]. PPy is one of the most popular heterocyclic polymers which exhibits good electrical conductivity in its quinoid form (doped state) (in Figure 17 A), this is because the quinoid form has lower energy band than its aromatic form [104]. In Figure 17 B), the polymer PANI contains planar aromatic amine chains possesses desired conductivity in its emeraldine (half-oxidized state) base [104].

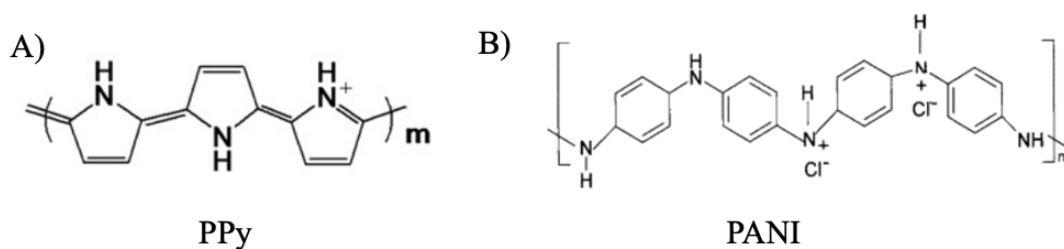


Figure 17. The structures of A) PPy and B) PANI [104].

In-situ polymerization method is used to form a compact film on the cathode material surface by conductive polymers [82] [100]. Compared with the conventional  $V_2O_5$ , the electrical contact is enhanced and exhibits significant improvements in

cycling performance as well as the ion and electron kinetics of this hybrid material [100][103]. In addition, the modified polymer layer serves as a barrier between the  $V_2O_5$  particles and the aqueous electrolyte, which buffers the  $V_2O_5$  volume dramatic contraction and prevents the connection and dissolution of  $V_2O_5$  from aqueous environment [98]-[103]. Therefore, conducting polymer plays a crucial role on surface modification of cathode material in RAZBs.

## **1.5 Electrolyte Optimizations to Suppress Dendrite Formation for RAZBs**

The usage of aqueous electrolyte benefits to transport guest ions and closely connect the cathode and anode [24]. Moreover, the low cost, ease of fabrication, high safety and good environmental friendliness make the aqueous electrolytes used widely in ZIBs [24]. However, the zinc dendrite formation is still against the cyclic stability of RAZBs. The sharp zinc protuberances can pierce the separator and finally leads to the direct connect of the cathode and anode, causing short circuits in the battery interior eventually. Therefore, electrolyte additives win an enhanced insight in battery research field.

In this research, the solution 2M  $ZnSO_4$  is used as the electrolyte in all Zn // vanadate battery system. To improve the Zn stripping / plating coulombic efficiency and cyclic performance, the salt  $Na_2SO_4$  is added into the electrolyte solution. Since the  $Na^+$  (-2.71 V) has much lower reduction potential than  $Zn^{2+}$  (-0.76 V), Na ions are

preferentially attracted by the negatively charged Zn protuberance which has a strong electric field, forming a positively shield around the sharp tip [106], as illustrated in Figure 18. Because of the repulsive force between same charged ions, the coming  $\text{Zn}^{2+}$  can be repelled to distribute on adjacent substrate [106]. According to the electrostatic shield mechanism, the zinc dendrite deposition has been inhibited effectively [105]-[107]. Moreover, adding Na ions in electrolyte changes the dissolution equilibrium of Na ions from the positive electrode, thus the continuous damage of cathode material would be impeded [106]. Chen' group reported a dual-carrier electrolyte system in Zn // sodium vanadate (NVO) aqueous battery [105]. The addition of  $\text{Na}^+$  ions in 1M  $\text{ZnSO}_4$  electrolyte was able to suppress the NVO nanowires dissolution and zinc dendrite deposition on anode [105]. This resulted the Zn // NVO aqueous battery delivered a high discharge capacity ( $250 \text{ mAh}\cdot\text{g}^{-1}$ ) at  $1 \text{ A}\cdot\text{g}^{-1}$  and stable cyclic performance over 82% after 1000 cycles [105].

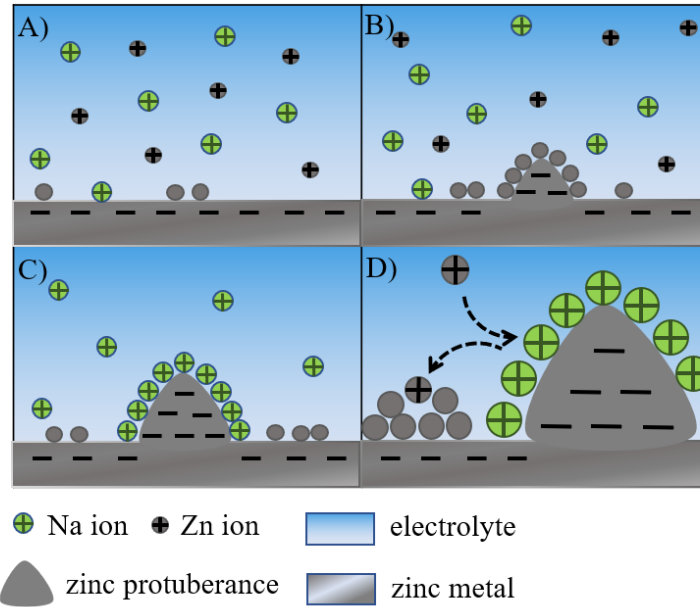


Figure 18. Illustration of zinc deposition process based on electrostatic shield mechanism.

## 1.6 Project Scope and Objectives

Overall, the work in this thesis is based on two main objectives:

- 1) Fabricating a thermally stable cathode material in RZAB. In this project, we aim to reduce the dissolution of  $V_2O_5$  in aqueous electrolyte and improve its thermal stability at high temperature. Thus, surface coating strategy is employed to modify  $V_2O_5$  surface by using conductive polymers.
- 2) Synthesizing a new type of vanadium-based cathode material by dual metal-ion intercalation ( $Zn^{2+}$  and  $Na^+$ ). As doping metal-ion into the  $V_2O_5$  structure offers more transfer electrons during cycling, a higher discharge capacity of Zn// vanadate aqueous battery is expected to achieve. Additionally, because of the electrostatic

shield mechanism, zinc dendrite formation can be inhibited. Therefore, this dual-ion electrode assisted with a dual-ion electrolyte (2M ZnSO<sub>4</sub>+2M Na<sub>2</sub>SO<sub>4</sub>) will provide an enhanced cyclic stability.

## **Chapter 2: Material and Electrochemical Characterization Techniques**

This section will explain expand on the characterization techniques that will be used to explore various electrochemical and structural properties over the course of experimentation.

### **2.1 Material Characterization Techniques**

#### **2.1.1 X-Ray Diffraction (XRD)**

X-ray diffraction (XRD) is a rapid analytical technique primarily used for identifying the phase of a crystalline material or a mix of different crystalline materials. Through analysis, we get the structural information (e.g. atomic spacing, unit cell dimensions, atom position of each element) in the unit cell. The analyzed material is finely homogenized and ground, and average bulk composition can be determined consequently. This non-destructive tool can be used to analyze all kinds of matter- ranging from fluids, to powders and crystals as long as they possess some sorts of repeating long range orders [108]. From research to engineering and production, XRD is an indispensable method for characterizing materials and detecting qualities [108].

The instrument to implement XRD is named the X-ray diffractometer. In principle, all X-ray diffractometers consist of three basic elements: an X-ray tube (source), a sample holder, and an X-ray detector (shown in Figure 19) [109]. The X-ray tube generates X-rays by heating a filament to produce electrons, the electrons are

accelerated toward a target material under a high voltage and the bombarded the material surface to emit characteristic X-ray beams [110]. The specific wavelengths correspond the characteristics of target material (e.g. Cu, Fe, Cr), for instance, copper as the most common target material for single-crystal diffraction, has a Cu-K<sub>α</sub> X-ray wavelength of 1.542Å [113]. This X-ray will be bombarded on the materials while the angle between the beam and the reflected / diffracted signals is changing (Figure 19). The X-ray signals are recorded and processed via a detector, and the detector converts the signal to a count rate, then output to a device [111]. The obtained maximum intensity allows to do the calculation of the crystal structure details, or if we know the crystal structure, the wavelength of the incident X-rays upon the material can be determined by Bragg's law, which is expressed below:

$$n\lambda = 2d_{hkl}\sin\theta \quad (3)$$

where  $n$  is an integer,  $\lambda$  is the wavelength of X-rays characteristic which impinging on the analyzed sample,  $d$  is the interplanar spacing between atomic rows, and  $\theta$  is the angle of the X-ray beam with respect to the planes [110]. As illustrated in Figure 20, when the geometry of incident X-rays satisfies the Bragg Equation, the constructive interference and a peak in intensity could occur [112].

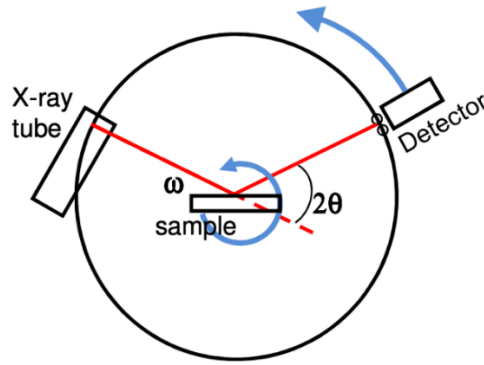


Figure 19. Schematic of XRD instrument.

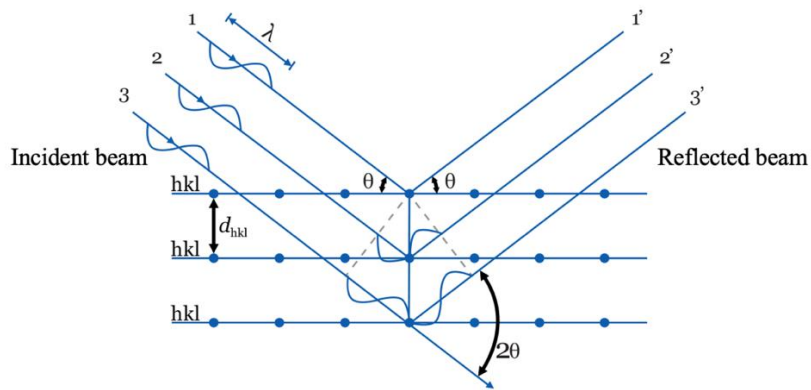


Figure 20. Schematic showing the interaction between X-rays and a typical crystalline sample [114].

Moreover, the synthesis and processing conditions of the measured sample may affect the size of crystal plane. Applying Scherrer equation (shown in equation 4) to calculate the size of the crystal from the XRD spectrum is an effective method.

$$d = \frac{K\lambda}{(\text{FWHM})\cos\theta} \quad (4)$$

where  $d$  is the crystal size,  $K$  is the Scherrer shape constant (in literatures, the common  $K$  values for spherical crystals are 0.94, for nanorods are 1.00, and for platelets are 0.89 [115]),  $\lambda$  is the X-ray wavelength, FWHM represents the full width at half maximum of the corresponding peak in the XRD spectrum, and  $\theta$  is the incidence angle.

In this work, XRD was used to determine the crystallinity of the vanadates material. The Brüker D8 Discover X-ray diffractometer with a copper target and a wavelength of 0.154 nm ( $\text{Cu-K}\alpha$ ) was used to carry all XRD experimentation in this project. For typical powder patterns, data was collected from  $\sim 5^\circ$  to  $70^\circ$  at a scan rate of 0.4 degrees per second.

### **2.1.2 Fourier Transform Infra-red Spectroscopy (FTIR)**

Fourier transform infra-red spectroscopy (FTIR) is one of the most straightforward way to obtain the infrared spectrum of materials allowing in different phases by infra-red (IR) light absorption or emission. FTIR spectroscopy is used to measure how much of the beam containing multiple different light frequencies are absorbed by the sample. The absorbed radiation with specific wavelength changes the dipole moment of the sample molecules, and the vibrational energy levels of sample molecules are excited from the ground state [116]. Consequently, the gap of the vibrational energy level determines the absorbed peak frequency. When a sample is exposed to IR radiation, some molecules of the sample selectively absorb the radiation

and some radiation is transmitted [117]. A spectrum is represented by the resulting signal at the detector, which acts as a molecular ‘fingerprint’ of the sample. Because different chemical structures can produce their corresponded spectral “fingerprints”, the infrared spectroscopy technique is becoming increasingly vital for material characterization.

The Michelson interferometer is a core setup of the FTIR spectrometer. As an example shown in Figure 21, this interferometer contains a beam splitter, a fixed mirror and a scanning mirror. The beam splitter made of a special material transmits half of the radiation and reflects the others [118]. Radiation from the infrared source attacks the beam splitter and separates into two pathways. One way is reflected off the beam splitter to attack the scanning mirror, which is shown in blue line (path 1); the other way (displayed in red line and named in path 2) is transmitted through the beam splitter to attack the fixed mirror [118]. Next, both the fixed and scanning mirrors reflect the radiation back to the beam splitter. Additionally, half of this reflected radiation occurs transmission and half is reflected by the beam splitter once again, leading the beam of path 1 passing to the detector and the beam of path 2 returning to the source [118].

In this work, FTIR spectroscopy was performed on a Brüker Optics Vertex 70 Spectrometer in a wavenumber range of  $400\text{ cm}^{-1}$  to  $4000\text{ cm}^{-1}$  with a repetition of 20 scans.

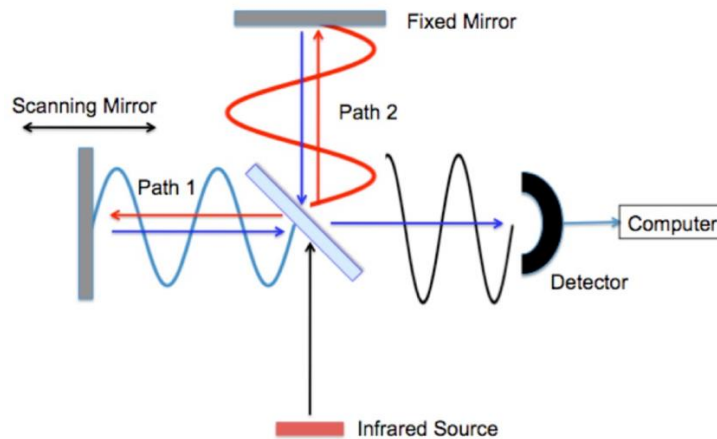


Figure 21. Working principle of an FTIR interferometer [118].

### 2.1.3 Scanning Electron Microscopy (SEM)

Scanning electron microscopy (SEM) is a powerful and versatile tool for characterizing material in high resolution. It is used to detect the surface structure, morphology, phase information and chemical composition of the solid object [120].

The main components of SEM containing electron source, electron lenses, electron detector, sample chamber and the data output device. The schematic of SEM is shown in Figure 22, the electrons carry significant amounts of kinetic energy are generated at the top of the column, then the produced electrons are accelerated to pass through a combination of lenses and apertures, and eventually, forming a focused electron beam to hit the surface of the sample [121]. Relying on the sample density and accelerating voltage, the electron beam passes through the sample with a few microns depth when it hits the sample surface [121]. The sample is placed on a stage in the chamber area, a combination of pumps evacuates both the column and chamber [122]. The scan coils,

which are situated above the objective lens, control the position of electron beam and allow the beam to be scanned over the sample surface [122]. As the electrons interact with the sample, a number of signals (e.g. secondary electrons, characteristic X-rays and backscattered electrons) are produced and detected by appropriate detectors [124]. SEM images are formed depending on these signals, which are collected by one or more detectors, then displayed on the computer screen [123]. The electron spot size and interaction volume of sample with the electron beam are the key factors to obtain the maximum resolution by SEM technique [123].

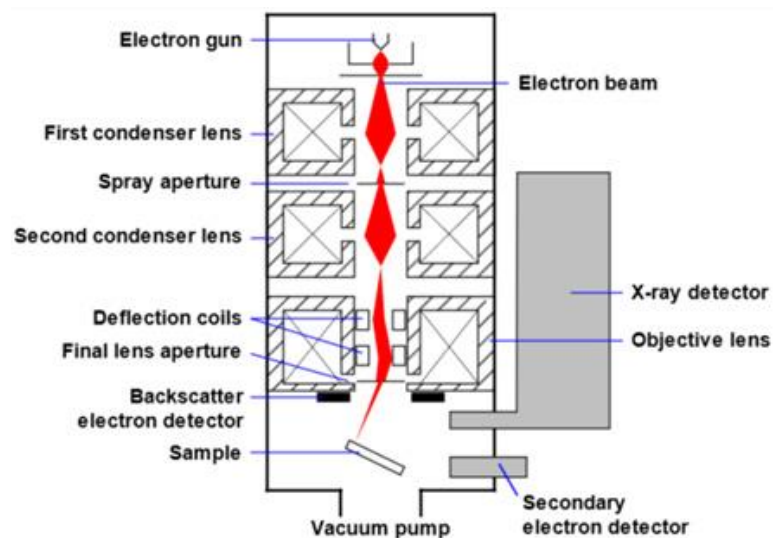


Figure 22. Components and principle of operation of an SEM [123].

Two kinds of electrons are regularly used for samples imaging. The first one is secondary electrons which are most beneficial for presenting topography and morphology of samples [125]. The other one is backscattered electrons, they are used to demonstrate the composition contrasts on samples which possess multiphase, for

instance, rapid phase discrimination [125]. The difference in SEM images produced by these two kinds of electrons is due to the different interaction volume (shown in Figure 23). When the electrons are excited to their high energy state, adequate energy can be obtained for electrons to escape the sample surface, then, secondary electrons are released from the surface atoms of the objected material [126]. A greater resolution combined with more surface sensitive can be obtained by the secondary electron imaging [126]. Because the escape depth of backscattered electrons is much greater than that of secondary electrons, the resolution of surface topographical characteristics can be damaged [126]. Nevertheless, the advantage of the backscattered electrons is that they are delicate to scatter the atomic mass of the nuclei, resulting in the elements with heavier mass backscattering more efficiently and appearing brighter than the lighter elements in a backscattered electron image [126].

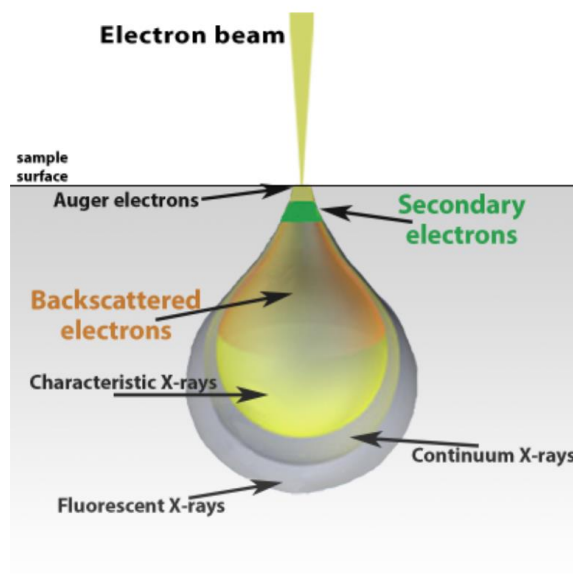


Figure 23. Schematic of electron beam interaction [127].

Additionally, energy-dispersive X-ray (EDX or EDS) spectroscopy is commonly used in conjunction with SEM to identify and quantify the elemental composition of the sample material. The incident electrons inelastically collide electrons in discrete orbitals (shells) of sample atoms to generate X-ray [128]. For a given element, the electrons in different orbitals have different energy levels. In other words, X-rays can be yielded in a specific wavelength when the excited electrons back to its lower energy states [128]. The production of characteristic X-rays of each element in a material is based on the excitation of electron beam, and then the X-rays are sent to a device for display and further data evaluation [129].

In this work, SEM was used to analyze the nanostructure and surface of cathode materials. All samples in this project was performed on a Zeiss LEO 1530 FESEM with an accelerating voltage of 10 kV under vacuum.

#### **2.1.4 High-Resolution Transmission Electron Microscopy (HRTEM)**

Transmission electron microscopy is a technique in which an electron beam is transmitting and interacting with an ultra-thin specimen. The interactions between the atoms of the specimen and the electrons are used to do features observation, such the dislocations and grain boundaries of the crystal structures [130].

As illustrated in Figure 24, the main components of TEM includes electron source, condenser lenses, objective lens, intermediate and projector lenses as well as a detector.

An electron beam is produced by a heated tungsten filament in the electron gun, then the condenser focuses the electron beam on the specimen. The magnetic lenses are used to focus the beam since electrons cannot pass through a glass lens [131]. In order to obtain a clear image, a high vacuum condition for the column, which containing the specimen and lenses, must be achieved since electrons can be deflected by colliding with air molecules [131]. The passing electron is scattered by the specimen, then focused by magnetic lenses, consequently, an enlarged, visible image of the specimen can be formed on a fluorescent screen [131]. Interestingly, the lighter areas of the image denote the areas of the sample that more electrons were passed through, while the darker areas indicate fewer electrons are transmitted through the specimen [131].

HRTEM of polymer coated samples was performed on a Zeiss Libra 200MC TEM using a 200 kV acceleration voltage. Cathode material were directly drop-casted onto the copper grid in ethanol solvent. The elemental mapping was performed using the electron energy loss spectroscopy (EELS) method on the scanning mode of the TEM instrument (STEM).

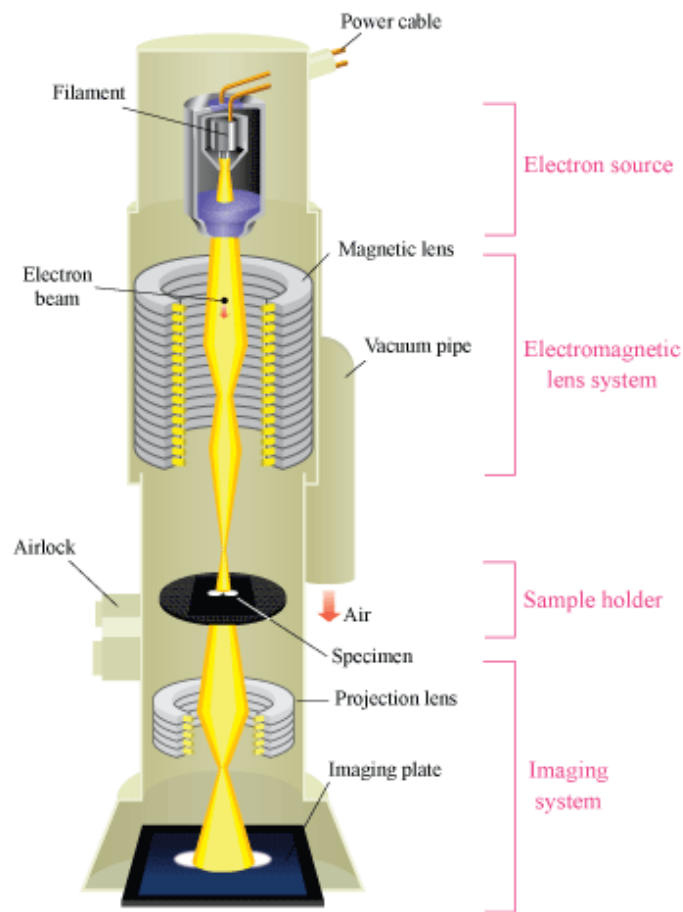


Figure 24. Components and principle of operation of an TEM [132].

### 2.1.5 X-Ray Photoelectron Spectroscopy (XPS)

X-ray photoelectron spectroscopy (XPS) is a quantitative technique for analyzing the elemental composition of the material surface, the binding states of the elements also can be determined by this technique. The main components of XPS instrument are displayed in Figure 25 including X-ray source, ultrahigh vacuum chamber, electron collection lens, electron energy analyzer and electron detector.

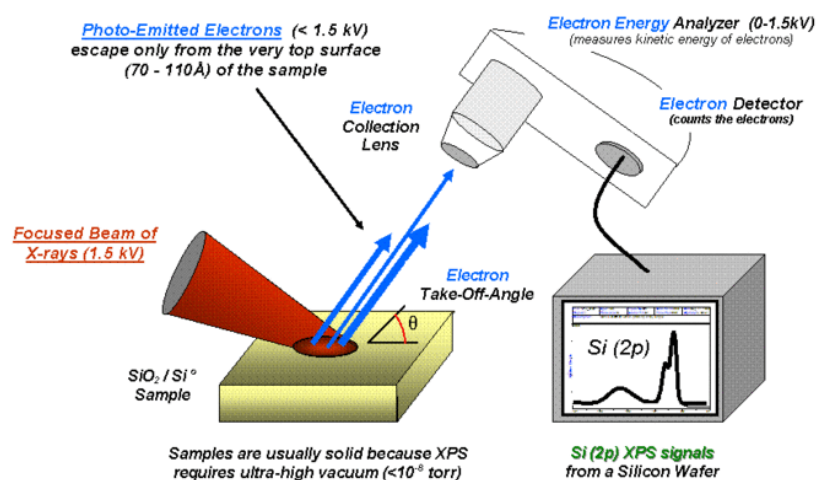


Figure 25. Schematic of XPS instrument [134].

The kinetic energy spectrum is determined by the excited photoelectrons in specific bound states from the specimen surface as the X-ray with sufficient energy ( $h\nu$ ) irradiating the object surface in ultrahigh vacuum (normally lower than  $10^{-7}$  Pa) [133]. The principle of the photoelectron emission is illustrated in Figure 26. The equation of  $h\nu$  by a kinetic energy of photoelectron,  $E_K$ , is expressed as below:

$$h\nu = E_K + E_B + \phi \quad (5)$$

where  $h$  is Plank constant,  $E_B$  is a binding energy of electron to nucleus relative to the Fermi level and  $\phi$  is the work function of the specimen. The value of chemical shift and  $E_B$  are utilized for identifying an element and analyzing the chemical bonding state of the specimen.

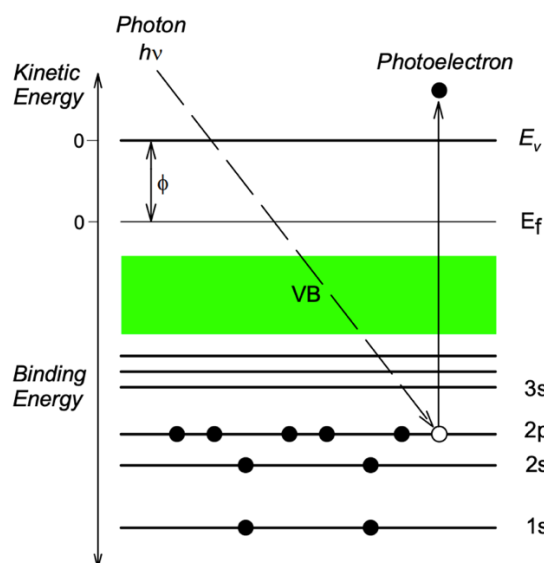


Figure 26. Principle of the photoelectron emission [135].

In a typical XPS spectrum, some of the photo-ejected electrons inelastically scatter through the sample en route to the surface, while other electrons emit immediately and few energies would be lost in escaping the surface and into the surrounded vacuum environment [134]. These photo-ejected electrons are collected once they are in the vacuum, and their kinetic energies can be measured by an electron analyzer [134]. Then, an energy spectrum of intensity vs. binding energy can be obtained by this electron energy analyzer, and each specific element has a corresponded prominent energy peak in the spectrum [134].

Apart from identifying elements of the analyzed material, the intensity of the peaks also indicates the amount of each element in the sample [136]. In other words, the number of atoms for each element is proportional to the integrated peak area, and

the chemical composition of the specimen can be obtained via calculating the contribution of each peak area respectively [136].

In this work, XPS spectra was performed by a Thermo-VG Scientific ESCALab 250 microprobe. The spectra was obtained via using a 200.0  $\mu\text{m}$  beam size at 1486.6 eV and 49.3 W. Reported binding energies were normalized against the C1s peak at 284.8 eV. During the measurement, the chamber pressure was maintained at 2.0 nPa, and wide survey (0-1200 eV) was conducted for each sample to determine the surface elemental composition of the samples.

#### **2.1.6 Thermogravimetric Analysis (TGA)**

The technique thermogravimetric analysis (TGA) is used to monitor the mass of a substance as a function of time or temperature, the sample is subjected under a defined temperature program with a controlled atmosphere. As displayed in Figure 27, a TGA consists of a sample pan that is supported by a precision balance, an auto sampler which serves to load the samples onto a micro-balance, and a thermocouple sits left below the sample [129]. The pan which loads a sample is placed in a furnace, then it is cooled or heated during the experiment, and the changes of the sample weight are monitored simultaneously [129]. The sample environment is controlled by a sample purge gas, moreover, this gas may be reactive or inert that flows over the sample and exits through an exhaust [129].

In this work, TGA was carried out in air with a temperature range of 30°C to 650°C at a ramp rate of 10°C·min<sup>-1</sup>.

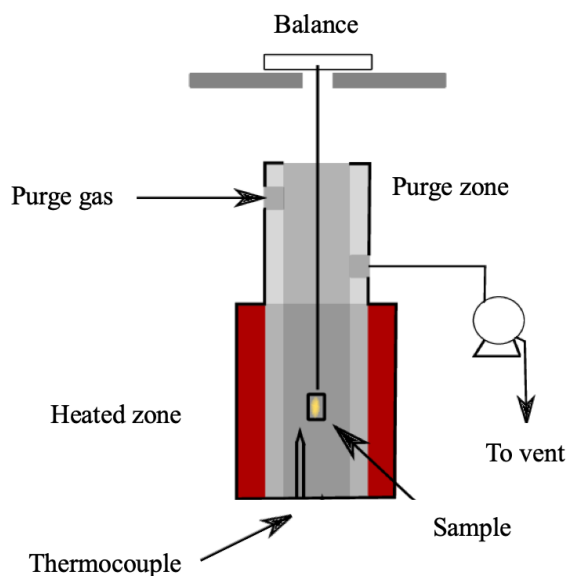


Figure 27. Schematic of TGA instrument [137].

### 2.1.7 Inductively Coupled Plasma Mass Spectrometry (ICP-MS)

Inductively coupled plasma mass spectrometry (ICP-MS) is an elemental analysis technology capable of detecting the metal elements at milligram to nanogram levels per liter. Atomic elements are led through a plasma source where they become ionized. Then, these ions are sorted on account of their mass.

As displayed in Figure 28, an ion source (ICP), a sampling interface, ion lens, a mass spectrophotometer and a detector are involved in ICP-MS. ICP, as the ion source, is an ideal ionization source which can ionize over 90% of the elements for mass

spectrometry [138]. Samples as the form of aerosol droplets are introduced into an argon plasma. The aerosol is dried by the plasma, and the molecules are dissociated, then the electrons from the components are removed, and consequently forms singly-charged ions [138]. Ions produced in the ICP leading the interface of a sample to a mass analysis unit. Two metallic cones are involved in the sampling interface unit, one is the sampling cone and the other one is skimmer cone, and a rotary gear pump ventilates between the two cones into several hundreds of Pa condition [138]. The sampling cone and the skimmer cone pull through the ions path, and use the ion lens to converge it into the mass spectrophotometer [138]. The ion lens and the mass spectrophotometer unit based on the turbo molecular pump are respectively ventilated to  $10^{-3}$  and  $10^{-4}$  Pa [138]. Additionally, the ions are classified by mass with the mass spectrophotometer and subsequently detected by the ion detector.

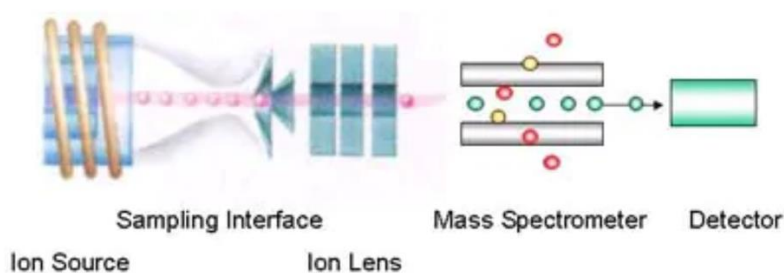


Figure 28. Schematic of ICP-MS instrument [138].

In this work, the amounts of elemental composition (V, Na and Zn) of the cathode material were detected by ICP-MS instrument. The powder sample was dissolved in

dilute nitric acid and the concentration of each element should over their detection limit of ICP-MS. The detection limits for each element are shown in Table 2.

<b>Line</b>	<b>DL</b>	<b>Units</b>
Mn 257.610 r	0.002	mg/L
Fe 238.204 r	0.004	mg/L
Ca 422.673 r	0.015	mg/L
Cu 324.754 r	0.005	mg/L
Zn 202.548 r	0.016	mg/L
Na 588.995 r	0.108	mg/L
Mg 285.213 r	0.003	mg/L
K 766.491 r	0.078	mg/L
Al 396.152 r	0.012	mg/L
Li 670.784 r	0.003	mg/L
Si 251.611 r	0.024	mg/L
V 309.311 r	0.004	mg/L

Table 2. Element detection limit of ICP-MS.

## 2.2 Electrochemical Characterization Techniques

### 2.2.1 Electrochemical Impedance Spectroscopy (EIS)

Electrochemical impedance spectroscopy (EIS) is an electrolytic method to measure the impedance and study the electrode kinetics of a system depends on the low amplitude alternating current (AC) potentials over a range of frequencies. A three electrode setup (T-cell Swagelok, as shown in Appendix 1) involves a working, a counter and a reference electrodes is conducted under a known voltage. The voltage is

passed from the working electrode through an electrolytic solution and into the counter electrode [139]. The EIS produces quantitative measurements which provide the evaluation of chemical mechanisms in small scale at the electrode interface in a electrolytic solution [139]. Hence, studying the research fields of batteries, coating evaluation, electrodeposition and corrosion, EIS is considered as a powerful technique to determine the electrical and dielectric properties of components in a wide range.

EIS studies can be utilized in both three electrode mode and coin cell. A metallic sample container (e.g. Swagelok) filled with a prepared electrolytic solution would provide additional pathways for electrons transportation during the experimentation [139]. As a result, the electrons prefer moving to the metal rather than the reference electrodes because the reduction of EIS response current. With this regard, insulating materials (e.g. glass or plastic) are employed to be the composition of a sample container, which will effectively decrease the impacts of electrons movement during testing [139]. In a three electrode mode, all (working, reference and counter) electrodes are submerged into the electrolytic solution, and using leads to connect these three electrodes to the frequency response analyzer, as shown in Figure 29. Then, the EIS system is ready for testing when all leads and parts are connected.

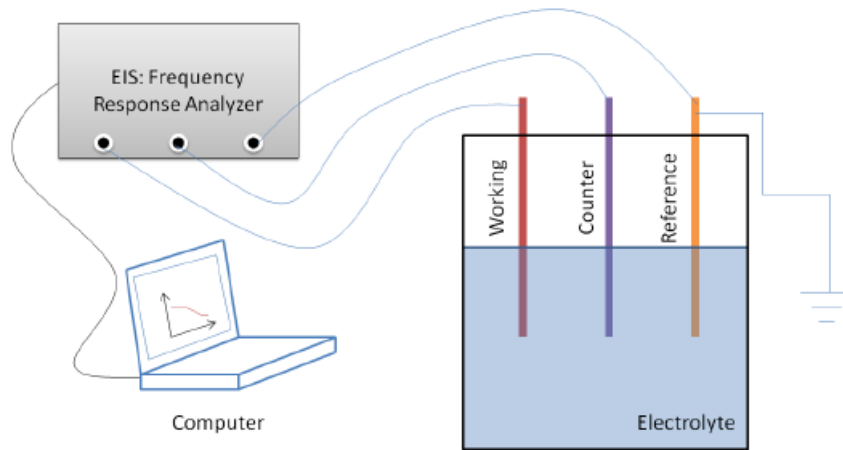


Figure 29. Experimental EIS system set up using three electrode mode [139].

After testing, electrochemical impedance data was expressed via a Nyquist plot (as an example displayed in Figure 30), which presents a plotting of the real impedance (along x-axis) vs. the negative imaginary part (along y-axis). Two principal equations describe the real and imaginary impedance components of EIS are shown in Equations 6 and 7, respectively:

$$Z' = R_s + \frac{R_{ct}}{1 + \omega^2 R_{ct}^2 C_{dl}^2} \quad (6)$$

$$Z'' = \frac{R_{ct}^2 C_{dl} \omega}{1 + \omega^2 R_{ct}^2 C_{dl}^2} \quad (7)$$

where  $Z'$  and  $Z''$  are the real and imaginary parts of impedance,  $R_s$  represents the equivalent serial resistance,  $R_{ct}$  is the charge-transfer resistance,  $C_{dl}$  is the double-layered capacitance and  $\omega$  is the applied frequency.

The characterization of the frequency dependence of impedance responses are presented by the electrical components in a Nyquist plot [139]. The electrical components are established by equivalent circuits (inserted in Figure 30). Near the region of plot origin, where corresponds to the high frequency intercept, the real impedance value gives the combination of electrode and electrolyte resistance in this battery, as referred to equivalent serial resistance ( $R_s$ ) [140]. The intercept at intermediate frequency of the real axis offers a summation of the  $R_{ct}$  and  $R_s$ , herein, we can treat the diameter of this semicircle as the value of charge-transfer resistance ( $R_{ct}$ ).  $R_{ct}$  stands by the moving resistance of electrons between the cathode material and electrolyte [141]. In addition, the tail in the low frequency region of Nyquist plot presents Warburg straight line, the ion diffusion rate in battery system can be determined by its slope value [140].

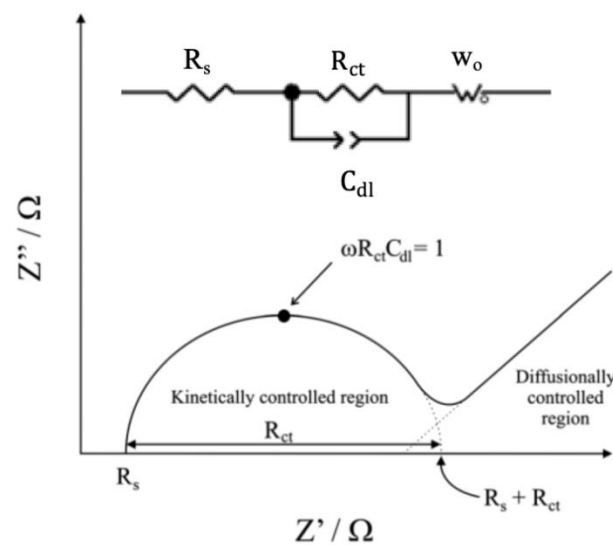


Figure 30. Relationship between Nyquist plot components [141].

In this project, EIS measurements were conducted on a Bio-Logic VMP3 electrochemical workstation. A coin cell contains the synthesized material as the working electrode, zinc disk as the counter electrode and an absorbed glass mat (AGM) as separator soaked with the electrolytic solution was constructed for the testing. Firstly, a 10 mV DC square wave was applied, then followed by scanning of AC frequencies from 1 MHz to 10 mHz.

### **2.2.2 Cyclic Voltammetry**

Cyclic voltammetry (CV) is a potentiodynamic electrochemical technique to measure the reduction and oxidation potentials of the chemical species. A cyclic voltammogram trace is obtained by recording the current, which flows between the working electrode and counter electrode, as a function of the applied voltage [142]. The working electrode potential is ramped linearly with time to draw a waveform in a triangle shape [142]. The potential scan with time and the resulted CV plots are shown in Figure 31. Under cathodic scanning, the peak current increases with the potential approaching to the reduction potentials of the analyzed chemical, then it falls off because the concentration of the analyte is consumed close to the electrode surface [142]. Subsequently, as the applied potential is reversed, the product which formed in the first reduction reaction will be re-oxidized as long as it will reach a potential, and a

current of reverse polarity from the forward scan is produced [142]. This oxidation peak will usually have a similar shape to the reduction peak.

The nonsymmetric and large differences of reduction and oxidation peaks indicate the nonreversible reaction. Moreover, the peak potential, peak current and the characteristic shape of cyclic voltammograms are the key parameters to characterize and study the mechanism of redox reactions at electrodes.

In this work, CV was utilized to measure the oxidation and reduction potentials of metal ions in both coin cell and three electrode battery systems. A Bio-Logic VMP3 electrochemical workstation was used to obtain the CV measurements with different scan rates under a voltage range of 0.2-1.6 V. Ag / AgCl and polished zinc foil were respectively employed as a reference and a counter electrode in three electrode system, aqueous electrolytes containing 2M ZnSO<sub>4</sub> with and without 2M Na<sub>2</sub>SO<sub>4</sub> were adjusted to pH=3.7± 0.2.

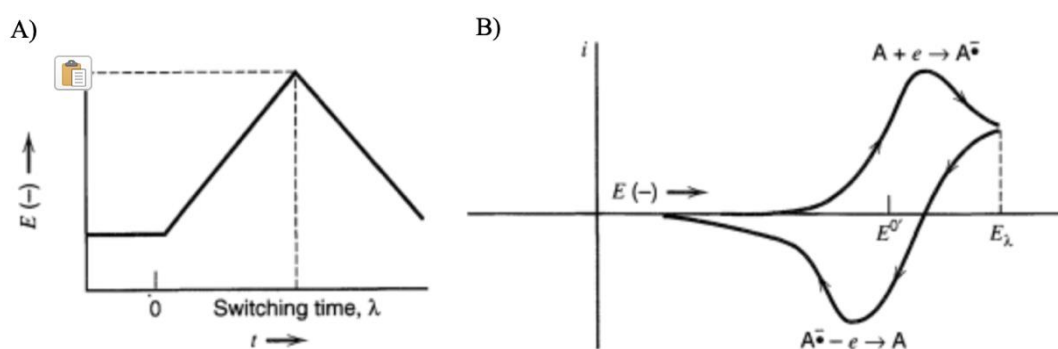


Figure 31. A) Potential scan with time and B) the resulted CV plot [143].

### 2.2.3 Battery Testing

In this work, galvanostatic charge-discharge cycling of batteries were tested using the constant current (CC) protocol by using a Neware battery tester at two current densities of 1 C and 5 C, where  $200 \text{ mA} \cdot \text{g}^{-1}$  corresponds to 1 C rate, for small coin cells ( $\sim 1.13 \text{ cm}^2$  in cell) and large batteries ( $\sim 9 \text{ cm}^2$  in cell, as shown in Appendix 2) under a voltage range of 0.2–1.6 V vs.  $\text{Zn}^{2+} / \text{Zn}$ . The cycling retention after x cycles was calculated based on the following equation:

$$\text{cycling retention} = \frac{\text{specific discharge capacity of } x \text{ cycle}}{\text{specific discharge capacity of 1st cycle}} \times 100\% \quad (8)$$

To observe the performance of discharge capacity at variety of current densities, rate capability test was conducted at gradual current rates (C-rate) of 1, 2.5, 5, 10 C, and then returned from high C-rate to 1 C under the voltage range of 0.2-1.6 V.

## **Chapter 3: Conductive Polymer Modified-Vanadium Oxide as the Cathode Materials in Rechargeable Aqueous Zinc-ion Batteries**

### **3.1 Fabrication of Conductive Polymer Coated Ball-milled Vanadium Oxide**

Ball-milling method was utilized to reduce the particle size of commercial  $V_2O_5$  via grinding. Firstly, a given amount of commercial  $V_2O_5$  powder (Sigma-Aldrich,  $\geq$  98% purity) was added into the ball-milled container, rotational speed 800 rpm is set with 8 hours grinding. During this grinding process, high pressure can be generated by collision of tiny solid balls in a sealed container, which makes original  $V_2O_5$  into a smaller particle size. Additionally, the activation process of the  $V_2O_5$  battery could be minimized significantly.

Polypyrrole (PPy) and polyaniline (PANI) were synthesized on the surface of  $V_2O_5$  via in situ polymerization. This method also refers to chemical oxidative polymerization, that a given amount of monomer reacts with oxidizing agent under a specific condition [82][97][103].

### **3.1.1 Synthesizing Polypyrrole (PPy) on the Surface of Ball-milled Vanadium Oxide**

In brief, 0.5 g ball-milled  $V_2O_5$  are dispersed into 200 mL deionized (DI) water with stirring for 15 min. Then, placing the suspension to 20 min sonication. After that, 1.82 g iron chloride ( $FeCl_3$ , Sigma-Aldrich,  $\geq 97\%$  purity) as oxidant and 0.8 g p-toluenesulphonic acid sodium ( $C_7H_7O_3SNa$ , Sigma-Aldrich,  $\geq 95\%$  purity) as surfactant are added into the solution and keep stirring for 30 min under ice bath ( $0-5^\circ C$ ). 0.05 g pyrrole monomer are added into the mixture, followed by an oxidative polymerization at low temperature for 5 hours [103].

Finally, the solid products are separated from aqueous solution by centrifugation, washed by DI water and ethanol for several times, then dried in vacuum oven at  $60^\circ C$  overnight. The final product ball-milled  $V_2O_5$ -PPy is showed in dark green color (as in Figure 32).

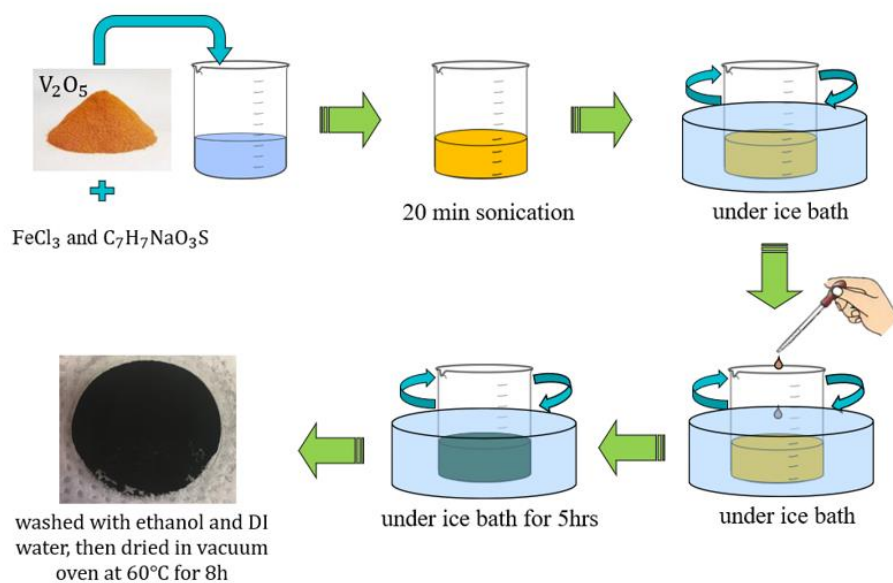


Figure 32. Experimental procedure of synthesizing ball-milled  $V_2O_5$ -PPy.

### 3.1.2 Synthesizing Polyaniline (PANI) on the Surface of Ball-milled Vanadium Oxide

With regard to PANI polymerization, 0.05 g aniline monomer in 30 mL 0.1M HCl solution are dispersed into ball-milled  $V_2O_5$  and DI water suspension, then 0.63 g ammonium persulphate (APS, Sigma-Aldrich,  $\geq 98\%$  purity) is added into the reaction system under vigorous magnetic stirring at temperature 0-5°C for 24 hours [82]. After washed with DI water and ethanol, the green powder product is obtained after drying overnight.

The conductive polymer which is coated on particle surface acts as a barrier between ball-milled  $V_2O_5$  and aqueous electrolyte, avoiding the host material (ball-

milled  $V_2O_5$ ) to contacting aqueous electrolyte directly and dissolving in electrolyte during charge and discharge process.

### **3.2 Cathode Fabrication and Battery Assembling**

The working electrode (or the cathode of the battery) consists 70 wt% active material (ball-milled  $V_2O_5$  coated by conductive polymer), 20 wt% graphene nanoparticle (GNP), and 10 wt% polyvinylidene fluoride (PVDF) in N-methyl-2-pyrrolidone (NMP) solution. The slurry is uniformly pasted onto the polyethylene (PE) film (All-Spec 854-36150) and dried at 60°C for 8 hours.

Both CR2032 coin-type and large batteries were employed for electrochemical tests. For coin cell, the cathode is punched into small disks with a diameter of 12 mm, and the mass loading of active material is around 4.5 mg·cm<sup>-2</sup>. As shown in Appendix 2 C), RAZB is assembled by the cathode containing vanadium-based material, double-layered absorbed glass mat (AGM, NSG Corporation, diameter: 12 mm, thickness: 0.5 mm) as the separator, and polished metal zinc (Rotometals, diameter: 12 mm, thickness: 0.2 mm) as the anode. As refer to the large battery shown in Appendix 2 D), the cathode (~ 9 cm<sup>2</sup> in cell), AGM separator and anode are cut in square shapes. The electrolyte is prepared by 2M zinc sulfate ( $ZnSO_4$ , Sigma-Aldrich,  $\geq$  98% purity) in DI water with pH value of  $3.7 \pm 0.2$ .

### 3.3 Material Characterizations

#### 3.3.1 Fourier Transformed Infra-Red Spectroscopy (FTIR)

Firstly, the technique FTIR was utilized to detect the chemical compounds of PPy and PANI on ball-milled  $V_2O_5$ . In Figure 33 A), the characteristic peak locates at  $1012\text{ cm}^{-1}$  is assigned to V=O stretching of raw material ball-milled  $V_2O_5$ , and  $840$  and  $531\text{ cm}^{-1}$  bands represent the symmetric and asymmetric V-O-V vibrational modes, respectively [144]. A set of “signature” peaks are illustrated in the spectrum of ball-milled  $V_2O_5$ -PPy, which are located at three absorption bands of  $1557$ ,  $1329$  and  $1200\text{ cm}^{-1}$ . The characteristic peak at  $1557\text{ cm}^{-1}$  presents the pyrrole ring, the absorption bands at  $1329\text{ cm}^{-1}$  and  $1200\text{ cm}^{-1}$  attribute to the in-plane N-H deformation of the pyrrole ring and C-H stretching vibration [98][100][103]. In the spectrum of ball-milled  $V_2O_5$ -PANI (Figure. 1 B), the bands locate at  $1508$  and  $1316\text{ cm}^{-1}$  are assigned to benzenoid (B) ring and C-H stretching, and the B-NH-B or aromatic C-H in plane bending appears at  $1168\text{ cm}^{-1}$  [82][145]. It is worth noting that the two “signature” peaks of ball-milled  $V_2O_5$  are shifted closer to each other (from  $840$  to  $828\text{ cm}^{-1}$  and  $531$  to  $562\text{ cm}^{-1}$ , respectively) after polymer modification. This situation suggests a sensitive physical interaction is occurred between the  $V_2O_5$  surface and coated polymer. Thus, the in-situ polymerization on  $V_2O_5$  surface can be roughly considered successfully by FTIR measurements.

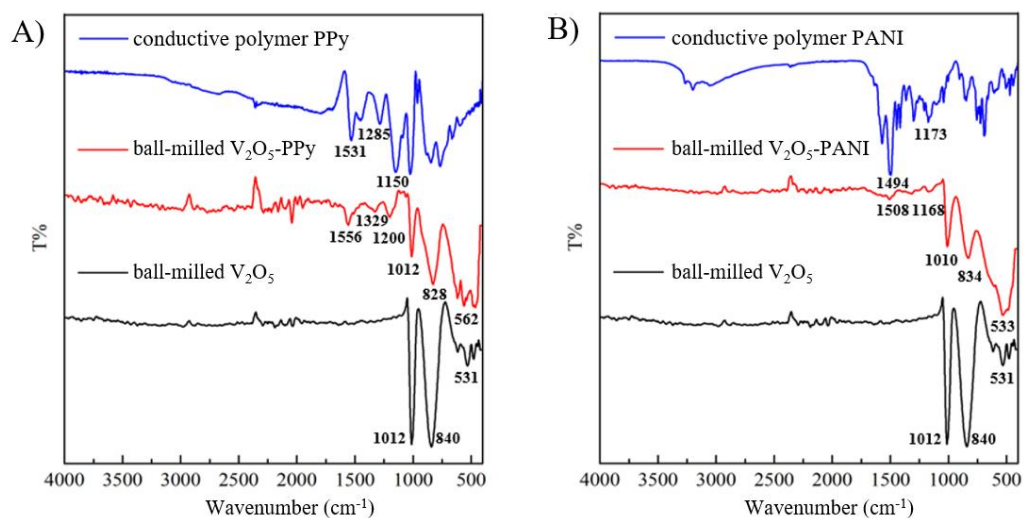


Figure 33. The FTIR patterns of A) ball-milled  $V_2O_5$ -PPy powder and B) ball-milled  $V_2O_5$ -PANI powder.

### 3.3.2 X-Ray Diffraction (XRD)

The XRD patterns of ball-milled  $V_2O_5$ , polymer-modified samples with a  $2\theta$  angle ranging from  $10^\circ$  to  $70^\circ$  are represented in Figure 35. A superb matching between the commercial  $V_2O_5$  powder (PDF# 41-1426) and ball-milled  $V_2O_5$  is demonstrated in Figure 34, its layered structure with corresponding diffraction (001) is indicated by the most intense peak located at  $2\theta = 20.347^\circ$  [146], and the typical orthorhombic structure of ball-milled  $V_2O_5$  is well-indexed with the commercial  $V_2O_5$  [48][49]. These demonstrate that the ball-milling method would not impact the structure of raw material (commercial  $V_2O_5$ ). Both ball-milled  $V_2O_5$ -PPy and ball-milled  $V_2O_5$ -PANI display similar XRD patterns to ball-milled  $V_2O_5$  in Figure 35. Because of the ultrathin and

amorphous polymer coating layers on ball-milled  $V_2O_5$ , the incident X-ray only interacts with the  $V_2O_5$  crystals. Furthermore, there are no chemical reactions occurred on the surface of  $V_2O_5$  since no obvious differences are displayed in peak intensities and locations [148]. With this regard, polymer modification will not affect the crystalline structure of raw material. Additionally, far more advanced crystallinities of the polymer-modified  $V_2O_5$  samples are exhibited in this pattern, indicating that the surface coating method employed by conductive polymers develops a stable structure, thus, the reversible  $Zn^{2+}$  intercalation and de-intercalation would be promoted during the cycling.

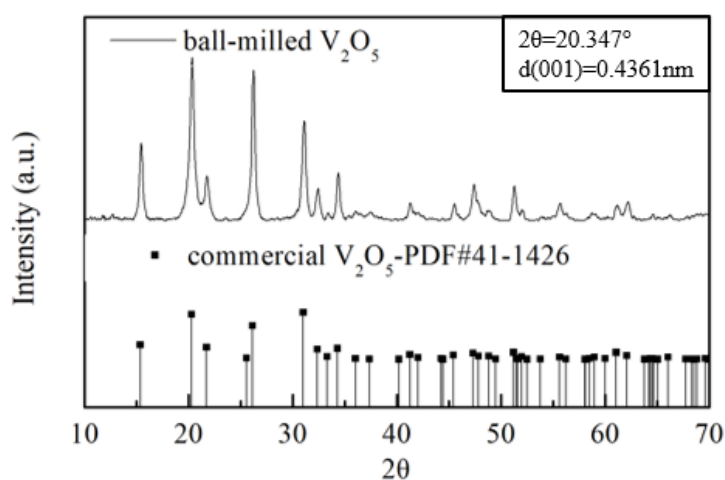


Figure 34. The XRD patterns of ball-milled  $V_2O_5$  and commercial  $V_2O_5$  (PDF# 41-1426).

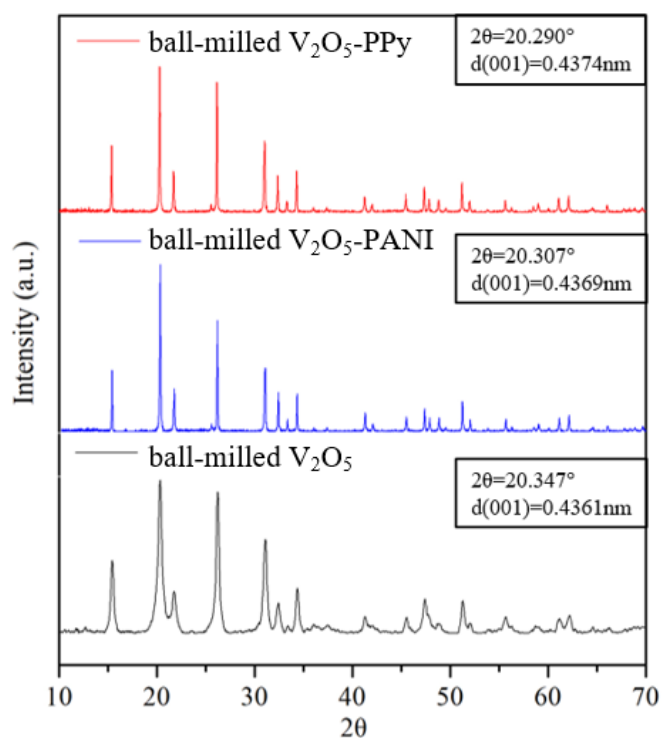


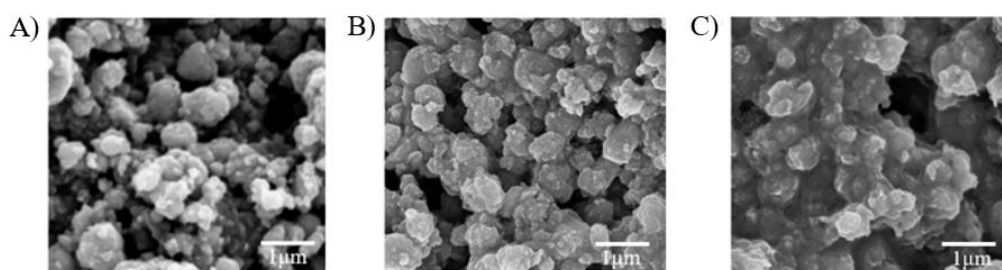
Figure 35. The XRD patterns of ball-milled  $V_2O_5$ -PPy and ball-milled  $V_2O_5$ -PANI and ball-milled  $V_2O_5$ .

### 3.3.3 Electron Microscopy

The morphology of polymer-modified  $V_2O_5$  particles were detected by the scanning electron microscopy (SEM). In Figure 36 A) to C), the observation of coating layers on the bare  $V_2O_5$  particle surface is evident, which contributing smoother coating walls on  $V_2O_5$  particles surface. Moreover, the modification on  $V_2O_5$  can be supported by signals of elements from energy-dispersive X-ray (EDX or EDS) pattern. As an example for ball-milled  $V_2O_5$ -PPy, elements N and Cl can be observed in Figure 37, where N only exists in heterocyclic aromatic ring and Cl comes from  $FeCl_3$  (oxidizing

agent). In addition, the compositions of each coating layer have been verified by FTIR results as mentioned in the above section. Herein, the conductive polymers are believed to coat on the surface of ball-milled  $V_2O_5$  by in-situ polymerization method.

High-resolution transmission electron microscopy (HRTEM) was conducted on investigating the material structure and thickness of conductive polymer coating. The lattice fringes of  $V_2O_5$  particle is presented in Figure 36 D), this image demonstrates a good agreement in its layered structure. In Figure 36 E) and F), the darker regions correspond to the  $V_2O_5$ , and the edge areas in bright color reveal the polymer-modified layers. The thickness of the PPy and PANI coating layers is measured around 6.7 nm and 13.2 nm, respectively. Because of developing a compact coating layer on the  $V_2O_5$  surface, the direct contact between active material and electrolyte can be minimized, and the dissolution of cathode material in aqueous electrolytes would be decreased eventually.



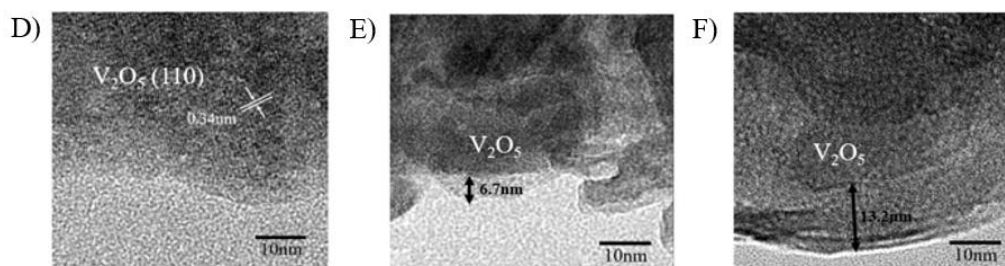


Figure 36. SEM images of A) ball-milled  $V_2O_5$ , B) ball-milled  $V_2O_5$ -PPy and C) ball-milled  $V_2O_5$ -PANI with scale bar of 1  $\mu\text{m}$ . TEM images of D) ball-milled  $V_2O_5$ , the coating thickness of E) ball-milled  $V_2O_5$ -PPy and F) ball-milled  $V_2O_5$ -PANI with scale bar of 10 nm.

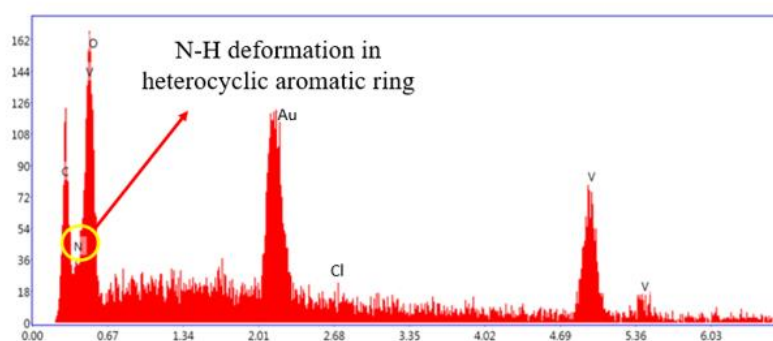
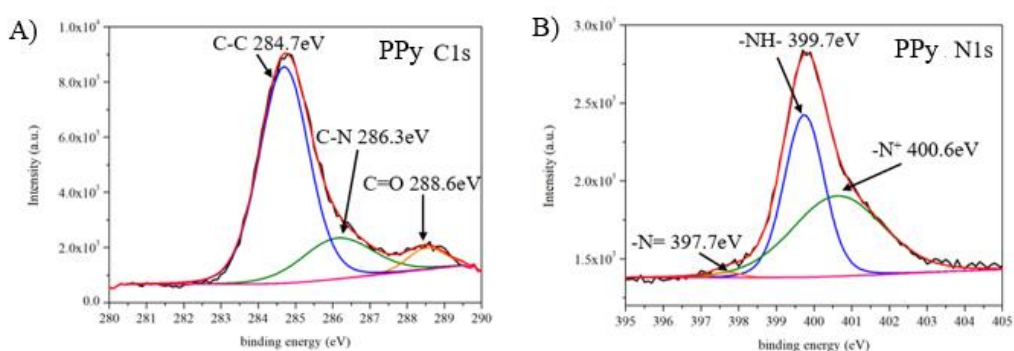


Figure 37. EDX image of ball-milled  $V_2O_5$ -PPy sample.

### 3.3.5 X-ray Photoelectron Spectroscopy (XPS)

X-ray photoelectron spectroscopy (XPS) is a quantitative technique for analyzing the elemental composition of the material surface, the binding states of the elements also can be determined by this technique. The existence of the coating layer of PPy can be confirmed by the characteristic peaks of C 1s and N 1s in Figure 38 A) and B). Three

different C species in the heterocyclic aromatic ring of pyrrole correspond the characteristic peaks at the binding energy (BE) of 284.7 eV, 286.3 eV and 288.6 eV in C 1s spectra. The neutral amine nitrogen (-NH-) is indicated in N 1s spectra of PPy as the major characteristic peak locates at 399.7 eV, the peak with higher BE of 400.6 eV demonstrates the nitrogen with positive charges ( $-N^+$ ), and the imine nitrogen ( $-N=$ ) is revealed at the lower BE of 397.7 eV [148]. Because of the anion doping (Cl<sup>-</sup>) on the conductive polymer PPy, the  $-N^+$  is presented in spectra which corresponds well to the observation of element Cl in EDX results (in Figure 37). Similarly, the coating layer composition of PANI sample also can be verified by the signature peaks in C 1s and N 1s spectra (in Figure 38 C) and D)). Therefore, the finding results of polymer compositions by using the XPS technique are consistent with the results from the FTIR method.



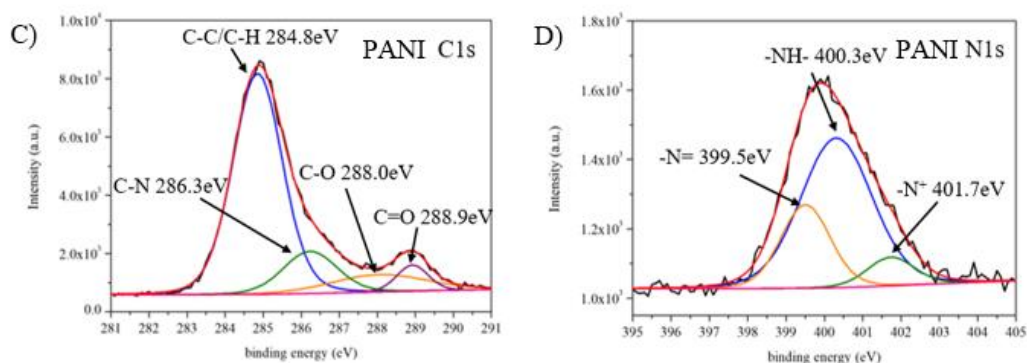


Figure 38. XPS spectra of ball-milled V<sub>2</sub>O<sub>5</sub>-PPy A) C 1s, B) N 1s, and ball-milled V<sub>2</sub>O<sub>5</sub>-PANI C) C 1s, D) N 1s.

### 3.3.4 Thermogravimetric Analysis (TGA)

Thermogravimetric analysis (TGA) was utilized to quantify the polymer amount in the modified samples. This technique was carried out in air with a temperature range of 30°C to 650°C at a ramp rate of 10°C·min<sup>-1</sup>. The plots of weight loss of polymer-coated V<sub>2</sub>O<sub>5</sub> powders vs. temperature are displayed in Figure 39. The ball-milled V<sub>2</sub>O<sub>5</sub> sample in black line maintains the weight percentage stably over the temperature range. With the comparison of ball-milled V<sub>2</sub>O<sub>5</sub> sample, the polymer-coated samples exhibit slight weight losses below 250°C, this situation corresponds to the removal of free and crystalline water as well as gases in a sample. Then, a followed dramatic weight drop occurs within 250°C-400°C that indicates the combustion of polymer component. By using this method, it was estimated that the amounts of PPy layer and PANI layer on the ball-milled V<sub>2</sub>O<sub>5</sub> particles was around 7.8% and 15.3% by weight, respectively.

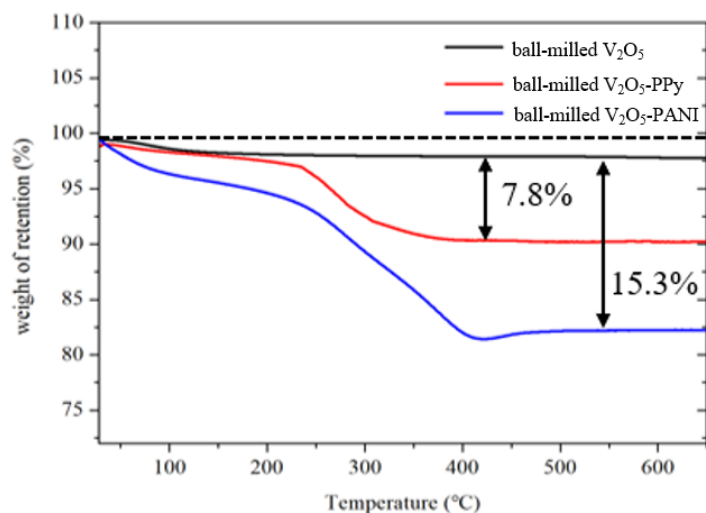


Figure 39. TGA measurements of ball-milled V<sub>2</sub>O<sub>5</sub>, ball-milled V<sub>2</sub>O<sub>5</sub>-PPy and ball-milled V<sub>2</sub>O<sub>5</sub>-PANI in a temperature range of 30°C to 650°C at a ramp rate of 10°C·min<sup>-1</sup>.

### 3.4 Electrochemical Performance

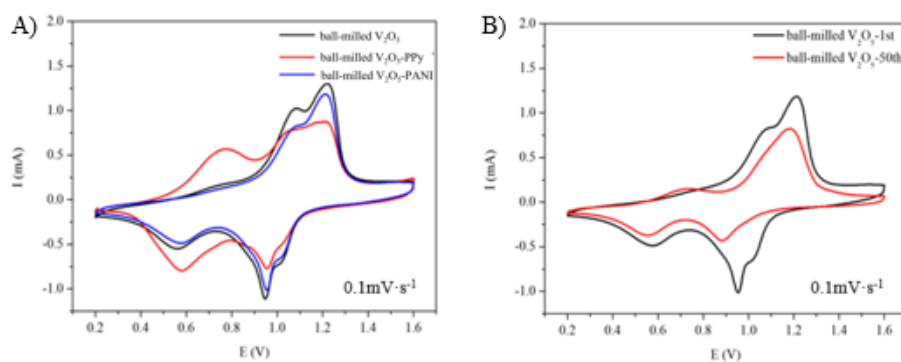
To fabricate a thermally stable cathode material for RZAB, especially under elevated temperatures (40, 60 and 80 °C), cyclic tests, rate capability, cyclic voltammetry and impedance measurements were used to value the electrochemical performance of polymer-coated cathodes. Consequently, we aim to develop a superior cyclic stability of RAZBs by utilizing this surface coating method to improve the structural stability of V<sub>2</sub>O<sub>5</sub> in aqueous environment during the cycling process.

### 3.4.1 Cyclic Voltammetry (CV)

Cyclic voltammetry (CV) test was firstly used to investigate the electrochemical performance of polymer-modified samples under ambient and elevated temperatures. In small coin cell batteries, the observation of three pairs of redox peaks among these samples in Figure 40 A) is obtained by CV technology in a voltage range of 0.2 -1.6 V vs.  $Zn^{2+} / Zn$  at a scanning rate of  $0.1 \text{ mV}\cdot\text{s}^{-1}$ . Three steps of zinc ion de- / intercalation during the charge / discharge process are represented by these pairs of peaks under this voltage range [146][147]. It is worth noting that the response currents of one-pair redox peak of ball-milled  $V_2O_5$ -PPy locates at 0.75 / 0.58 V are enhanced and exceeds other pair of redox peaks (locate at 1.22 / 0.95 V). This is due to the additional redox reactions of polymer composition (PPy) occurs within 0.6-1.2 V (oxidation) and 0.4-0.8 V (reduction) voltage range as shown in Figure 40 D). Herein, the reactions of conductive polymer PPy may devote to slightly increase the discharge capacity for RAZBs. On the contrary, owing to no redox reactions for PANI compound within the same voltage range, the ball-milled  $V_2O_5$ -PANI sample shows very similar CV results to the control one.

However, the 2nd and 3rd oxidation peaks of ball-milled  $V_2O_5$  locate at 1.08 and 1.22 V are overlapped at 1.18 V, and their corresponded reduction peaks at 1.02 and 0.95 V are consolidated into one top determines at 0.88 V after 50 cycles as presented in Figure 40 B). This similar event also occurred to sample ball-milled  $V_2O_5$ -PANI in Figure 40 C). The galvanostatic charge and discharge curves of ball-milled  $V_2O_5$  and

ball-milled  $V_2O_5$ -PANI samples at their 1st and 50th cycles are respectively shown in Figure 40 E) and F), this test is carried out under room temperature at a current density of 5 C. An obvious capacity fading of ball-milled  $V_2O_5$  sample is displayed when cycle number is increased, this is due to the zinc ions cannot fully extract from the  $V_2O_5$  interlayer during charge process. Thereby, a tilting platform is formed as a result of charge / discharge plateaus connection, which corresponds to the reduction of one more pair of redox peaks in its CV plots. Moreover, an enormous capacity gap between 1st and 50th cycling tests is existed in the galvanostatic discharge curve in Figure 40 E), and a slight capacity fading of ball-milled  $V_2O_5$ -PANI sample is indicated in Figure 40 F). Nevertheless, its reduction peak at 0.53 V in cathodic sweeping and an oxidation peak at 0.7 V in anodic scans are both heightened in the CV plot of ball-milled  $V_2O_5$ -PANI sample (shown in Figure 40 C). This condition is thanks to the conductive polymer layers minimize the exposure and dissolution of host material  $V_2O_5$  in the acidic electrolytic solution. As a result, the side reactions between  $V_2O_5$  and electrolyte can be reduced.



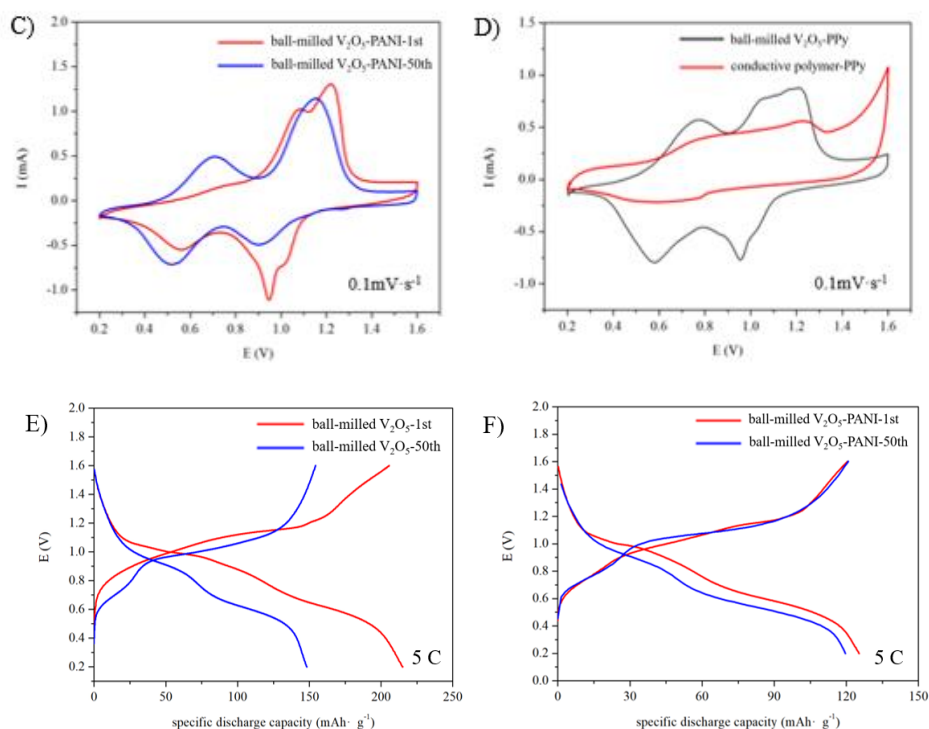
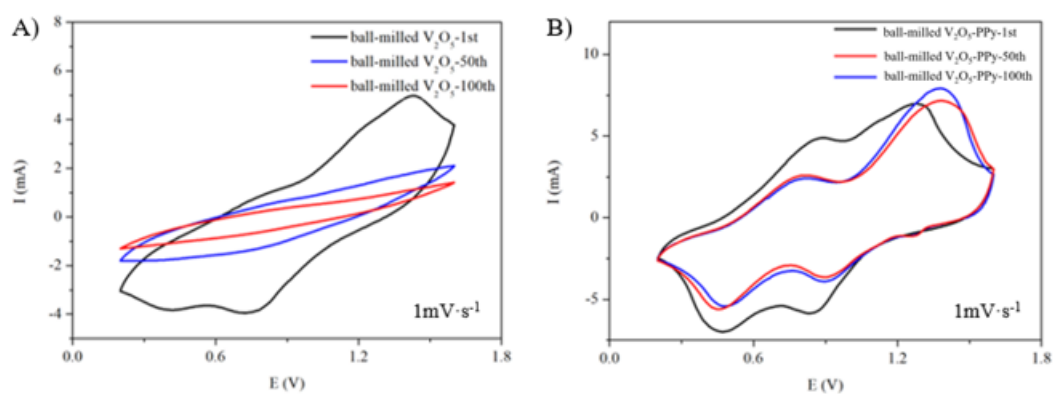


Figure 40. The CV plots of A) ball-milled  $V_2O_5$ , ball-milled  $V_2O_5$ -PPy and ball-milled  $V_2O_5$ -PANI at their 1st cycling, B) ball-milled  $V_2O_5$  cathode and C) ball-milled  $V_2O_5$ -PANI at their 1st and 50th cycling, D) ball-milled  $V_2O_5$ -PPy and the conductive polymer PPy cathode at 1st cycling with a scan rate of  $0.1 \text{ mV}\cdot\text{s}^{-1}$ . The galvanostatic charge / discharge curves of E) ball-milled  $V_2O_5$  cathode and F) ball-milled  $V_2O_5$ -PANI cathode at 5 C at room temperature.

CV measurements at a scanning rate of  $1 \text{ mV}\cdot\text{s}^{-1}$  at  $60^\circ\text{C}$  were obtained to investigate the electrochemical performance at elevated temperatures by employing the three electrode system, the results are shown in Figure 41. Enormous differences in the plot of control sample in Figure 41 A) are exhibited with increased cycle numbers, this is caused by the serious corrosion of  $V_2O_5$  cathode in an acidic aqueous electrolyte at a

high temperature. To confirm this, the  $V_2O_5$  electrodes were respectively immersed in 2M  $ZnSO_4$  electrolyte at room temperature and  $60^\circ C$  for 3 hours, the resulted electrolyte solutions are shown in Appendix 3. The electrolyte would be colorless and transparent at room temperature, however, after the  $V_2O_5$  electrode is immersed for 3 hours at  $60^\circ C$ , the electrolyte color turns yellow which indicates the dissolution of  $V_2O_5$  material is occurred under a high temperature condition. Thus, there are no redox peaks for capacity contribution of  $V_2O_5$  sample at  $60^\circ C$  since the bare  $V_2O_5$  has poor thermal stability. Nevertheless, in Figure 41 B and C, both polymer-modified samples exhibit at least two pairs of redox peaks even after 100 cycles which thanks to the protection of polymer coating layers and their good thermally stable properties at high temperatures.



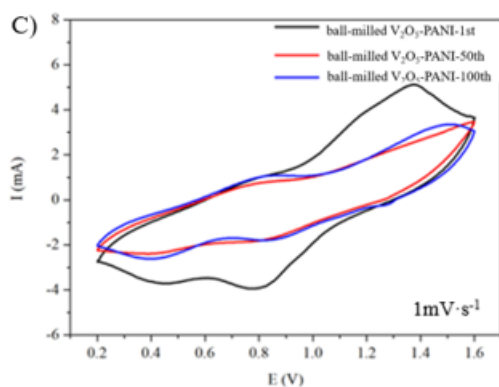


Figure 41. CV plots of A) ball-milled  $V_2O_5$ , B) ball-milled  $V_2O_5$ -PPy and C) ball-milled  $V_2O_5$ -PANI at their selected cycling (1st, 50th, 100th) with  $1 \text{ mV} \cdot \text{s}^{-1}$  scanning rate at  $60^\circ\text{C}$ .

### 3.4.2 Rate Capability

Rate capabilities of different cathode materials in RAZBs at room temperature are exhibited in Figure 42 A). The discharge capacity of bare  $V_2O_5$  drops rapidly as a current density jumps from 5 C to 10 C, however, both polymer-modified samples display similar capacity performance at increased current densities. This is based on the crucial protection of the compact coating layer. Regarding the rate capability of these three samples at  $60^\circ\text{C}$  (in Figure 42 B), as the dissolution of bare  $V_2O_5$  is extremely serious at small current densities, the measured values of its specific discharge capacity are around  $0 \text{ mAh} \cdot \text{g}^{-1}$  when reaching higher current densities. Even though, the polymer-coated samples exhibit superb rate performance at  $60^\circ\text{C}$ , and higher discharge capacities at different current densities are delivered by the ball-milled  $V_2O_5$ -PPy

cathode in RAZBs. Furthermore, at temperatures ranging from 40 to 80°C, both polymer-coated samples reveal favorable performance at high current rates (Figure 42 C and D) due to the excellent thermal stability of their coating components.

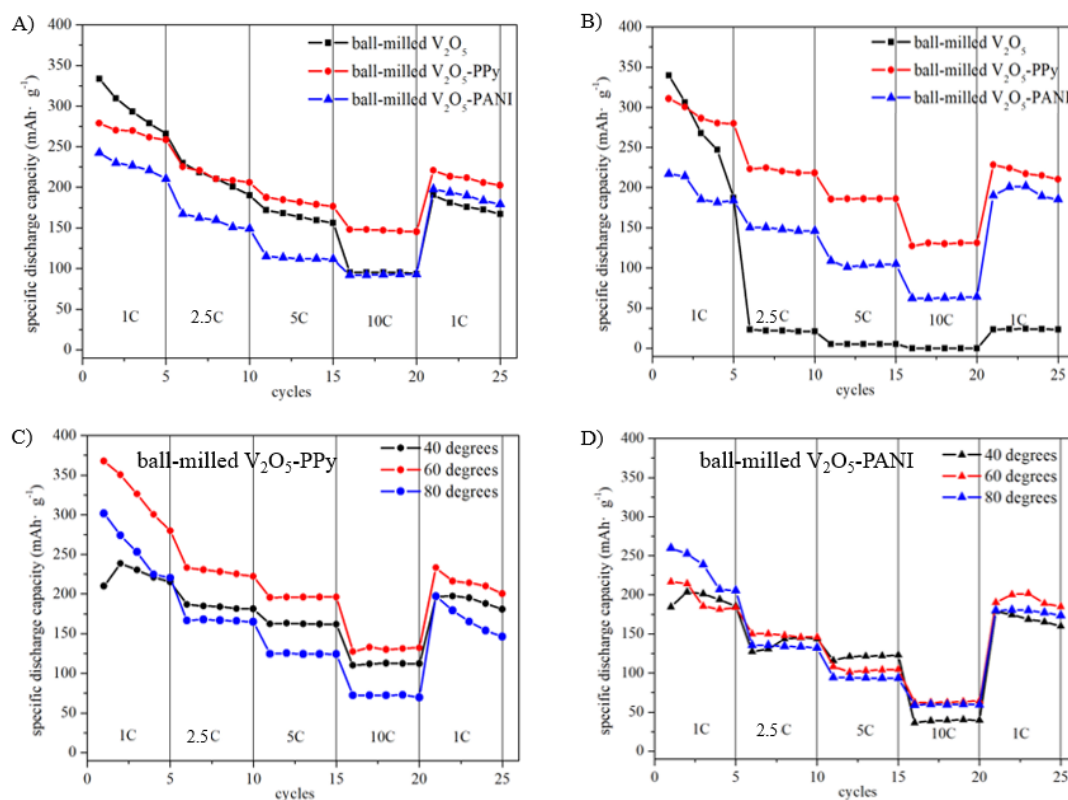


Figure 42. Rate performance of ball-milled V<sub>2</sub>O<sub>5</sub>, ball-milled V<sub>2</sub>O<sub>5</sub>-PPy and ball-milled V<sub>2</sub>O<sub>5</sub>-PANI samples at A) room temperature in coin cells (~ 1 cm<sup>2</sup> in cell) and B) at 60°C in large batteries (~ 9 cm<sup>2</sup> in cell) at different current densities. Rate capability of large batteries (~ 9 cm<sup>2</sup> in cell) containing C) ball-milled V<sub>2</sub>O<sub>5</sub>-PPy and D) ball-milled V<sub>2</sub>O<sub>5</sub>-PANI cathodes at 40°C, 60°C and 80°C at different current densities (1 C, 2.5 C, 5 C and 10 C). 1 C corresponds to 200 mA·g<sup>-1</sup>. All of them have mass loading around 4.5 mg·cm<sup>-2</sup>.

### 3.4.3 Cyclic Performance

Small coin batteries ( $\sim 1 \text{ cm}^2$  in cell) were conducted for cycling test at room temperature and the results are shown in Figure 43 A). Ball-milled  $\text{V}_2\text{O}_5$ -PANI manifests an outstanding cyclic performance, the discharge capacity retention is approximate 92.7% after 350 cycles. However, this cathode material only has a specific discharge capacity of  $125 \text{ mAh}\cdot\text{g}^{-1}$  at a current density of 5 C. As for PPy-coated and bare  $\text{V}_2\text{O}_5$  samples, the initial specific discharge capacities of these two cathode materials in RAZBs are  $195.7 \text{ mAh}\cdot\text{g}^{-1}$  and  $211.3 \text{ mAh}\cdot\text{g}^{-1}$ , respectively. A close initial capacity value is obtained which is much higher than that of PANI-coated cathode in RAZB. Because of a slightly thicker coating layer and a larger amount of PANI on  $\text{V}_2\text{O}_5$  surface, which are observed in TEM images and TGA results, the decreased rate of  $\text{Zn}^{2+}$  diffusion between the electrode and electrolyte arises during the reaction. When the test running over 30 cycles, the discharge capacities of PPy-coated battery exceeds the control one. Subsequently, the observation of capacity fading on PPy-coated battery shows a slower rate (17.0% within 350 cycles) than that on the control battery (53.3% within 350 cycles), as the percentages of capacity loss are listed in Table 3. In addition, the PPy-coated sample shows only 0.6% differences in capacity retention to ball-milled  $\text{V}_2\text{O}_5$ -PANI at room temperature after 200 cycles. PPy-coated battery deliveries a much higher capacity of  $175.5 \text{ mAh}\cdot\text{g}^{-1}$  at 5 C than PANI-coated battery since it possesses an ultrathin coating layer on  $\text{V}_2\text{O}_5$  surface.

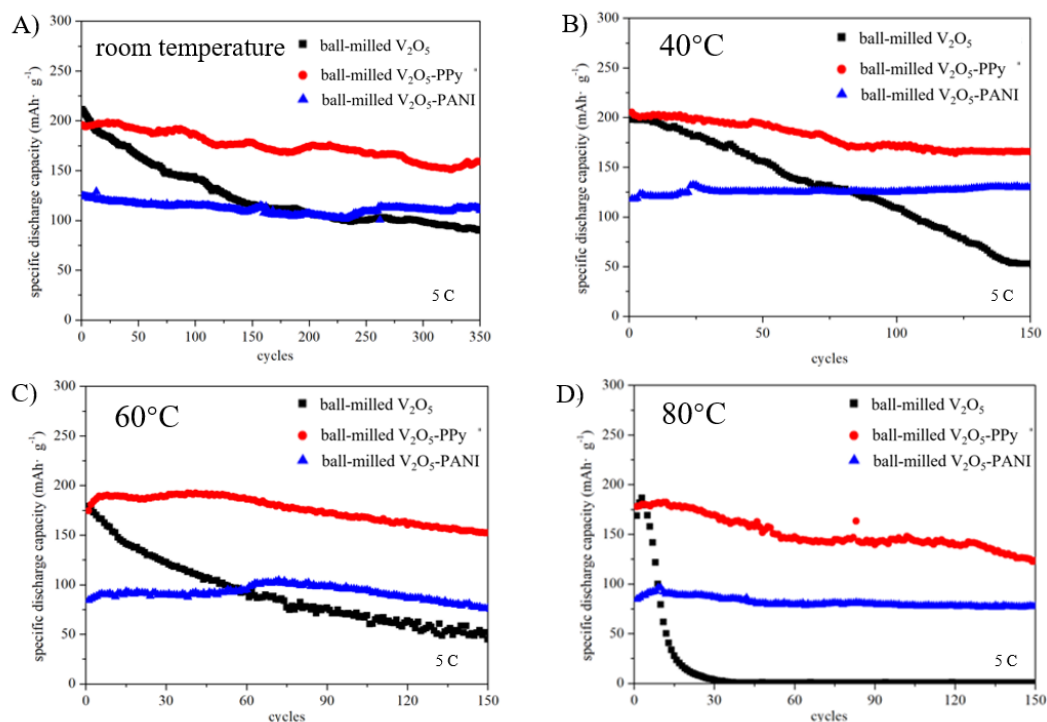


Figure 43. Galvanostatic cycling tests of ball-milled  $V_2O_5$ , ball-milled  $V_2O_5$ -PPy and ball-milled  $V_2O_5$ -PANI samples A) at room temperature in coin cells ( $\sim 1 \text{ cm}^2$  in cell), B) at  $40^\circ\text{C}$ , C)  $60^\circ\text{C}$  and D)  $80^\circ\text{C}$  in large batteries ( $\sim 9 \text{ cm}^2$  in cell) at a current density of 5 C over the voltage range of 0.2-1.6 V. All of them have mass loading around  $4.5 \text{ mg}\cdot\text{cm}^{-2}$ .

samples	cycle numbers		
	100	200	350
ball-milled $V_2O_5$	70.3 %	54.2 %	46.7 %
ball-milled $V_2O_5$ -PPy	96.6 %	90.5 %	83.0 %
ball-milled $V_2O_5$ -PANI	94.2 %	91.1 %	92.7 %

Table 3. Capacity retention at a current density of 5 C at room temperature.

As refer to the galvanostatic cycling tests of large battery ( $\sim 9 \text{ cm}^2$  in cell) at increased temperatures from 40 to 80°C, quite similar performance of the polymer-coated batteries are obtained in Figure 43 B) to D). Under high temperature conditions, dramatic capacity losses of ball-milled  $\text{V}_2\text{O}_5$  sample are demonstrated in the above cyclic patterns. In Table 4, only 25 % of initial capacity is maintained at 60°C after 150 cycles since the elevated temperature promotes  $\text{V}_2\text{O}_5$  dissolution in the acidic aqueous electrolyte, this result is well matched to the CV measurements at 60°C (Figure 41 A). Nevertheless, the data shown in Appendix 4 and Appendix 5 suggest over 80 % capacity retention of these two polymer-coated samples within 150 cycles at 60°C are obtained. In particularly, the PPy-modified sample shows a much larger initial capacity ( $189.5 \text{ mAh}\cdot\text{g}^{-1}$ ) than other samples under a same condition. According to the cyclic results in Figure 44 A) and B), the PPy-coated and PANI-coated samples maintain a relatively stable state of discharge capacity as the temperature gradually increases. These compact coating layers assist to prevent bare  $\text{V}_2\text{O}_5$  from detaching and dissolving in aqueous electrolyte at elevated temperatures. Moreover, within the first 50 cycles, apparent divergences of discharge capacities among these samples are observed at different temperatures. More notably, similar property enhancement is exhibited for both small ( $\sim 1 \text{ cm}^2$  in 0.98 mAh cell) and large ( $\sim 9 \text{ cm}^2$  in 9 mAh cell) batteries, this indicating an excellent potential for scale-up production and manufacturing.

temperatures \ cycle numbers	50	100	150
40°C	78.8 %	55.1 %	26.7 %
60°C	56.4 %	38.4 %	25.0 %
80°C	0.3 %	---	---

Table 4. Capacity retention of ball-milled V<sub>2</sub>O<sub>5</sub> sample with a current density of 5

C at different temperatures.

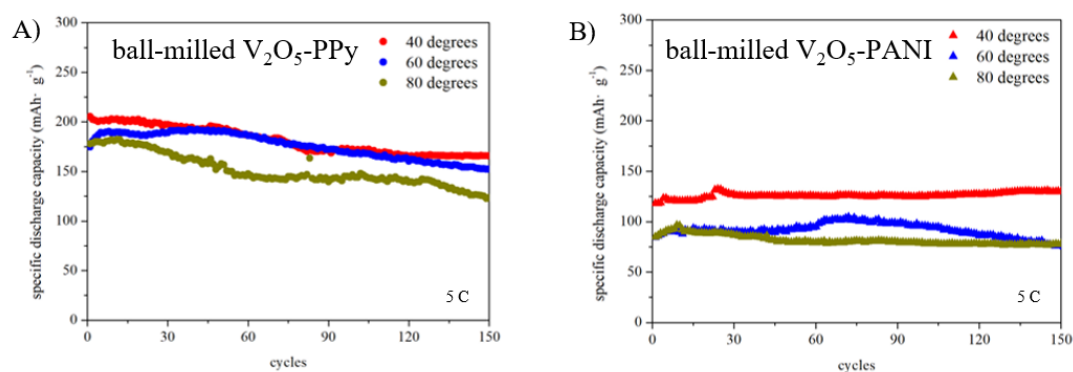


Figure 44. Galvanostatic cycling tests of A) ball-milled V<sub>2</sub>O<sub>5</sub>-PPy and B) ball-milled V<sub>2</sub>O<sub>5</sub>-PANI samples at 60°C in large batteries (~ 9 cm<sup>2</sup> in cell) at a current density of 5 C over the voltage range of 0.2-1.6 V. All of them have mass loading around 4.5 mg·cm<sup>-2</sup>.

### 3.4.4 Electrochemical Impedance Spectroscopy (EIS)

Further investigations of the discharge capacities were illustrated by electrochemical impedance spectroscopy (EIS) measurement. The impedances spectra

of  $V_2O_5$  and polymer-modified batteries were carried out over the frequency range of 1 MHz -10 mHz at different cycles. Figure 45 demonstrates the Nyquist plots of ball-milled  $V_2O_5$  and polymer- $V_2O_5$  electrodes at 50th cycling in fully discharged state. This Nyquist plot involves two contents, they are one semicircle locates at a high-frequency region and a Warburg straight line within intermediate frequency region. Generally in this battery system, the combination of electrode and electrolyte resistance represents equivalent serial resistance ( $R_s$ ), while  $R_{ct}$  stands by the resistance of electrons transfer from the electrode material to the ions in the liquid electrolyte [139]-[141]. The relationship among these elements is illustrated by an equivalent circuit which inserted in Figure 45. The intercepts on x-axis demonstrate the value of  $R_s$ , and the diameter of semicircle corresponds to  $R_{ct}$ . Therefore, in Figure 45 A), ball-milled  $V_2O_5$  and PPy-coated battery have very close  $R_s$  in RAZBs, while the PPy-coated battery shows a much smaller semicircle whose possesses a lower  $R_{ct}$ , the measured impedance results at ambient temperature are listed in Table 5. Herein, PPy-coated battery shows the lowest  $R_{ct}$  among others, suggesting a shorter length for electron transportation would be offered, so that a higher discharge capacity is delivered by PPy-modified battery. This result is corresponded well to its galvanostatic cycling plot in Figure 43 A). In the cyclic curves, the existence of a big gap between PPy-coated and PANI-coated batteries is observed at their 50th discharge capacities. However, the impedance measurement results of these two polymer-modified samples show very similar values in  $R_{ct}$  under ambient condition. The factor that causes PANI-coated battery have much lower

capacity is the larger  $R_s$  value (21.27 Ohm, as listed in Table 5) of pure conductive polymer-PANI as shown in Appendix 6. This condition might be due to the over-coating, or the synthesized PANI is not entirely oxidized in emeraldine base (half-oxidized state) [82]. Besides, much larger slopes are obtained in the Warburg linear region for PPy and PANI batteries, which represent higher Zn ion diffusion rates and better capacity behaviors are existed in these two polymer-coated samples during the cycling. Figure 45 B) and Appendix 7 are the impedance fitting results for samples under high temperature conditions. The noticeable difference between A) and B) in the Figure 45 is the intercept of control sample along x-axis shifts to a larger value as temperatures increases. This phenomenon can be explained by the increase of its electrolyte resistance since partial  $V_2O_5$  is dissolved into the aqueous electrolyte. As a result, a larger value of  $R_s$  in bare  $V_2O_5$  battery is obtained. Surprisingly, less obvious changes in  $R_s$  of these two polymer-coated batteries are exhibited, which supports the polymer coating can conserve  $V_2O_5$  from breaking down at high temperatures. As shown in Table 6, PANI-modified sample exhibited larger  $R_s$  and  $R_{ct}$  values at 60°C, thus, a lower specific discharge capacity is displayed in its cycling test (in Figure 43 C). Consequently, a perfect explanation of the cycling performance can be illustrated by EIS results.  $R_{ct}$  benefits PPy-coated batteries possess much higher specific discharge capacities than the control sample after 50 cycles, whereas larger  $R_s$  leads PANI batteries have much lower capacities than others. Also, the measured impedance of PPy at 60°C and 80°C show an enormous difference in  $R_{ct}$  values, as found in Table 6 and

Appendix 8. The  $R_{ct}$  value (12.39 Ohm) at 80°C is 6 times of the  $R_{ct}$  (2.93 Ohm) at 60°C, which corresponds to its capacity difference at 50th cycling in Figure 44 A). Overall, polymer-protected samples exhibited better cyclic performance because of the polymeric layer protection and their stable thermal properties, especially at high temperatures.

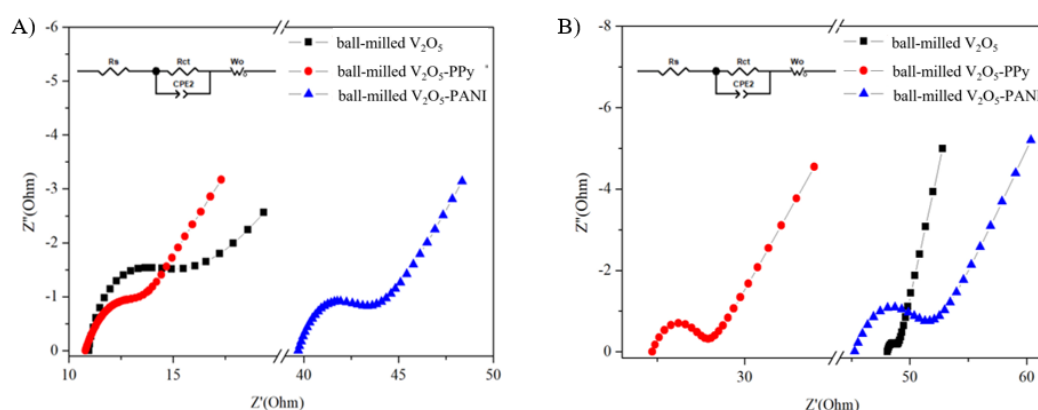


Figure 45. Nyquist plots of three samples at their 50th cycle under A) room temperature, and B) 60°C.

samples	impedance	
	$R_s$ (Ohm)	$R_{ct}$ (Ohm)
ball-milled $V_2O_5$	10.19	3.69
ball-milled $V_2O_5$ -PPy	10.37	2.10
ball-milled $V_2O_5$ -PANI	39.26	2.84
Conductive polymer-PPy	8.91	---
Conductive polymer-PANI	21.27	---

Table 5. EIS measurement results at room temperature.

samples	impedance	
	$R_s$ (Ohm)	$R_{ct}$ (Ohm)
ball-milled $V_2O_5$	47.94	0.90
ball-milled $V_2O_5$ -PPy	24.32	2.93
ball-milled $V_2O_5$ -PANI	45.21	6.19

Table 6. EIS measurement results at 60°C.

### 3.5 Section Conclusions

In this project, two different kinds of conductive monomers with the same input amounts (10 wt%) were used to form compact and ultrathin coating layers on the surface of bare  $V_2O_5$  via in-situ polymerization method. The compositions of the polymer layers were analyzed by FTIR and XPS technologies. Base on XRD patterns, polymer modification would not affect the active material structure, while enhancing the material crystallinities. The TEM detected the thickness of PANI layer is twice as much for the PPy layer, and the mass percentages of polymer compositions in cathode materials were measured by TGA technique. Both polymer-coated RAZBs are revealed the enhanced rate capabilities and cycling stabilities. Compared the electrochemical results of PPy and PANI batteries, PPy battery displayed a higher capacity of 195.7  $\text{mAh}\cdot\text{g}^{-1}$  at a current density of 5 C with a similar capacity loss (9.5%) at room temperature after 200 cycles (merely 0.05% per cycle). Even at 60°C, the PPy sample remained 80% of its initial discharge capacity ( $152 \text{ mAh}\cdot\text{g}^{-1}$ ) after 150 cycles. Therefore, PPy-coated electrode possesses an ultrathin coating layer on raw material,

presenting a better electrochemical performance under the ambient and high temperatures (40°C, 60°C and 80°C). Furthermore, the usage of surface coating method by conductive polymers provides a favorable approach to realize a thermally stable energy storage system, which can be considered as an alternative to lithium-ion batteries.

## **Chapter 4. Dual-ion Doped Vanadium Oxide as the Cathode Material in Rechargeable Aqueous Zinc-ion Batteries**

### **4.1 Synthesis of Dual-ion Inserted Vanadate Material**

Hydrothermal method is one of the most popular method for crystal growth. It is conducted under high temperature solution and vapor pressure, and utilized to synthesize the raw material into diverse structures, such as wires, rods, belts, sheets and spheres... A temperature gradient is maintained between the opposite ends of the growth chamber. The solute is dissolved at the end of hotter, while at the cooler end it would deposit on a seed crystal, growing the desired crystal. Through this method, the particle size of the new synthesized material is in nanoscale and a large specific surface area would be offered [61][62].

More specifically, 0.366 g commercial  $V_2O_5$  and 0.2 g polyethylene glycol (MW=4000) (PEG-4000, Scientific Polymer Products Inc.) are stirred vigorously in 60 mL DI water for 15 min. After that, placing the suspension to sonicate at least 20 min. Subsequently, determined amounts of 1 M sodium hydroxide (NaOH, Sigma-Aldrich,  $\geq 97\%$  purity) solution and 1 M zinc chloride ( $ZnCl_2$ , Sigma-Aldrich,  $\geq 97\%$  purity) solution were separately added into the mixture by the molar ratio of Zn: Na=0.65:1. After mixing for 30 minutes, the solution was transferred to a 100 mL Teflon vessel, and sealed with an autoclave. Then, placing it into a high temperature oven followed by a reacted condition under 190 °C for 24 hours.

After the reaction was finished, using DI water and ethanol solution to wash the synthesized material for several times, finally dried this sample at 60°C in vacuum oven for at least 20 hours. The color of the obtained product was green, as shown in Figure 46. Additionally, V<sub>2</sub>O<sub>5</sub> nanobelts (Appendix 9) without doping metal ions as a control sample were produced under the same condition (190 °C for 24 hours).

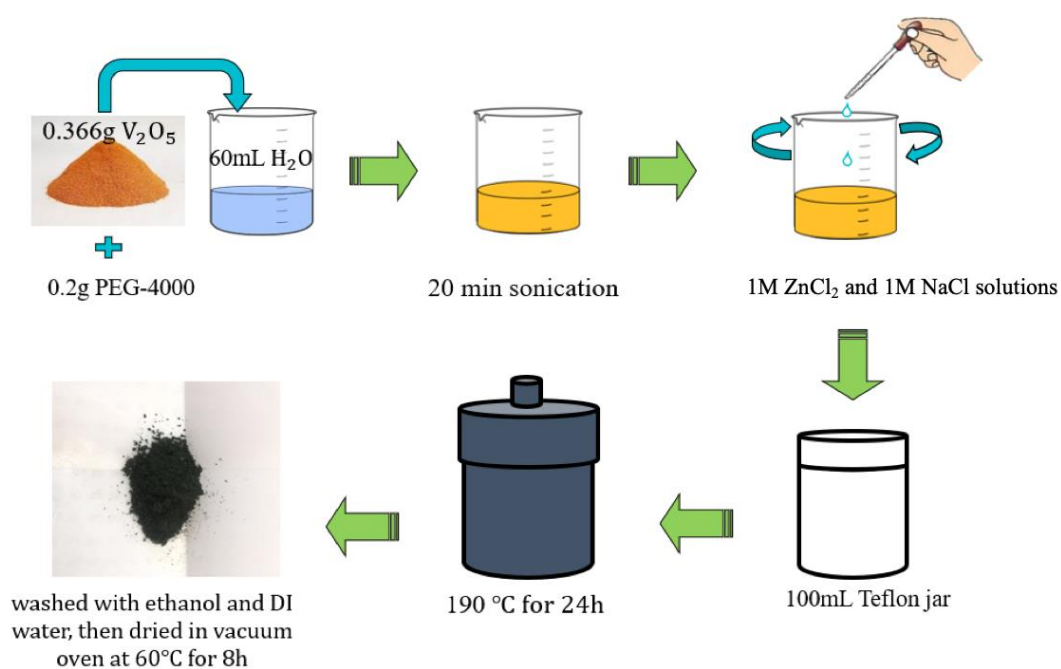


Figure 46. Experimental procedure of synthesizing dual-ion inserted vanadate material.

## 4.2 Cathode Fabrication and Battery Assembling

The electrode consists of 70 wt% active material (ZNVO or  $V_2O_5$  nanobelts), 20 wt% GNP, and 10 wt% PVDF in NMP solution. The slurry is pasted on the PE film and dried at 60°C for 8 hours.

Both CR2032 coin-type and T-cell (Swagelok) batteries were employed for electrochemical tests. The battery assembly is almost same for both types. The cathode is punched into small disks of 12 mm in diameter, with a mass loading of active material around  $2.3 \text{ mg} \cdot \text{cm}^{-2}$ . RAZB is assembled by the cathode containing vanadium-based material, double-layered AGM (diameter: 12 mm, thickness: 0.5 mm) as the separator, and polished metal zinc (diameter: 12 mm, thickness: 0.2 mm) as the anode. Three kinds of electrolytes were employed in this system, they are 2M zinc sulfate ( $ZnSO_4$ , Sigma-Aldrich,  $\geq 98\%$  purity), 2M sodium sulfate ( $Na_2SO_4$ , Sigma-Aldrich,  $\geq 99\%$  purity) and 2M  $ZnSO_4 + 2M Na_2SO_4$  aqueous electrolytes with pH value of  $3.7 \pm 0.2$ .

## 4.3 Material Characterizations

### 4.3.1 Scanning Electron Microscopy (SEM)

Scanning electron microscopy (SEM) was utilized to detect the morphology and nanostructure of metal-ion doped  $V_2O_5$  (ZNVO). The ZNVO sample was obtained via a simple synthesis process (hydrothermal method), and the raw material (commercial  $V_2O_5$ ) and its 1D nanobelts are clearly projected in SEM images (Figure 47). It should

be pointed out that these nanobelts have a tendency to assemble together and form bundles in tens of micrometers in length and 100-300 nm in width. In addition, the element composition can be roughly detected by energy-dispersive X-ray (EDX or EDS) technique. As shown in Figure 47 C), both Zn and Na elements are observed in the EDX pattern, which supports the successes of dual metal-ion insertion.

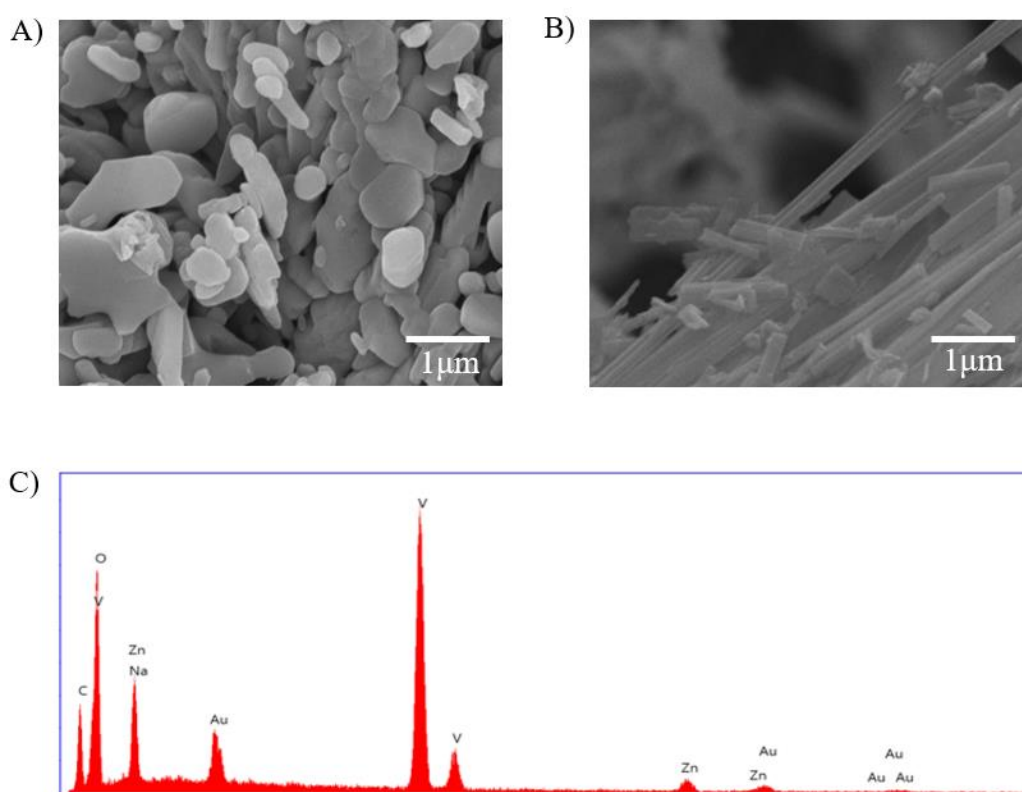


Figure 47. SEM images of A) commercial  $V_2O_5$  and B) synthesized ZNVO nanobelts with scale bar of 1  $\mu\text{m}$ . C) EDX image of ZNVO sample.

### 4.3.2 Inductively Coupled Plasma Mass Spectrometry (ICP-MS)

The quality of each element in ZNVO sample can be directly reported by the inductively coupled plasma mass spectrometry (ICP-MS) technique. Firstly, the origin sample ZNVO was dissolved in dilute nitric acid, and after ICP detection, the concentrations for all elements are obtained and listed in the below table (Table 7). Finally, the mole ratio of Zn : Na : V is calculated in 0.3 : 0.43 : 1, thus the conformed material composition is  $Zn_{0.3}Na_{0.43}V_2O_5$ . Moreover, ICP technique also can be employed to detect the charge / discharge product compositions of the positive electrode, so that the number of transfer electrons could be calculated by the corresponded capacities. This calculation will not include in this thesis but as the research future work.

element	Zn	Na	V
mean (mg/L)	8.6592	4.4183	45.7571

Table 7. Concentrations for each element in ZNVO sample.

### 4.3.3 X-ray Photoelectron Spectroscopy (XPS)

XPS is another effective way to verify the element composition. In Figure 48 A), C) and D), both Zn and Na elements can be observed in these XPS spectrums, which support the existence of Zn and Na elements in the sample. In addition, XPS technique

is also widely used to investigate the de- / intercalation of ions during charge / discharge process. The shift of peak locations corresponds to their different element valances. From the Figure 48 B), the V 2p scan of the pristine ZNVO sample is presented in energy levels of 2p<sub>3/2</sub> and 2p<sub>1/2</sub>, all the peaks locate at these two regions are assigned to the valance of 5+. However, peaks of V would shift to other positions in its energy level, which making V present in different oxidation states (V<sup>3+</sup>, V<sup>4+</sup> or V<sup>5+</sup>) during the reaction. Therefore, the usage of XPS would assist to study the mechanism of electrochemical reactions for the future work.

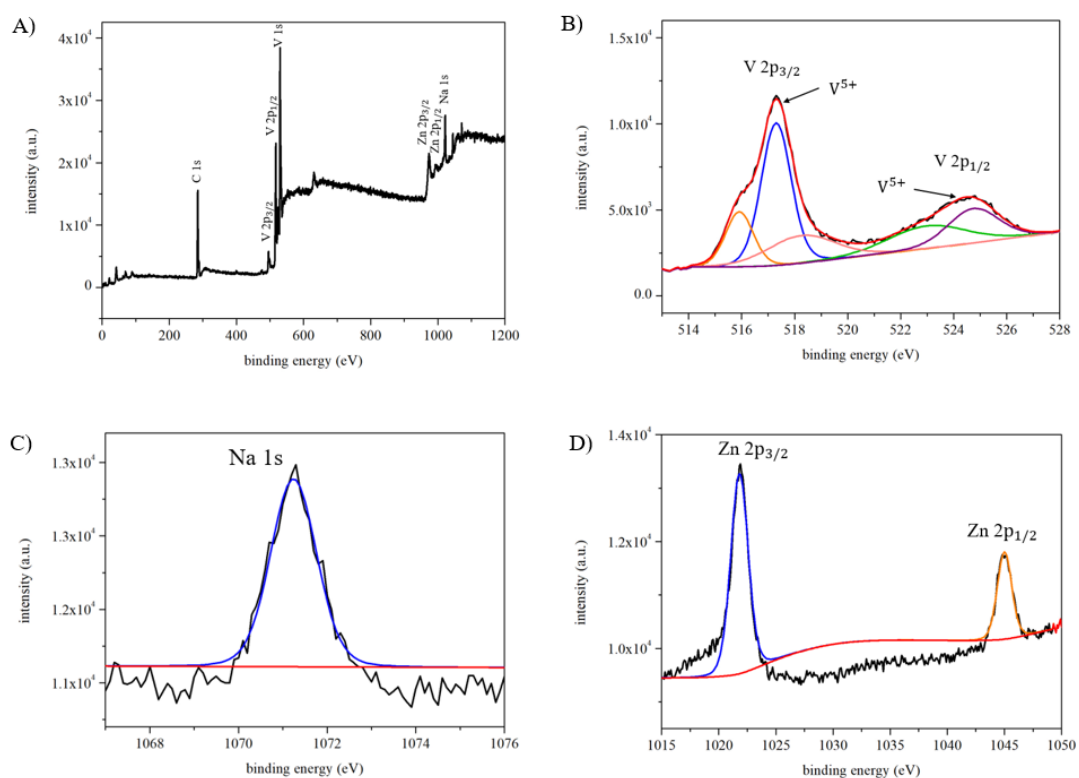


Figure 48. XPS spectra of pristine ZNVO sample in A) survey spectrum, B) V 2p spectrum, C) Na 1s spectrum and D) Zn 2p spectrum.

## 4.4 Basic Electrochemical Performance

### 4.4.1 Cyclic Performance

The electrochemical performance of ZNVO as the positive electrode of RAZB were examined in assembled coin cells. In the contrast of the traditional alkane electrolyte presents fast capacity fading and poor coulombic efficiency, mildly acidic electrolyte prepared by 2M ZnSO<sub>4</sub> in DI water (pH=3.7 ± 0.2) were utilized in this battery system. In order to investigate the effects on battery capacities by metal-ion insertion, the comparisons between V<sub>2</sub>O<sub>5</sub> and ZNVO nanobelt electrodes in RAZBs are conducted via galvanostatic cycling tests at a current density of 5 C. As shown in Figure 49 A), the ZNVO cathode in 2M ZnSO<sub>4</sub> electrolyte (red dot) deliveries a much higher initial discharge capacity (over 300 mAh·g<sup>-1</sup>) than that of V<sub>2</sub>O<sub>5</sub> nanobelt electrode (black dot). However, the capacities for both electrodes fade dramatically in the following cycles, this might due to the dissolution of nanobelts and the growth of zinc dendrites on anode.

To relieve this situation, additional metal ions (e.g. Na ions) possess lower reduction potential was supplied in the electrolytic solution. Surprisingly, as adding Na<sub>2</sub>SO<sub>4</sub> into original 2M ZnSO<sub>4</sub> electrolyte, the Zn // ZNVO battery exhibits an excellent cyclic performance and a discharge capacity of 190.2 mAh·g<sup>-1</sup> is achieved at 5 C (in Figure 49 B). This dual-ion system (contains both dual metal-ion doped positive electrode and dual-carriers electrolyte) presents a highly durable and extremely long cycle life with capacity retention approximate 89.1% even over 4000 cycles. Moreover,

this superb cycling performance is presented by the galvanostatic discharge curves of ZNVO cathode in dual-ion electrolyte (as shown in Figure 49 C). This is because Na ions work as dual carriers in the electrolyte, providing great support on reducing the dissolution of ZNVO nanobelts and suppressing zinc dendrites formation during the cycling process. The function of Na ions on inhibiting dendrite growth will be discussed in the followed Anode Characterization section.

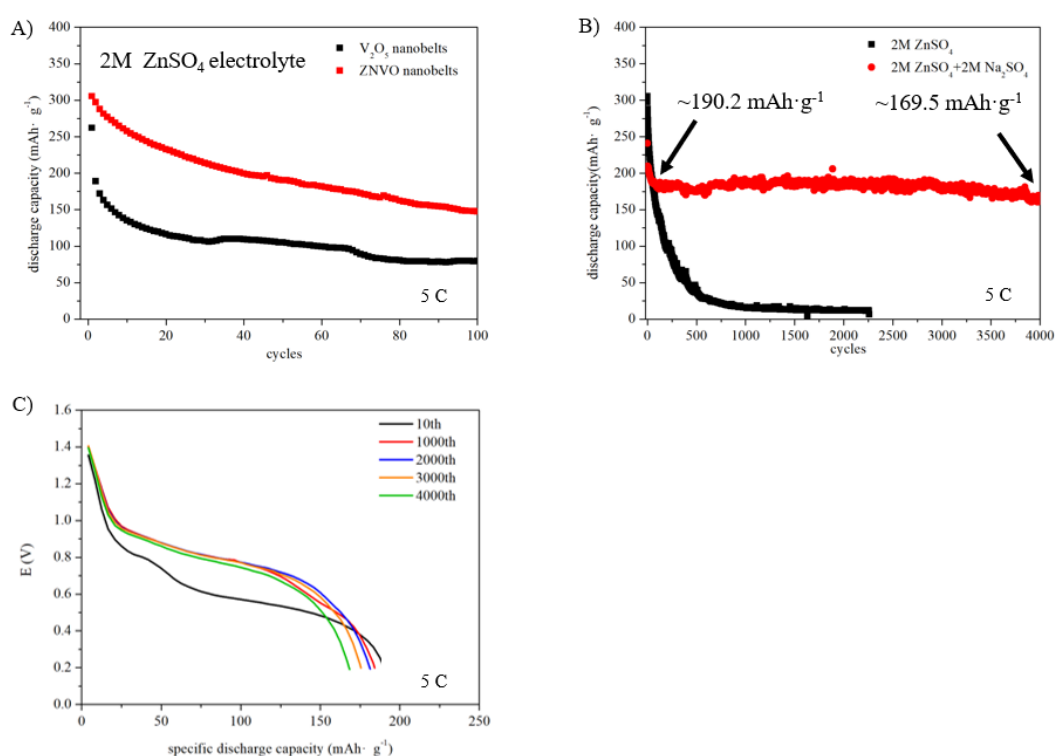


Figure 49. Cycling performance of A) V<sub>2</sub>O<sub>5</sub> and ZNVO nanobelts electrodes in 2M ZnSO<sub>4</sub> electrolyte and B) ZNVO electrode in 2M ZnSO<sub>4</sub> electrolyte with and without Na<sub>2</sub>SO<sub>4</sub> addition. C) The galvanostatic discharge curves of ZNVO cathode in dual-ion electrolyte. All tests are conducted in coin cells at a current density of 5 C in a voltage range of 0.2-1.6 V. All of them have mass loading around 2.3 mg·cm<sup>-2</sup>.

#### 4.4.2 Rate Capability

High rate capability is crucial to realize practical manufacturing of RAZBs in grid energy storage applications. Apart from the high capacity retention and long cycle life, the ZNVO electrode in 2M ZnSO<sub>4</sub> + 2M Na<sub>2</sub>SO<sub>4</sub> aqueous electrolyte (red line) exhibits a superior rate performance as shown in Figure 50. In this dual-ion system, ZNVO electrode offers average discharge capacities of 291.6, 260.3, 222.3, 191.3, 172.8 and 159.6 mAh·g<sup>-1</sup> at current densities of 0.5, 1, 2.5, 5, 7.5 and 10 C, respectively. After the cycling reaches high current density, an average discharge capacity of 308.6 mAh·g<sup>-1</sup> can be recovered as its current density returns to 0.5 C. As a result, over 100% of the capacity retention is achieved which is much higher than that of ZNVO electrode in 2M ZnSO<sub>4</sub> electrolyte (black line). This result implies the excellent rate capability of ZNVO electrode accompanied by 2M ZnSO<sub>4</sub> + 2M Na<sub>2</sub>SO<sub>4</sub> aqueous electrolyte.

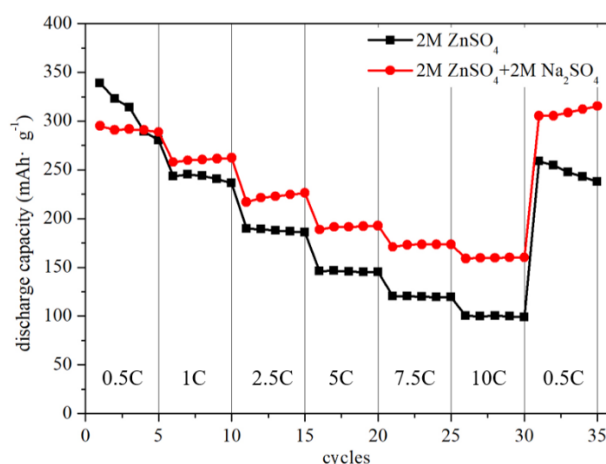


Figure 50. Rate performance of ZNVO electrode in different electrolytes at various current densities, where 1C corresponds to 200 mA·g<sup>-1</sup>.

#### 4.4.3 Cyclic Voltammetry (CV)

Figure 51 A) and B) present the initial three cycles of CV plots for ZNVO electrode in different electrolytes at a scan rate of  $0.1 \text{ mV}\cdot\text{s}^{-1}$  with the potential window of 0.2-1.6 V vs.  $\text{Zn}^{2+} / \text{Zn}$ . Both of them obviously present three oxidation peaks and two reduction peaks. For the CV profile of ZNVO electrode in  $2\text{M ZnSO}_4 + 2\text{M Na}_2\text{SO}_4$  electrolyte, the sweep of the first cycle is slightly different from the followed two cycles in terms of the peak locations (Figure 51 B). The presence of peak shifting in first cycle is due to the activation process of the fresh electrode, which corresponds to a quick capacity drop between 1st and 2nd cycle in its cycling plot (Figure 49 B). Interestingly, after comparing A) and B) in Figure 51, two reduction peaks and the first two oxidation peaks are hold similar positions in their first three cycles, while the third oxidation peak shifts from 1.38 V to 1.45 V with the addition of Na ions in electrolyte. Nevertheless, the third peak in anodic sweeping is disappeared with increased cycle number, as shown in Figure 51 C) and D). Therefore, this oxidation peak locates at 1.38 V or 1.45 V presents a nonreversible process, as Na ions come from ZNVO only extract from the raw lattice into the aqueous electrolyte without a back insertion. It is notable that, a pair of redox peaks locate at 1.1 / 0.8 V is enhanced in this dual-ion electrolyte as the cycling increased. However, the response currents of the same redox peaks in  $2\text{M ZnSO}_4$  electrolyte battery exhibit dramatic reduction from the 50th cycles to 500th cycles, indicating a decreased capacity of this battery since the integrated areas of CV curves are lowered down. By contrast, the areas of CV plots in Figure 51 D) is maintained

stable within 500 cycles. Thus, the outstanding reversibility and stability of this dual-ion battery system can be demonstrated, which is perfectly matched with the outcome of high capacity retention obtained in cycling tests.

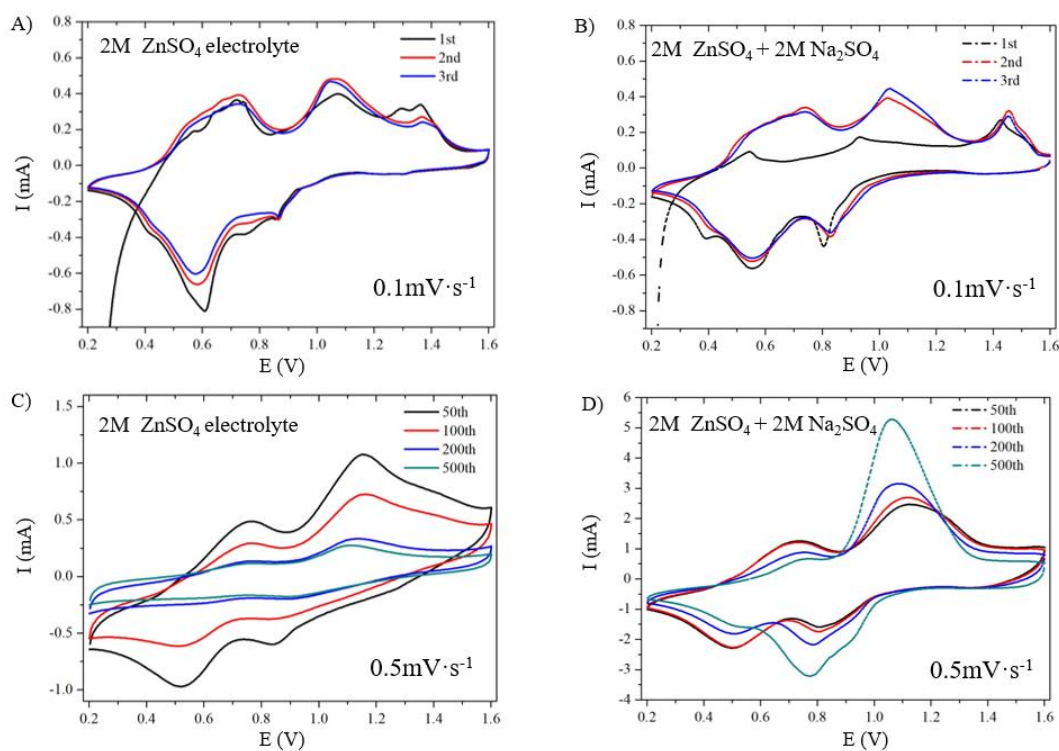


Figure 51. Cyclic voltammograms of ZNVO electrode in A) 2M  $ZnSO_4$  and B) 2M  $ZnSO_4 + 2M Na_2SO_4$  electrolyte at a scan rate of  $0.1\text{ mV}\cdot\text{s}^{-1}$ . Cyclic voltammograms of ZNVO electrode in C) 2M  $ZnSO_4$  and D) 2M  $ZnSO_4 + 2M Na_2SO_4$  electrolyte at a scan rate of  $0.5\text{ mV}\cdot\text{s}^{-1}$  at selected cycle numbers.

## 4.5 Anode Characterizations

As mentioned in above section 1.5, adding Na ions into electrolyte assists to inhibit zinc dendrite growth on anode surface during charging process. Since the  $\text{Na}^+$  (-2.71 V) has much lower reduction potential than  $\text{Zn}^{2+}$  (-0.76 V), the coming  $\text{Zn}^{2+}$  can be repelled to distribute on adjacent substrate according to the electrostatic shield mechanism [106].

To find out an appropriate concentration of sodium salts ( $\text{Na}_2\text{SO}_4$ ) in an electrolytic solution. Gradient increased amounts of  $\text{Na}_2\text{SO}_4$  (0.5, 1, 1.5 and 2M) were separately added in 2M  $\text{ZnSO}_4$  solution to prepare electrolytes. After comparing the testing results,  $\text{Na}_2\text{SO}_4$  at a concentration of 2M in electrolytes exhibited the best electrochemical performance of batteries. Herein, we will show the positive works on the anode by this dual-ion aqueous electrolyte.

From Figure 52 A) to C), in 2M  $\text{ZnSO}_4$  electrolyte, large amounts of harsh and vertical zinc dendrites are grown on the anode surface with increased cycle numbers. However, in an electrolyte with rich Na ions (dual-ion electrolyte), the surface of negative electrode is uniform and smooth (in Figure 52 D to F). Even after 500 cycles (Appendix 10), very fewer amounts of zinc dendrites are formed in the lateral level which provides a flat morphology on the anode surface. This indicates the important effects of Na ions on suppressing dendrite formation of anodes.

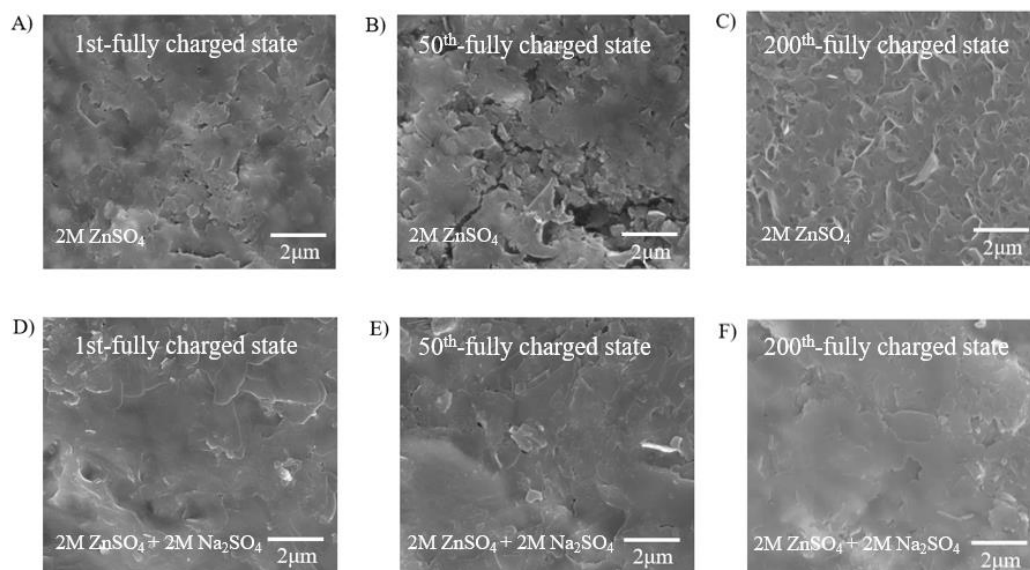


Figure 52. SEM images of anode surface in different electrolytes at their selected cycles at fully charged state. Scale bars, 2  $\mu\text{m}$ .

## 4.6 Advanced Characterizations

To investigate the energy storage mechanism of dual-ion inserted electrode in these aqueous batteries during cycling, advanced characterizations such as XRD, FTIR and CV need to be conducted.

### 4.6.1 Cyclic Voltammetry (CV)

The reversible extraction / insertion of ions during charge / discharge process can be established by CV measurements. Because of the activation behavior on the first cycle for the positive electrode (as discussed in section 4.4.3 Cyclic Voltammetry (CV)), the investigations of ion de- / intercalation and its corresponded redox peaks will be analyzed from the second cycle.

Two pairs of redox peaks shown in Figure 51 B) are commonly considered as the multiple-steps for Zn ion extraction and insertion [105][107]. However, in this study, we wonder if the Na ions in the electrolyte are involved in the reaction or not. Therefore, CV plots of ZNVO electrode in different electrolytes (2M ZnSO<sub>4</sub> + 2M Na<sub>2</sub>SO<sub>4</sub> and 2M Na<sub>2</sub>SO<sub>4</sub>) are conducted, as shown in Figure 53 A). In 2M Na<sub>2</sub>SO<sub>4</sub> electrolyte, only one reduction peak locates at 0.8 V is observed, after comparing with ZNVO electrode in 2M ZnSO<sub>4</sub> + 2M Na<sub>2</sub>SO<sub>4</sub> electrolyte, the disappeared reduction peak at 0.55 V should correspond to the insertion of Zn ions. This is because as Zn ions extract from ZNVO electrode into electrolyte during the charge process, the amount of Zn ions in electrolyte are not enough to assist the extracted Zn ions to complete the insertion process during charging process. However, we could not confirm the rest pair of redox peaks at 1.0 / 0.8 V presents Na ions de- / intercalation. Even though the existence of Zn ions with an extremely small amount in electrolyte (these Zn ions only come from electrode material), they may involve in the reaction. Take this into consideration, we fabricate another electrode material NVO by inserting with single metal ion (Na ion), then conducting the CV measurements of this electrode in 2M Na<sub>2</sub>SO<sub>4</sub> electrolyte. It is noted that, zinc anode is replaced by a graphite rod which is used as the counter electrode in the T-cell system. This action can remove the Zn ions in the battery system, and get rid of the effects of Zn ions on the peaks shown in CV curves.

In Figure 53 B), the NVO electrode shows one reduction peak (around 0.8 V) that is close to the position of corresponded peak for ZNVO electrode, and the curves of

two oxidation peaks at 1.0 V and 1.5 V are perfectly overlapped with ZNVO electrode. More importantly, the oxidation peak at 0.56 V is vanished in the CV profile of NVO electrode, illustrating the extraction of Zn ions has not occurred in NVO system. Thus, the redox peaks at 0.72 / 0.55 V represent the extraction / insertion of Zn ions. Although the redox peaks at 1.0 / 0.8 V stand for the behavior of Na ions during cycling, we still could not verify that no reactions for Zn ions occur at the same voltages since the response current is reduced at 0.8 V. Therefore, we demonstrate that both Zn and Na ions are involved in the chemical reactions of this dual-ion battery system (Zn / 2M ZnSO<sub>4</sub> + 2M Na<sub>2</sub>SO<sub>4</sub> / ZNVO): the redox peaks at 0.72 / 0.55 V manifest the reversible pathway of Zn ions extract / insert from / into V<sub>2</sub>O<sub>5</sub> interlayers; another pair at 1.0 / 0.8 V is dominated by Na ions de- / intercalation, but may contain the chemical reactions of Zn ions.

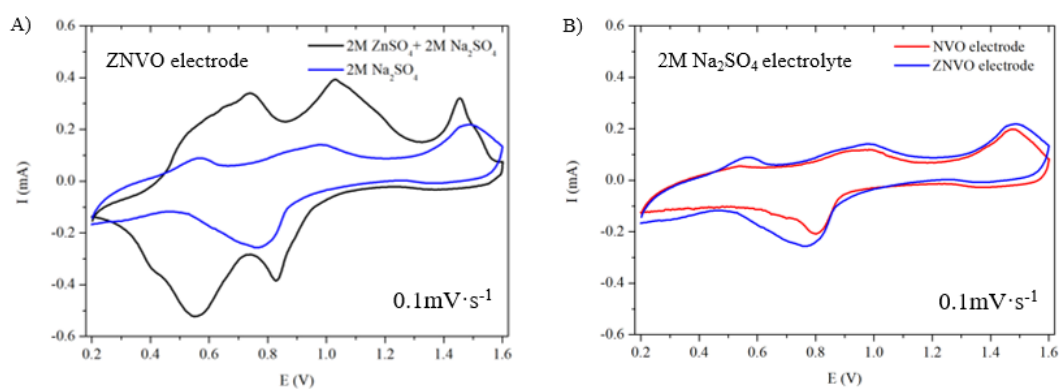


Figure 53. CV plots of A) ZNVO electrode in different electrolytes and B) NVO and ZNVO in 2M Na<sub>2</sub>SO<sub>4</sub> electrolyte at their 2nd cycling at a scan rate of  $0.1 \text{ mV} \cdot \text{s}^{-1}$ .

#### 4.6.2 X-Ray Diffraction (XRD)

For further understanding the energy storage mechanism of Zn // ZNVO battery with 2M ZnSO<sub>4</sub> + 2M Na<sub>2</sub>SO<sub>4</sub> electrolyte, various ex situ tests, including XRD and FTIR were utilized to analyze the positive electrode at the selected states of 2nd charge / discharge cycling. In this section, the reversible ions (Zn<sup>2+</sup> and Na<sup>+</sup>) de- / intercalation process between V<sub>2</sub>O<sub>5</sub> lattice and electrolyte would be investigated by ex situ XRD patterns. Two regions in Figure 54 A) will be discussed here.

In region ① (Figure 54 B), the reflection (111) of sodium vanadium oxide (NVO) at 26.4° shifts to lower 2θ positions as discharging from 1.6 to 0.2 V. In this process, the space of V<sub>2</sub>O<sub>5</sub> interlayer is expanded since the Na ions are inserted into the V<sub>2</sub>O<sub>5</sub> structure. Subsequently, the reflection (111) gradually shifts back as charging to 1.6 V, indicating the extraction process of Na ions from V<sub>2</sub>O<sub>5</sub> interlayers during the charge process. In addition, the zinc vanadium oxide (ZVO) also display a reversible de- / intercalation of Zn ions during the charge / discharge process, as marked in blue dot line. Interestingly, zinc sulfate hydroxide hydrate (Zn<sub>4</sub>SO<sub>4</sub>(OH)<sub>6</sub> · 5H<sub>2</sub>O, PDF# 39-0688) displayed in region ② is generated during the discharging process and gradually disappeared after charging from 0.2 to 1.6 V (as shown in Figure 54 C). This illustrates a reversible and successive decomposition / formation of Zn<sub>4</sub>SO<sub>4</sub>(OH)<sub>6</sub> · 5H<sub>2</sub>O on the positive electrode during charge / discharge process. Therefore, the reversible behavior of ions reveals good structural stability of ZNVO electrode in dual-ion electrolyte during the charge and discharge processes.

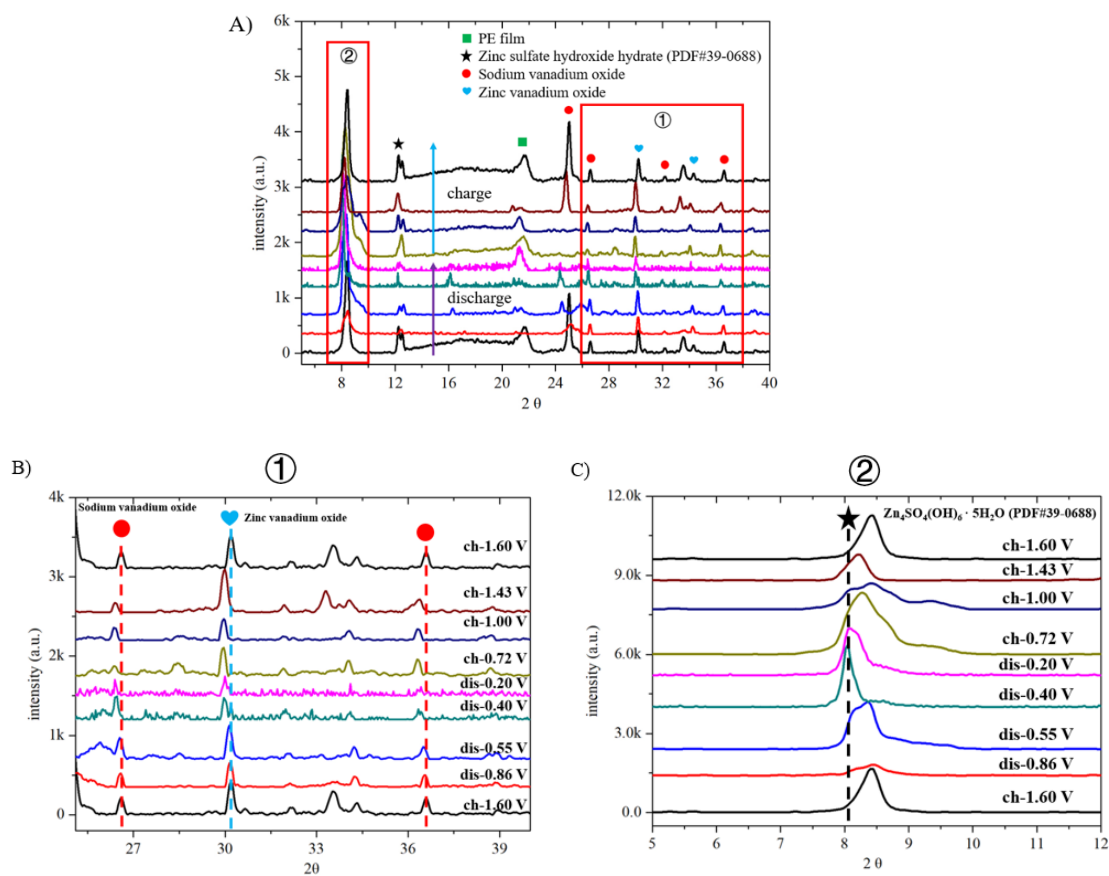


Figure 54. Ex situ XRD patterns of ZNVO electrode in 2M ZnSO<sub>4</sub> + 2M Na<sub>2</sub>SO<sub>4</sub>

electrolyte at determined voltages at their 2nd cycle.

#### 4.6.3 Fourier Transformed Infra-Red Spectroscopy (FTIR)

Another ex situ technique was also used to verify the mechanism of Zn<sub>4</sub>SO<sub>4</sub>(OH)<sub>6</sub> · 5H<sub>2</sub>O compound on positive electrode during cycling. As illustrated in Figure 55, the absorption band locates at 1125 cm<sup>-1</sup> is assigned to SO<sub>4</sub><sup>2-</sup> in Zn<sub>4</sub>SO<sub>4</sub>(OH)<sub>6</sub> · 5H<sub>2</sub>O [105]. The intensity of this band is gradually enhanced as discharging from 0.86 to 0.2 V, while in the charge process, it becomes much weaker at its fully charged state.

Therefore, the reversible formation and decomposition of  $\text{Zn}_4\text{SO}_4(\text{OH})_6 \cdot 5\text{H}_2\text{O}$  on ZNVO electrode can be proved by FTIR spectra.

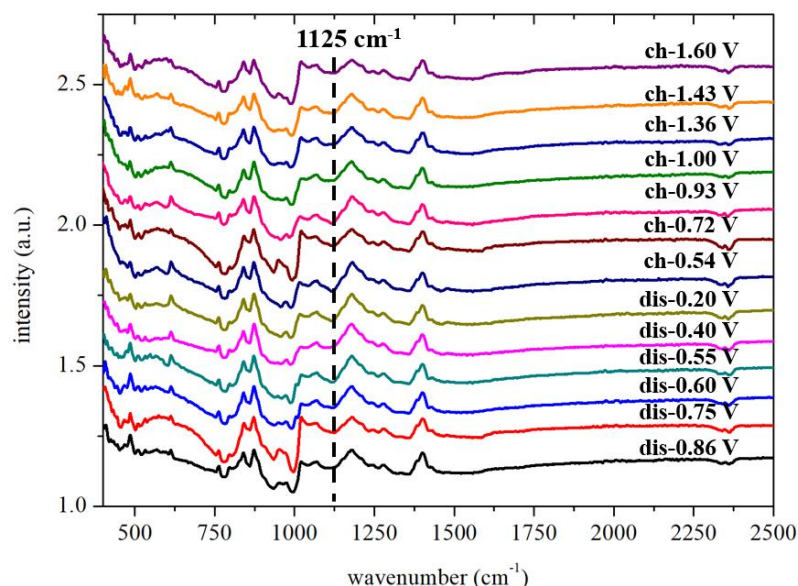


Figure 55. FTIR spectra of ZNVO electrode in 2M  $\text{ZnSO}_4 + 2\text{M Na}_2\text{SO}_4$  electrolyte at determined voltages at their 2nd cycle.

## 4.7 Section Conclusions

In this project, a new kind of vanadate cathode material with dual metal-ion insertions was successfully synthesized via hydrothermal method. It was produced as long nanobelts in an average width of 200 nm, and the composition of this material ( $\text{Zn}_{0.3}\text{Na}_{0.43}\text{V}_2\text{O}_5$ ) was detected by ICP-MS and XPS techniques. Surprisingly, this Zn // ZNVO battery provides excellent cyclic performance (~ 89% capacity retention over 4000 cycles) and high rate capabilities in an aqueous electrolyte with additional sodium

salt, and a specific discharge capacity of  $190 \text{ mAh}\cdot\text{g}^{-1}$  at a current density of  $5 \text{ C}$  is delivered by this dual-ion system. The dual-ion electrolytic solution not only assists to suppress zinc dendrites growth on anode, but also reduces the dissolution of cathode material in the aqueous environment. Furthermore, the energy storage mechanism of this dual-ion system was investigated by XRD, FTIR and CV tests. The reversible and successive de- / intercalation processes of ions ( $\text{Na}^+$  and  $\text{Zn}^{2+}$ ) during cycling can perfectly explain the superb electrochemical performances of ZNVO electrode in aqueous batteries. Therefore, this dual-ion system (contains both dual metal-ion doped positive electrode and dual-ion electrolyte) holds a silver hope on realizing the practical manufacturing of RAZBs, and pave a way for potential electric applications in grid energy storage.

## Chapter 5. Summary of Thesis and Recommendations for Future Work

Rechargeable aqueous zinc battery (RAZB) represents a promising energy storage system for its high energy density, high safety and low-cost. Among available cathode materials for RAZBs,  $V_2O_5$  is being considered thanks to its high specific discharge capacity, and the ease of Zn intake / extraction due to layered crystalline structure. However, this turned out to be a false hope because  $V_2O_5$  had very poor cycling performance and cannot be applied as power sources in electric products. The cause has been generally agreed to be the  $V_2O_5$  dissolution into the aqueous electrolyte, but the solution has evaded the community. Therefore, to stabilize its layered structure and decrease the solubility of  $V_2O_5$  in aqueous electrolyte systems, two effective strategies involving surface coating and doping metal ions on  $V_2O_5$  were optimized in this project.

In the first sub-project, conductive polymers (PPy and PANI) were used to form compact and ultrathin coating layers on the surface of ball-milled  $V_2O_5$  to reduce the dissolution of positive electrode in aqueous environment. Both polymer-modified electrodes offered significant improvements on the electrochemical performance of RAZBs. Specifically, at room temperature, PPy battery delivered a higher discharge capacity of  $195.7 \text{ mAh}\cdot\text{g}^{-1}$  at a current density of 5 C with only 9.5% capacity loss after 200 cycles. Even under a high temperature condition ( $60^\circ\text{C}$ ), 80% of capacity retention after 150 cycles can be obtained by coating protection. Therefore, polymer-coated electrodes offered superior electrochemical performance under both the ambient and

high temperatures (40°C, 60°C and 80°C), providing a promising approach to realize a thermally stable energy storage system.

Another sub-project introduced a new type of vanadium-based material with dual-ion intercalation (ZNVO) as the cathode in RAZBs. Assisting with a dual-carrier electrolyte (2M ZnSO<sub>4</sub> + 2M Na<sub>2</sub>SO<sub>4</sub>), this dual-ion battery offered a long-term cycle life (~ 89% capacity retention after 4000 cycles) and dendrite-free system. Moreover, the reversible ion de- / intercalation was verified by the tests of XRD, FTIR and CV, offering strong supports on the superb electrochemical performance of this dual-ion system.

Based on the experiences and findings of this project, there are several recommendations for future work in the field of Zn / 2M ZnSO<sub>4</sub> + 2M Na<sub>2</sub>SO<sub>4</sub> / ZNVO studies:

Firstly, the number of electron transfer during the reaction could be found. Once the cathode compositions after charge / discharge were obtained by ICP tests, the electron numbers can be calculated based on their corresponded specific capacities.

Secondly, the participation of H<sup>+</sup> in the reaction need to be investigated by solid-state H<sup>1</sup>-NMR. After that, the overall chemical reaction of ZNVO in 2M ZnSO<sub>4</sub> + 2M Na<sub>2</sub>SO<sub>4</sub> electrolyte would be completed.

Lastly, the type of electrochemical process needs to be explored by CV tests at high scan rates (1-100 mV·s<sup>-1</sup>). Based on the equation  $\log(i) = b \log(v) + \log(a)$  (derived from  $i = av^b$ , where  $i$  is the peak current,  $v$  represents the scan rate), the slope value of

$b$  can be found where  $b$  is often in a range of 0.5-1. If  $b$  closes to 0.5, this reaction is controlled by ion-diffusion; if  $b$  reaches to 1, surface-controlled reaction which also refers to the pseudocapitance would dominate the charge / discharge process.

## References

- [1]. Hayes, B. Analysis: Energy Supply And The Future Of The Oil And Gas Industry. <https://www.dailyoilbulletin.com/article/2018/9/4/analysis-energy-supply-and-the-future-of-the-oil-a/> (accessed Sept 4, 2018)
- [2]. Lithium-ion battery sector: developing a promising sector for Quebec's economy. <https://propulsionquebec.com/wp-content/uploads/2019/09/RAPPORT-BATTERIES-LITHIUM-ION-EN-2.pdf?download=1> (accessed Sept, 2019)
- [3]. Pramudita, J. C., Sehwat, D., Goonetilleke, D., & Sharma, N. (2017). An initial review of the status of electrode materials for potassium-ion batteries. *Advanced Energy Materials*, 7(24), 1602911.
- [4]. Chen, S., Wu, C., Shen, L., Zhu, C., Huang, Y., Xi, K., ... & Yu, Y. (2017). Challenges and Perspectives for NASICON-Type Electrode Materials for Advanced Sodium-Ion Batteries. *Advanced Materials*, 29(48), 1700431.
- [5]. Ni, J., Fu, S., Wu, C., Maier, J., Yu, Y., & Li, L. (2016). Self-supported nanotube arrays of Sulfur-doped TiO<sub>2</sub> enabling ultrastable and robust Sodium storage. *Advanced Materials*, 28(11), 2259-2265.
- [6]. Winter, M., & Brodd, R. J. (2005). What Are Batteries, Fuel Cells, and Supercapacitors (*Chem. Rev.* 2003, 104, 4245– 4269. Published on the Web 09/28/2004.). *Chemical reviews*, 105(3), 1021-1021.
- [7]. Zhang, H., Ye, K., Zhu, K., Cang, R., Yan, J., Cheng, K., ... & Cao, D. (2017). High-Energy-Density Aqueous Magnesium-Ion Battery Based on a Carbon-Coated FeVO<sub>4</sub> Anode and a Mg-OMS-1 Cathode. *Chemistry—A European Journal*, 23(67), 17118-17126.
- [8]. Ponrouch, A., Frontera, C., Bardé, F., & Palacín, M. R. (2016). Towards a calcium-based rechargeable battery. *Nature materials*, 15(2), 169.
- [9]. Canepa, P., Sai Gautam, G., Hannah, D. C., Malik, R., Liu, M., Gallagher, K. G., ... & Ceder, G. (2017). Odyssey of multivalent cathode materials: open questions and future challenges. *Chemical reviews*, 117(5), 4287-4341.
- [10]. Elia, G. A., Marquardt, K., Hoeppe, K., Fantini, S., Lin, R., Knipping, E., ... & Hahn, R. (2016). An overview and future perspectives of aluminum batteries. *Advanced Materials*, 28(35), 7564-7579.
- [11]. Ambroz, F., Macdonald, T. J., & Nann, T. (2017). Trends in Aluminium-Based Intercalation Batteries. *Advanced Energy Materials*, 7(15), 1602093.
- [12]. Das, S. K., Mahapatra, S., & Lahan, H. (2017). Aluminium-ion batteries: developments and challenges. *Journal of Materials Chemistry A*, 5(14), 6347-6367.
- [13]. Sun, X., Blanc, L., Nolis, G. M., Bonnicksen, P., Cabana, J., & Nazar, L. F. (2017). NaV<sub>1.25</sub>Ti<sub>0.75</sub>O<sub>4</sub>: A Potential Post-Spinel Cathode Material for Mg Batteries. *Chemistry of Materials*, 30(1), 121-128.
- [14]. Sun, X., Bonnicksen, P., & Nazar, L. F. (2016). Layered TiS<sub>2</sub> positive electrode for Mg batteries. *ACS Energy Letters*, 1(1), 297-301.

- [15]. Xu, C., Li, B., Du, H., & Kang, F. (2012). Energetic zinc ion chemistry: the rechargeable zinc ion battery. *Angewandte Chemie International Edition*, 51(4), 933-935.
- [16]. Li, Y., & Dai, H. (2014). Recent advances in zinc–air batteries. *Chemical Society Reviews*, 43(15), 5257-5275.
- [17]. Gu, P., Zheng, M., Zhao, Q., Xiao, X., Xue, H., & Pang, H. (2017). Rechargeable zinc–air batteries: a promising way to green energy. *Journal of Materials Chemistry A*, 5(17), 7651-7666.
- [18]. Parker, J. F., Chervin, C. N., Pala, I. R., Machler, M., Burz, M. F., Long, J. W., & Rolison, D. R. (2017). Rechargeable nickel–3D zinc batteries: An energy-dense, safer alternative to lithium-ion. *Science*, 356(6336), 415-418.
- [19]. Song, M., Tan, H., Chao, D., & Fan, H. J. (2018). Recent Advances in Zn-Ion Batteries. *Advanced Functional Materials*, 28(41), 1802564.
- [20]. Dean, J. A. (1999). *Lange's handbook of chemistry*. New york; London: McGraw-Hill, Inc..
- [21]. Marcus, Y. (1988). Ionic radii in aqueous solutions. *Chemical Reviews*, 88(8), 1475-1498.
- [22]. Tansel, B. (2012). Significance of thermodynamic and physical characteristics on permeation of ions during membrane separation: Hydrated radius, hydration free energy and viscous effects. *Separation and purification technology*, 86, 119-126.
- [23]. Popov, K., Grgur, B., & Djokić, S. S. (2007). *Fundamental aspects of electrometallurgy*. Springer Science & Business Media.
- [24]. Fang, G., Zhou, J., Pan, A., & Liang, S. (2018). Recent advances in aqueous zinc-ion batteries. *ACS Energy Letters*, 3(10), 2480-2501.
- [25]. Thackeray, M. M., David, W. I. F., Bruce, P. G., & Goodenough, J. B. (1983). Lithium insertion into manganese spinels. *Materials Research Bulletin*, 18(4), 461-472.
- [26]. Thackeray, M. M., Johnson, P. J., De Picciotto, L. A., Bruce, P. G., & Goodenough, J. B. (1984). Electrochemical extraction of lithium from  $\text{LiMn}_2\text{O}_4$ . *Materials Research Bulletin*, 19(2), 179-187.
- [27]. Goodenough, J. B., Thackeray, M. M., David, W. I. F., & Bruce, P. G. (1984). Lithium insertion/extraction reactions with manganese oxides. *Revue de Chimie minerale*, 21(4), 435-455.
- [28]. Gummow, R. J., De Kock, A., & Thackeray, M. M. (1994). Improved capacity retention in rechargeable 4 V lithium / lithium-manganese oxide (spinel) cells. *Solid State Ionics*, 69(1), 59-67.
- [29]. Bakenov, Z., & Taniguchi, I. (2005). Electrochemical performance of nanostructured  $\text{LiM}_x\text{Mn}_{2-x}\text{O}_4$  (M= Co and Al) powders at high charge–discharge operations. *Solid State Ionics*, 176(11-12), 1027-1034.

- [30]. Xu, D., Li, B., Wei, C., He, Y. B., Du, H., Chu, X., ... & Kang, F. (2014). Preparation and characterization of MnO<sub>2</sub>/ acid-treated CNT nanocomposites for energy storage with zinc ions. *Electrochimica Acta*, 133, 254-261.
- [31]. Qiu, W., Li, Y., You, A., Zhang, Z., Li, G., Lu, X., & Tong, Y. (2017). High-performance flexible quasi-solid-state Zn–MnO<sub>2</sub> battery based on MnO<sub>2</sub> nanorod arrays coated 3D porous nitrogen-doped carbon cloth. *Journal of Materials Chemistry A*, 5(28), 14838-14846.
- [32]. Wang, L., Lu, Y., Liu, J., Xu, M., Cheng, J., Zhang, D., & Goodenough, J. B. (2013). A superior low-cost cathode for a Na-ion battery. *Angewandte Chemie International Edition*, 52(7), 1964-1967.
- [33]. Wessells, C. D., Peddada, S. V., McDowell, M. T., Huggins, R. A., & Cui, Y. (2011). The effect of insertion species on nanostructured open framework hexacyanoferrate battery electrodes. *Journal of the Electrochemical Society*, 159(2), A98-A103.
- [34]. Trócoli, R., & La Mantia, F. (2015). An Aqueous Zinc-Ion Battery Based on Copper Hexacyanoferrate. *ChemSusChem*, 8(3), 481-485.
- [35]. Liang, Y., Jing, Y., Gheyhani, S., Lee, K. Y., Liu, P., Facchetti, A., & Yao, Y. (2017). Universal quinone electrodes for long cycle life aqueous rechargeable batteries. *Nature materials*, 16(8), 841.
- [36]. Zhao, Q., Huang, W., Luo, Z., Liu, L., Lu, Y., Li, Y., ... & Chen, J. (2018). High-capacity aqueous zinc batteries using sustainable quinone electrodes. *Science advances*, 4(3), eaao1761.
- [37]. Häupler, B., Rössel, C., Schwenke, A. M., Winsberg, J., Schmidt, D., Wild, A., & Schubert, U. S. (2016). Aqueous zinc-organic polymer battery with a high rate performance and long lifetime. *NPG Asia Materials*, 8(7), e283.
- [38]. Zhang, N., Dong, Y., Jia, M., Bian, X., Wang, Y., Qiu, M., ... & Cheng, F. (2018). Rechargeable aqueous Zn–V<sub>2</sub>O<sub>5</sub> battery with high energy density and long cycle life. *ACS Energy Letters*, 3(6), 1366-1372.
- [39]. Zavalij, P. Y., & Whittingham, M. S. (1999). Structural chemistry of vanadium oxides with open frameworks. *Acta Crystallographica Section B: Structural Science*, 55(5), 627-663.
- [40]. Zhang, Y. M., Bao, S. X., Liu, T., Chen, T. J., & Huang, J. (2011). The technology of extracting vanadium from stone coal in China: History, current status and future prospects. *Hydrometallurgy*, 109(1-2), 116-124.
- [41]. Whittingham, M. S. (2004). Lithium batteries and cathode materials. *Chemical reviews*, 104(10), 4271-4302.
- [42]. Wang, Y., Takahashi, K., Lee, K. H., & Cao, G. Z. (2006). Nanostructured Vanadium Oxide Electrodes for Enhanced Lithium-Ion Intercalation. *Advanced Functional Materials*, 16(9), 1133-1144.
- [43]. Livage, J. (2010). Hydrothermal synthesis of nanostructured vanadium oxides. *Materials*, 3(8), 4175-4195.

- [44]. Livage, J. (2003). Actuator materials: Towards smart artificial muscle. *Nature Materials*, 2(5), 297.
- [45]. Gu, G., Schmid, M., Chiu, P. W., Minett, A., Frayssé, J., Kim, G. T., ... & Baughman, R. H. (2003). V<sub>2</sub>O<sub>5</sub> nanofibre sheet actuators. *Nature materials*, 2(5), 316.
- [46]. Baughman, R. H., Cui, C., Zakhidov, A. A., Iqbal, Z., Barisci, J. N., Spinks, G. M., ... & Jaschinski, O. (1999). Carbon nanotube actuators. *Science*, 284(5418), 1340-1344.
- [47]. Takahashi, K., Wang, Y., & Cao, G. (2005). Growth and electrochromic properties of single-crystal V<sub>2</sub>O<sub>5</sub> nanorod arrays. *Applied Physics Letters*, 86(5), 053102.
- [48]. Bystrom, A., Wilhelmi, K. A., & Brotzen, O. (1950). Vanadium pentoxide-a compound with five-coordinated vanadium atoms. *Acta. Chem. Scand*, 4, 1119.
- [49]. Yao, J., Li, Y., Massé, R. C., Uchaker, E., & Cao, G. (2018). Revitalized interest in vanadium pentoxide as cathode material for lithium-ion batteries and beyond. *Energy Storage Materials*, 11, 205-259.
- [50]. Fiermans, L., Clauws, P., Lambrecht, W., Vandenbroucke, L., & Vennik, J. (1980). Single crystal V<sub>2</sub>O<sub>5</sub> and lower oxides. A survey of their electronic, optical, structural, and surface properties. *physica status solidi (a)*, 59(2), 485-504.
- [51]. Livage, J. (1991). Vanadium pentoxide gels. *Chemistry of Materials*, 3(4), 578-593.
- [52]. West, K., Zachau-Christiansen, B., Jacobsen, T., & Skaarup, S. (1993). Vanadium oxide xerogels as electrodes for lithium batteries. *Electrochimica acta*, 38(9), 1215-1220.
- [53]. Petkov, V., Trikalitis, P. N., Bozin, E. S., Billinge, S. J., Vogt, T., & Kanatzidis, M. G. (2002). Structure of V<sub>2</sub>O<sub>5</sub> · 105 · nH<sub>2</sub>O Xerogel Solved by the Atomic Pair Distribution Function Technique. *Journal of the American Chemical Society*, 124(34), 10157-10162.
- [54]. Ming, J., Guo, J., Xia, C., Wang, W., & Alshareef, H. N. (2019). Zinc-ion batteries: Materials, mechanisms, and applications. *Materials Science and Engineering: R: Reports*, 135, 58-84.
- [55]. Petkov, V., Zavalij, P. Y., Lutta, S., Whittingham, M. S., Parvanov, V., & Shastri, S. (2004). Structure beyond Bragg: Study of V<sub>2</sub>O<sub>5</sub> nanotubes. *Physical Review B*, 69(8), 085410.
- [56]. Zavalij, P. Y., & Whittingham, M. S. (1999). Structural chemistry of vanadium oxides with open frameworks. *Acta Crystallographica Section B: Structural Science*, 55(5), 627-663.
- [57]. Li, Y., Huang, Z., Kalambate, P. K., Zhong, Y., Huang, Z., Xie, M., ... & Huang, Y. (2019). V<sub>2</sub>O<sub>5</sub> nanopaper as a cathode material with high capacity and long cycle life for rechargeable aqueous zinc-ion battery. *Nano Energy*, 60, 752-759.

- [58]. Yue, Y., & Liang, H. (2017). Micro-and nano-structured vanadium pentoxide ( $V_2O_5$ ) for electrodes of lithium-ion batteries. *Advanced Energy Materials*, 7(17), 1602545.
- [59]. Liu, J., Xia, H., Xue, D., & Lu, L. (2009). Double-shelled nanocapsules of  $V_2O_5$ -based composites as high-performance anode and cathode materials for Li ion batteries. *Journal of the American Chemical Society*, 131(34), 12086-12087.
- [60]. Liu, J., Zhou, Y., Wang, J., Pan, Y., & Xue, D. (2011). Template-free solvothermal synthesis of yolk-shell  $V_2O_5$  microspheres as cathode materials for Li-ion batteries. *Chemical Communications*, 47(37), 10380-10382.
- [61]. Liu, J., Cao, G., Yang, Z., Wang, D., Dubois, D., Zhou, X., ... & Zhang, J. G. (2008). Oriented nanostructures for energy conversion and storage. *ChemSusChem: Chemistry & Sustainability Energy & Materials*, 1(8-9), 676-697.
- [62]. Arico, A. S., Bruce, P., Scrosati, B., Tarascon, J. M., & Van Schalkwijk, W. (2011). Nanostructured materials for advanced energy conversion and storage devices. In *Materials for sustainable energy: a collection of peer-reviewed research and review articles from Nature Publishing Group* (pp. 148-159).
- [63]. Ren, Y., Armstrong, A. R., Jiao, F., & Bruce, P. G. (2009). Influence of size on the rate of mesoporous electrodes for lithium batteries. *Journal of the American Chemical Society*, 132(3), 996-1004.
- [64]. Lu, L., Chen, X., Huang, X., & Lu, K. (2009). Revealing the maximum strength in nanotwinned copper. *Science*, 323(5914), 607-610.
- [65]. Jiang, C., Hosono, E., & Zhou, H. (2006). Nanomaterials for lithium ion batteries. *Nano today*, 1(4), 28-33.
- [66]. Li, G., Pang, S., Jiang, L., Guo, Z., & Zhang, Z. (2006). Environmentally friendly chemical route to vanadium oxide single-crystalline nanobelts as a cathode material for lithium-ion batteries. *The Journal of Physical Chemistry B*, 110(19), 9383-9386.
- [67]. Wang, H. G., Ma, D. L., Huang, Y., & Zhang, X. B. (2012). Electrospun  $V_2O_5$  Nanostructures with Controllable Morphology as High-Performance Cathode Materials for Lithium-Ion Batteries. *Chemistry—A European Journal*, 18(29), 8987-8993.
- [68]. Li, Y., Yao, J., Uchaker, E., Yang, J., Huang, Y., Zhang, M., & Cao, G. (2013). Leaf-Like  $V_2O_5$  Nanosheets Fabricated by a Facile Green Approach as High Energy Cathode Material for Lithium-Ion Batteries. *Advanced Energy Materials*, 3(9), 1171-1175.
- [69]. Chan, C. K., Peng, H., Twisten, R. D., Jarausch, K., Zhang, X. F., & Cui, Y. (2007). Fast, completely reversible Li insertion in vanadium pentoxide nanoribbons. *Nano letters*, 7(2), 490-495.
- [70]. Yin, H., Yu, K., Peng, H., Zhang, Z., Huang, R., Travas-Sejdic, J., & Zhu, Z. (2012). Porous  $V_2O_5$  micro / nano-tubes: Synthesis via a CVD route, single-tube-based humidity sensor and improved Li-ion storage properties. *Journal of Materials Chemistry*, 22(11), 5013-5019.

- [71]. Wang, Z. L., Xu, D., Wang, L. M., & Zhang, X. B. (2012). Facile and Low-Cost Synthesis of Large-Area Pure  $V_2O_5$  Nanosheets for High-Capacity and High-Rate Lithium Storage over a Wide Temperature Range. *ChemPlusChem*, 77(2), 124-128.
- [72]. Yan, D. J., Zhu, X. D., Wang, K. X., Gao, X. T., Feng, Y. J., Sun, K. N., & Liu, Y. T. (2016). Facile and elegant self-organization of Ag nanoparticles and  $TiO_2$  nanorods on  $V_2O_5$  nanosheets as a superior cathode material for lithium-ion batteries. *Journal of Materials Chemistry A*, 4(13), 4900-4907.
- [73]. Seng, K. H., Liu, J., Guo, Z. P., Chen, Z. X., Jia, D., & Liu, H. K. (2011). Free-standing  $V_2O_5$  electrode for flexible lithium ion batteries. *Electrochemistry Communications*, 13(5), 383-386.
- [74]. Wang, S., Lu, Z., Wang, D., Li, C., Chen, C., & Yin, Y. (2011). Porous monodisperse  $V_2O_5$  microspheres as cathode materials for lithium-ion batteries. *Journal of Materials Chemistry*, 21(17), 6365-6369.
- [75]. Li, H., & Zhou, H. (2012). Enhancing the performances of Li-ion batteries by carbon-coating: present and future. *Chemical Communications*, 48(9), 1201-1217.
- [76]. Chen, Z., Qin, Y., Amine, K., & Sun, Y. K. (2010). Role of surface coating on cathode materials for lithium-ion batteries. *Journal of Materials Chemistry*, 20(36), 7606-7612.
- [77]. Zhang, X. F., Wang, K. X., Wei, X., & Chen, J. S. (2011). Carbon-coated  $V_2O_5$  nanocrystals as high performance cathode material for lithium ion batteries. *Chemistry of Materials*, 23(24), 5290-5292.
- [78]. Zhou, X., Wu, G., Wu, J., Yang, H., Wang, J., Gao, G., ... & Yan, Q. (2013). Multiwalled carbon nanotubes- $V_2O_5$  integrated composite with nanosized architecture as a cathode material for high performance lithium ion batteries. *Journal of Materials Chemistry A*, 1(48), 15459-15468.
- [79]. De Volder, M. F., Tawfick, S. H., Baughman, R. H., & Hart, A. J. (2013). Carbon nanotubes: present and future commercial applications. *science*, 339(6119), 535-539.
- [80]. Baughman, R. H., Zakhidov, A. A., & De Heer, W. A. (2002). Carbon nanotubes--the route toward applications. *science*, 297(5582), 787-792.
- [81]. Su, D. S., & Schlögl, R. (2010). Nanostructured carbon and carbon nanocomposites for electrochemical energy storage applications. *ChemSusChem: Chemistry & Sustainability Energy & Materials*, 3(2), 136-168.
- [82]. Li, G., Zhang, C., Peng, H., & Chen, K. (2009). One-Dimensional  $V_2O_5$ @ Polyaniline Core/Shell Nanobelts Synthesized by an In situ Polymerization Method. *Macromolecular rapid communications*, 30(21), 1841-1845.
- [83]. Xu, H., Chen, J., Zhang, H., Zhang, Y., Li, W., & Wang, Y. (2016). Fabricating  $SiO_2$ -coated  $V_2O_5$  nanoflake arrays for high-performance lithium-ion batteries with enhanced cycling capability. *Journal of Materials Chemistry A*, 4(11), 4098-4106.
- [84]. George, S. M. (2009). Atomic layer deposition: an overview. *Chemical reviews*, 110(1), 111-131.

- [85]. Xie, M., Sun, X., Sun, H., Porcelli, T., George, S. M., Zhou, Y., & Lian, J. (2016). Stabilizing an amorphous  $V_2O_5$ /carbon nanotube paper electrode with conformal  $TiO_2$  coating by atomic layer deposition for lithium ion batteries. *Journal of Materials Chemistry A*, 4(2), 537-544.
- [86]. Li, C., Zhang, H.P., Fu, L.J., Liu, H., Wu, Y.P., Rahm, E., . . . Wu, H.Q. (2006). Cathode materials modified by surface coating for lithium ion batteries. *Electrochimica Acta*, 51(19), 3872-3883.
- [87]. Chen, Z., Qin, Y., Amine, K., & Sun, Y. K. (2010). Role of surface coating on cathode materials for lithium-ion batteries. *Journal of Materials Chemistry*, 20(36), 7606-7612.
- [88]. Wu, Y. P., Rahm, E., & Holze, R. (2002). Effects of heteroatoms on electrochemical performance of electrode materials for lithium ion batteries. *Electrochimica Acta*, 47(21), 3491-3507.
- [89]. Iwanaga, S., Marciniak, M., Darling, R. B., & Ohuchi, F. S. (2007). Thermopower and electrical conductivity of sodium-doped  $V_2O_5$  thin films. *Journal of applied physics*, 101(12), 123709.
- [90]. Zhu, D., Liu, H., Lv, L., Yao, Y. D., & Yang, W. Z. (2008). Hollow microspheres of  $V_2O_5$  and Cu-doped  $V_2O_5$  as cathode materials for lithium-ion batteries. *Scripta Materialia*, 59(6), 642-645.
- [91]. Yu, H., Rui, X., Tan, H., Chen, J., Huang, X., Xu, C., . . . & Yan, Q. (2013). Cu doped  $V_2O_5$  flowers as cathode material for high-performance lithium ion batteries. *Nanoscale*, 5(11), 4937-4943.
- [92]. Ming, F., Liang, H., Lei, Y., Kandambeth, S., Eddaoudi, M., & Alshareef, H. N. (2018). Layered  $Mg_xV_2O_5 \cdot nH_2O$  as Cathode Material for High-Performance Aqueous Zinc Ion Batteries. *ACS Energy Letters*, 3(10), 2602-2609.
- [93]. Zhu, K., Qiu, H., Zhang, Y., Zhang, D., Chen, G., & Wei, Y. (2015). Synergetic effects of  $Al^{3+}$  doping and graphene modification on the electrochemical performance of  $V_2O_5$  cathode materials. *ChemSusChem*, 8(6), 1017-1025.
- [94]. Kundu, D., Adams, B. D., Duffort, V., Vajargah, S. H., & Nazar, L. F. (2016). A high-capacity and long-life aqueous rechargeable zinc battery using a metal oxide intercalation cathode. *Nature Energy*, 1(10), 16119.
- [95]. He, P., Zhang, G., Liao, X., Yan, M., Xu, X., An, Q., . . . & Mai, L. (2018). Sodium Ion Stabilized Vanadium Oxide Nanowire Cathode for High-Performance Zinc-Ion Batteries. *Advanced Energy Materials*, 8(10), 1702463.
- [96]. Badot, J. C., & Dubrunfaut, O. (2011). Evidence for transition from polaron to bipolaron conduction in electroactive  $Li_xCr_{0.11}V_2O_{5.16}$  powders: A dynamic study from 10 to 1010 Hz. *Journal of Solid State Chemistry*, 184(12), 3208-3215.
- [97]. Somboonsub, B., Srisuwan, S., Invernale, M. A., Thongyai, S., Praserttham, P., Scola, D. A., & Sotzing, G. A. (2010). Comparison of the thermally stable conducting polymers PEDOT, PANi, and PPy using sulfonated poly (imide) templates. *Polymer*, 51(20), 4472-4476.

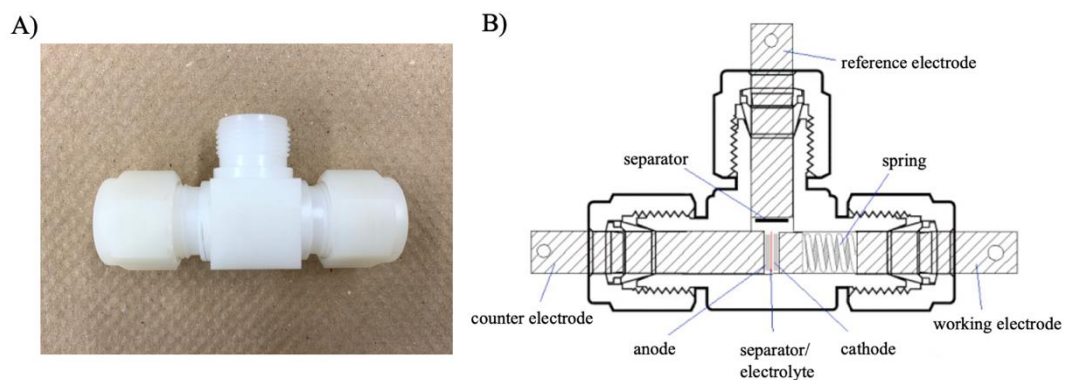
- [98]. Yussuf, A., Al-Saleh, M., Al-Enezi, S., & Abraham, G. (2018). Synthesis and Characterization of Conductive Polypyrrole: The Influence of the Oxidants and Monomer on the Electrical, Thermal, and Morphological Properties. *International Journal of Polymer Science*, 2018.
- [99]. Kumar, D., & Sharma, R. C. (1998). Advances in conductive polymers. *European polymer journal*, 34(8), 1053-1060.
- [100]. Zhao, H., Yuan, A., Liu, B., Xing, S., Wu, X., & Xu, J. (2012). High cyclic performance of V<sub>2</sub>O<sub>5</sub> @ PPy composite as cathode of recharged lithium batteries. *Journal of Applied Electrochemistry*, 42(3), 139-144.
- [101]. Ravichandran, R., Sundarrajan, S., Venugopal, J. R., Mukherjee, S., & Ramakrishna, S. (2010). Applications of conducting polymers and their issues in biomedical engineering. *Journal of the Royal Society Interface*, 7(suppl\_5), S559-S579.
- [102]. Le, T. H., Kim, Y., & Yoon, H. (2017). Electrical and electrochemical properties of conducting polymers. *Polymers*, 9(4), 150.
- [103]. Noerochim, L., Wang, J., Wexler, D., Rahman, M., Chen, J., & Liu, H. (2012). Impact of mechanical bending on the electrochemical performance of bendable lithium batteries with paper-like free-standing V<sub>2</sub>O<sub>5</sub>-polypyrrole cathodes. *Journal of Materials Chemistry*, 22(22), 11159-11165.
- [104]. Yi, N., & Abidian, M. R. (2016). Conducting polymers and their biomedical applications. In *Biosynthetic Polymers for Medical Applications* (pp. 243-276). Woodhead Publishing.
- [105]. Wan, F., Zhang, L., Dai, X., Wang, X., Niu, Z., & Chen, J. (2018). Aqueous rechargeable zinc / sodium vanadate batteries with enhanced performance from simultaneous insertion of dual carriers. *Nature communications*, 9(1), 1656.
- [106]. Ding, F., Xu, W., Graff, G. L., Zhang, J., Sushko, M. L., Chen, X., ... & Liu, X. (2013). Dendrite-free lithium deposition via self-healing electrostatic shield mechanism. *Journal of the American Chemical Society*, 135(11), 4450-4456.
- [107]. Hu, P., Zhu, T., Wang, X., Wei, X., Yan, M., Li, J., ... & Zhou, Z. (2018). Highly durable Na<sub>2</sub>V<sub>6</sub>O<sub>16</sub> · 1.63H<sub>2</sub>O nanowire cathode for aqueous zinc-ion battery. *Nano letters*, 18(3), 1758-1763.
- [108]. Mokhtari, F., Latifi, M., & Shamshirsaz, M. (2016). Electrospinning / electro spray of polyvinylidene fluoride (PVDF): piezoelectric nanofibers. *The Journal of The Textile Institute*, 107(8), 1037-1055.
- [109]. Li, Y. (2012). Synthesis, structure, and characterization of hybrid solids containing polyoxometalates and ruthenium polypyridyl complexes.
- [110]. Segales, M. (2015). Nanoconfinement of complex hydrides in porous hosts for hydrogen storage applications (Doctoral dissertation, University of Glasgow).
- [111]. Channam, V. S. K. (2017). Synthesis of strongly correlated oxides and investigation of their electrical and optical properties (Doctoral dissertation).

- [112]. Sebastian, A. R. (2017). *Electrical Characteristics of Hydroxyapatite (Ca)<sub>x</sub>(BaTiO<sub>3</sub>)<sub>1-x</sub> Composite* (Doctoral dissertation, The University of Texas at San Antonio).
- [113]. Mitha, A., Yazdi, A. Z., Ahmed, M., & Chen, P. (2018). Surface adsorption of polyethylene glycol to suppress dendrite formation on zinc anodes in rechargeable aqueous batteries. *ChemElectroChem*, 5(17), 2409-2418.
- [114]. Gharbi, O. (2016). In-situ investigation of elemental corrosion reactions during the surface treatment of Al-Cu and Al-Cu-Li alloys (Doctoral dissertation, Paris 6).
- [115]. Langford, J. I.; Wilson, A. J. C.; IUCr. Scherrer after Sixty Years: A Survey and Some New Results in the Determination of Crystallite Size. *J. Appl. Crystallogr.* **1978**, 11 (2), 102–113.
- [116]. Altin, B. (2019). Synthesis and characterization of poly ((2-dimethylamino) ethyl methacrylate) (PDMAEMA) modified silica nanoparticles.
- [117]. Alazragi, R. S. (2014). Self-assembling peptides as biofunctional component in medical fabrics. University of Leeds.
- [118]. Bacsik, Z., Mink, J., & Keresztury, G. (2004). FTIR spectroscopy of the atmosphere. I. Principles and methods. *Applied Spectroscopy Reviews*, 39(3), 295-363.
- [119]. Clayborne, A.; Vernon, M. Fourier Transform Infrared Spectroscopy (FTIR)-Chemistry LibreTexts  
[https://chem.libretexts.org/Courses/Howard\\_University/Howard%3A\\_Physical\\_Chemistry\\_Laboratory/14.\\_Fourier\\_Transform\\_Infrared\\_Spectroscopy\\_\(FTIR\)](https://chem.libretexts.org/Courses/Howard_University/Howard%3A_Physical_Chemistry_Laboratory/14._Fourier_Transform_Infrared_Spectroscopy_(FTIR))  
 (accessed Jun 17, 2018).
- [120]. Chen, Z. (2018). *Mechanical and Materials Development of Radio-Frequency Contact for the ITER Ion Cyclotron Resonance Heating Antenna* (Doctoral dissertation).
- [121]. Fonseca, A. J. R. (2018). Chemistry vs Topography: Influence on the biotic interface (Master's thesis).
- [122]. Yulianis, Y., Muhammad, S., Pontas, K., Mariana, M., & Mahidin, M. (2018, May). Characterization and Activation of Indonesian Natural Zeolite from Southwest Aceh District-Aceh Province. In *IOP Conference Series: Materials Science and Engineering* (Vol. 358, No. 1, p. 012052). IOP Publishing.
- [123]. Scanning Electron Microscopy. *Nanoscience instruments*.  
<https://www.nanoscience.com/techniques/scanning-electron-microscopy/>
- [124]. Singh, A. K. (2016). Chapter 4-Experimental Methodologies for the Characterization of Nanoparticles. *Engineered Nanoparticles: Structure, Properties and Mechanisms of Toxicity*, Singh, AK (Ed.), Academic Press, New York, 125-170.
- [125]. Pattanaik, M. (2011). Synthesis and Characterizations of Lead Free KNN Ceramics Near Morphotropic Phase Boundaries (Doctoral dissertation).

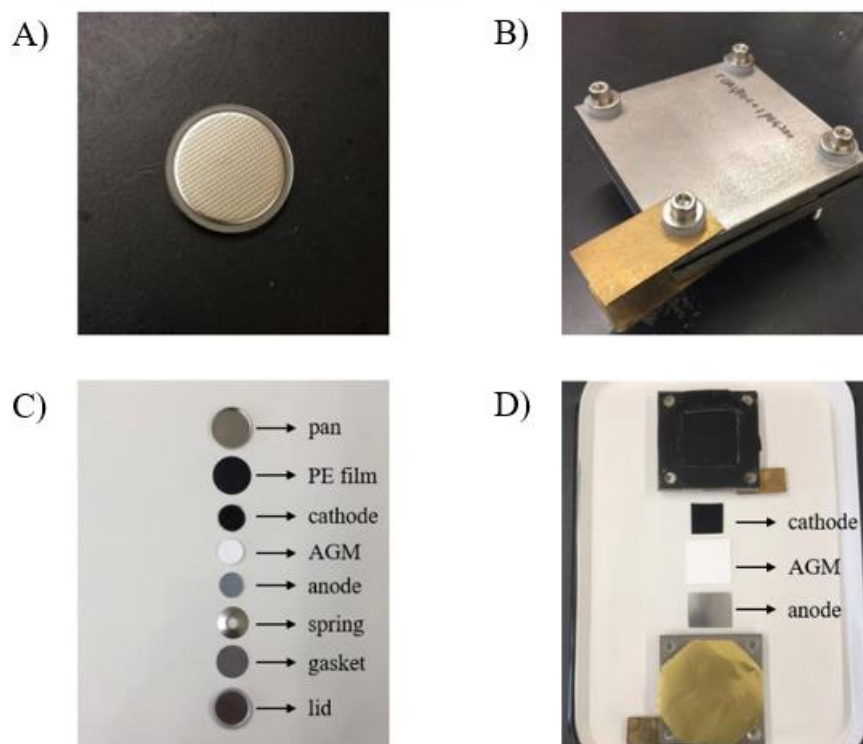
- [126]. Khursheed, A. (2007). *U.S. Patent No. 7,294,834*. Washington, DC: U.S. Patent and Trademark Office.
- [127]. Zhang, R., & Ulery, B. D. (2018). Synthetic vaccine characterization and design. *Journal of Bionanoscience*, 12(1), 1-11.
- [128]. Nogara, J., & Zarrouk, S. J. (2018). Corrosion in geothermal environment Part 2: Metals and alloys. *Renewable and Sustainable Energy Reviews*, 82, 1347-1363.
- [129]. Sandhya, K. P., & Sugunan, S. (2014). *Synthesis, Characterization and Applications of Hybrid Nanocomposites of TiO<sub>2</sub> With Conducting Polymers* (Doctoral dissertation, Cochin University of Science and Technology).
- [130]. Zhang, J. (2016). Electrodeposition of novel nanostructured and porous materials for advanced applications synthesis, structural characterization and physical/chemical performance.
- [131]. Bioscience Notes.  
<https://www.biosciencenotes.com/transmission-electron-microscope-tem/>
- [132]. Atomic World. Atomic World - Transmission electron microscope (TEM) - Principle of TEM  
[http://www.hk-phy.org/atomic\\_world/tem/tem02\\_e.html](http://www.hk-phy.org/atomic_world/tem/tem02_e.html) (accessed Jun 17, 2018).
- [133]. ELUMALAI, N. K. (2013). Engineering of binary metal oxide nanostructures for highly efficient and stable excitonic solar cells (Doctoral dissertation).
- [134]. "Principle of X-ray photoelectron spectroscopy (XPS) | TikZ example."  
[Online]. Available:  
<http://www.texample.net/tikz/examples/principle-of-x-ray-photoelectron-spectroscopy-xps/>. [Accessed: 01-Jul-2018].
- [135]. Haasch, R. T. (2014). X-ray photoelectron spectroscopy (XPS) and auger electron spectroscopy (AES). In *Practical Materials Characterization* (pp. 93-132). Springer, New York, NY.
- [136]. Ohrelius, M. (2019). Fabrication and Evaluation of Perovskite LaCrO<sub>3</sub> Nanoparticles as Catalyst for Electrochemical Ammonia Synthesis.
- [137]. Rowell, R. M., & Diertenberger, M. A. (2013). Thermal properties, combustion, and fire retardancy of wood. In: *Second edition of the Handbook of wood Chemistry and Wood Composites*, Roger Rowell, Editor, by CRC Books, 2013, (6), 127-149.
- [138]. Principle of ICP Mass Spectrometry (ICP-MS). Available:  
<https://www.hitachihightech.com/global/products/science/tech/ana/icp/descriptions/icp-ms.html>
- [139]. Electrochemical Impedance Spectroscopy. In *LibreTexts Engineering*. Available:  
[https://eng.libretexts.org/Bookshelves/Materials\\_Science/Supplemental\\_Modules\\_\(Materials\\_Science\)/Insulators/Electrochemical\\_Impedance\\_Spectroscopy](https://eng.libretexts.org/Bookshelves/Materials_Science/Supplemental_Modules_(Materials_Science)/Insulators/Electrochemical_Impedance_Spectroscopy)  
[Accessed: 05-Jun-2019].
- [140]. Tabrizi, A. G., Arsalani, N., Mohammadi, A., Ghadimi, L. S., Ahadzadeh, I., & Namazi, H. (2018). A new route for the synthesis of polyaniline nanoarrays on

- graphene oxide for high-performance supercapacitors. *Electrochimica Acta*, 265, 379-390.
- [141]. Macdonald, D. D. (2006). Reflections on the history of electrochemical impedance spectroscopy. *Electrochimica Acta*, 51(8-9), 1376-1388.
- [142]. Makokha, V. (2018). Separation, Electroanalytical, And Spectrochemical Techniques.
- [143]. A. J. Bard and L. R. Faulkner, *Electrochemical methods: fundamentals and applications*. Wiley, 1980.
- [144]. He, P., Quan, Y., Xu, X., Yan, M., Yang, W., An, Q., ... & Mai, L. (2017). High-Performance Aqueous Zinc-Ion Battery Based on Layered  $H_2V_3O_8$  Nanowire Cathode. *Small*, 13(47), 1702551.
- [145]. Huang, X., Hu, N., Gao, R., Yu, Y., Wang, Y., Yang, Z., . . . Zhang, Y. (2012). Reduced graphene oxide-polyaniline hybrid: Preparation, characterization and its applications for ammonia gas sensing. *Journal of Materials Chemistry*, 22(42), 22488-22495.
- [146]. Zhou, J., Shan, L., Wu, Z., Guo, X., Fang, G., & Liang, S. (2018). Investigation of  $V_2O_5$  as a low-cost rechargeable aqueous zinc ion battery cathode. *Chemical Communications*, 54(35), 4457-4460.
- [147]. Hu, Ping, Yan, Mengyu, Zhu, Ting, Wang, Xuanpeng, Wei, Xiujuan, Li, Jiantao, . . . Mai, Liqiang. (2017). Zn / VO Aqueous Hybrid-Ion Battery with High Voltage Platform and Long Cycle Life. *ACS Applied Materials & Interfaces*, 9(49), 42717-42722.
- [148]. Han, M., Zhi, J., Hoang, T. K., Li, Y., Li, L., & Chen, P. (2019). Artificial solid electrolyte interphase for thermally stable rechargeable aqueous zinc batteries. *Journal of Power Sources*, 441, 227171.

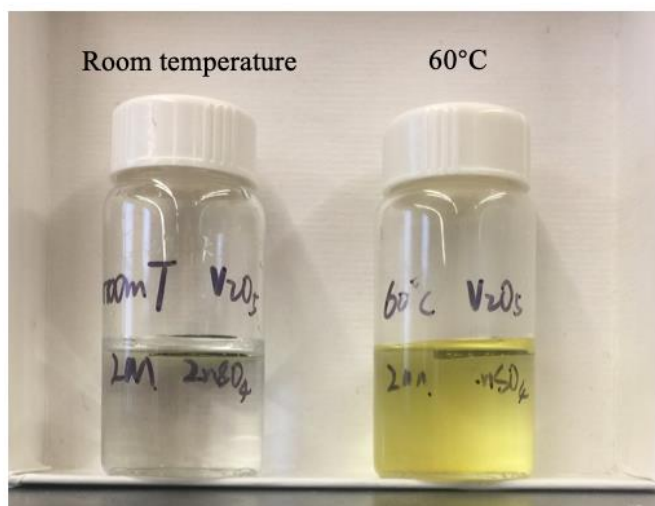
## Appendices



Appendix 1. A) External view of the T-cell Swagelok, B) schematic of the T-cell Swagelok



Appendix 2. A) coin cell, B) large battery and the internal composition of C) coin cell and D) large battery.



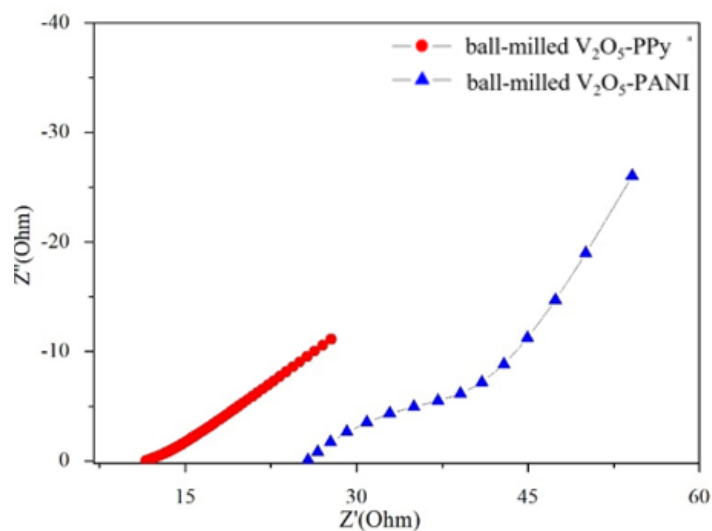
Appendix 3. Optical image of  $V_2O_5$  electrode in 2M  $ZnSO_4$  electrolyte at room temperature and  $60^\circ C$  for 3 hours.

cycle numbers temperatures	50	100	150
	$40^\circ C$	96.0 %	85.4 %
$60^\circ C$	99.8 %	88.4 %	80.1 %
$80^\circ C$	88.6 %	83.2 %	70.4 %

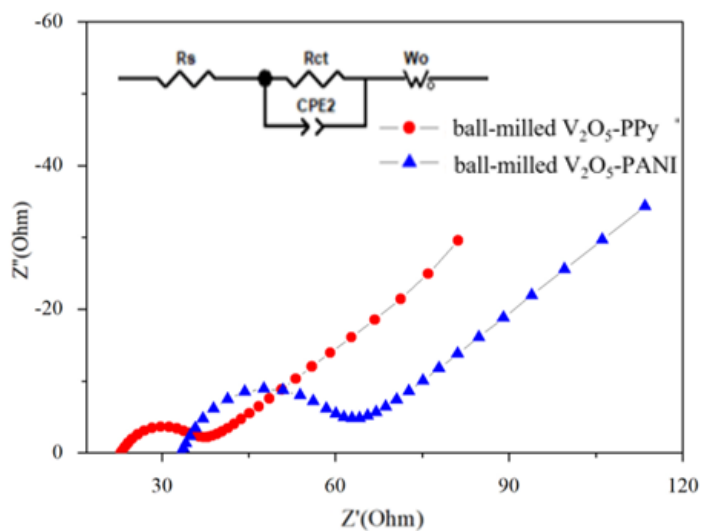
Appendix 4. Capacity retention of ball-milled  $V_2O_5$ -PPy sample with a current density of 5 C at different temperatures.

cycle numbers temperatures	50	100	150
	$40^\circ C$	102.2 %	101.5 %
$60^\circ C$	99.3 %	105.7 %	84.2 %
$80^\circ C$	92.3 %	90.8 %	90.1 %

Appendix 5. Capacity retention of ball-milled  $V_2O_5$ -PANI sample with a current density of 5 C at different temperatures.



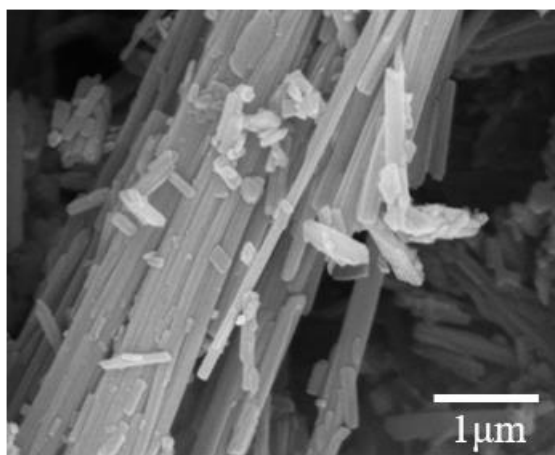
Appendix 6. Nyquist plots of conductive polymer-PPy and PANI at their 50th cycle at room temperature.



Appendix 7. Nyquist plots of ball-milled  $V_2O_5$ -PPy and ball-milled  $V_2O_5$ -PANI samples at their 50th cycle at 80°C.

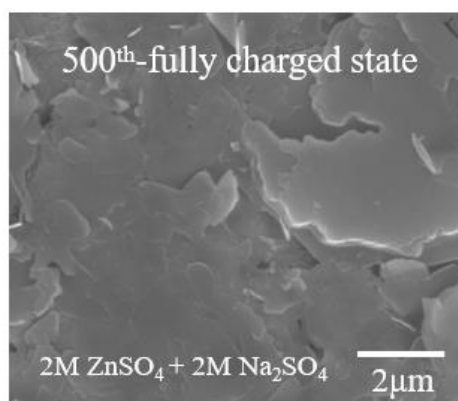
samples	impedance	
	$R_s$ (Ohm)	$R_{ct}$ (Ohm)
ball-milled $V_2O_5$ -PPy	21.93	12.39
ball-milled $V_2O_5$ -PANI	32.12	25.16

Appendix 8. EIS measurement results at 80°C.



Appendix 9. SEM image of  $V_2O_5$  nanobelt with the average width of 100-200 nm.

The scale bar is 1  $\mu\text{m}$ .



Appendix 10. SEM image of anode surface after 500 cycles at a fully charged state in 2M  $ZnSO_4$  + 2M  $Na_2SO_4$  electrolyte.